**Title**
Design and Analysis of Spectrum Scanners Based on Passive, Linear Periodically Time-Varying Circuits



**Author**
Sinha, Neha

**Publication Date**
2017

Peer reviewed|Thesis/dissertation

UNIVERSITY OF CALIFORNIA

Los Angeles

# Design and Analysis of Spectrum Scanners Based on Passive, Linear Periodically Time-Varying Circuits

A dissertation submitted in partial satisfaction of the

requirements for the degree Doctor of Philosophy

in Electrical Engineering

by

Neha Sinha

2017

ABSTRACT OF THE DISSERTATION

Design and Analysis of Spectrum Scanners Based on Passive, Linear Periodically Time-Varying Circuits

by

Neha Sinha

Doctor of Philosophy in Electrical Engineering

University of California, Los Angeles, 2017

Professor Sudhakar Pamarti, Chair

Spectrum sensing finds its use is many applications. With modern communication systems moving towards Cognitive Radios (CRs) to better utilize the available spectrum, spectrum sensing is a key enabling functionality that allows the detection of primary users and interferes to support spectrum sharing. Spectrum sensing can also be useful in security applications that require a certain degree of RF spectrum awareness. In addition, it can be used for built-in self-test like transmitter tuning by measuring the output spectrum to allow spur reduction and digital predistortion.

To be useful, the spectrum scanners used for sensing should be able to handle large blockers and detect weak signals at the same time. Thus both good linearity and high sensitivity are desired. In addition, these scanners need to be highly programmable and selective while incurring a low power cost.

In this research we have addressed the issues that plague traditional spectrum scanners by using the recent technique of Filtering by Aliasing (FA). The FA-based spectrum scanner is a passive structure that uses simple but linear, periodically time-varying (LPTV) RC circuits. This LPTV

circuit is shown to provide a high spurious-free dynamic range, precise resolution bandwidths while still consuming very low power.

In this dissertation, the FA technique is briefly explained, and the design considerations and implementation of a spectrum scanner IC that achieves excellent linearity and low power as compared to state-of-the-art designs is presented. In addition, a theoretical analysis of some of the limiting factors of the passive LPTV scanner is presented together with some circuit and/or signal-processing solutions.

Chapters 2 and 3 of this dissertation are the reprint of a paper that is to be published in full in the IEEE Journal of Solid-States Circuits (JSSC). The dissertation author is the primary investigator and Professor Sudhakar Pamarti supervised the research which forms the basis for this paper. Dr. Mansour Rachid and Professor Shanthi Pavan from IIT, Madras collaborated on this work as well.

Chapters 4 and 5 of this dissertation are the reprint of a paper under preparation to be submitted in part or in full to the IEEE Transactions of Circuits and Systems-1 (TCAS-1). The dissertation author is the primary investigator and Professor Sudhakar Pamarti supervised the research which forms the basis for this paper. By the virtue of being independent papers, there is a slight degree of content overlap between Chapters 2-3 and 4-5.

The dissertation of Neha Sinha is approved.

Danijela Cabric

Chih Kong Ken Yang

Mario Gerla

Sudhakar Pamarti, Committee Chair

University of California, Los Angeles

2017

*To Papa and Ma.*

# TABLE OF CONTENTS

# LIST OF FIGURES

# LIST OF TABLES

# ACKNOWLEDGEMENTS

*"The more you know, the more you know you don't know."*

*- Aristotle*

Graduate school has been a humbling experience which has taught me a lot both academically and otherwise and I have a lot of people to thank for this. First and foremost, I would like to thank my advisor, Prof. Sudhakar Pamarti for giving me the opportunity to work with him and for being a great mentor. I will always be grateful for his kindness and patience over the years and for the countless hours he has spent discussing interesting research topics with me. I can recollect many a times leaving our meetings feeling inspired and motivated. I am also in awe of his depth and breadth of knowledge in the field, his stress on developing intuition while still being mathematically rigorous. I hope I can imbibe some of his qualities in my professional life.

I would also like to thank my committee members: Prof. Danijela Cabric, Prof. Chih Kong Ken Yang and Prof. Mario Gerla. I have always had pleasant interactions with Prof. Cabric and I am thankful for her help over the course of my time as a graduate student both when I took her classes and otherwise. I am thankful to Prof. Yang for agreeing to be on my committee at the last minute and for his words of encouragement. I am also grateful to Prof. Gerla for taking out time from his busy schedule to be on the committee.

My academic experience at UCLA was greatly enhanced and rewarding from all my interactions with Prof. Asad Abidi both inside and outside class. His very basic and intuitive style of teaching is matched to none other. His teachings were and will be extremely valuable in my academic and professional life.

Trying to keep track of administrative requirements were made seamless thanks to Kyle, Deeona and Mandy. They will be part of one of my favorite memories at UCLA. Long discussions with Deeona about life, family, school and her work were always a good break from all the research. Thank you for caring for all of us students so much Deeona, it means a lot to us. Thank you to Kyle for planning events for us, for taking care of the ICSL lab and just for being a very fun and thoughtful person to be around. I know I have ranted a lot to you, but thank you for always listening patiently. I would also like to thank Sandra Bryant, Marty Revilla, Minji Zhu, Richard Al-Hadi, Yen-Cheng, Joseph Chen for their help with various administrative and technical tasks related to tapeout and testing.

I would also like to thank my group members for the extremely valuable discussions about research and for the good (and stressful) times we have shared in the ICSL lab. I am thankful to Dr. Mansour Rachid for our fruitful collaboration in this work and for his continuous encouragement and optimism, my friend and lab mate Jeffrey Lee who was always pleasant to work with and Abhishek Ghosh for teaching me about the nuances of tapeout. I would also like to thank Sameed for proof reading my papers and for our various research discussions. I want to thank my other group members: Sunbo, Nitin, Szu-Yao, Hani, Shi and Jiyue. I was fortunate to have met some great senior graduate students (Vaibhav, Cheng, Yousr, Arash, Joseph) who gave valuable technical advice and helped expand my knowledge during the course of my studies.

I was fortunate to have made some good friends along the way who shared the fun and pain of this journey. My friend and cubicle-mate for 7 years, Hari, who is probably the one person I have interacted the most with during my time at UCLA. I have learnt SO much from him academically and can only hope to acquire his work ethics. I will miss our discussions about research, life and

everything in between. Thanks for patiently listening to my long monologues. I cherish and will miss my times with Dejan and Sina and some of our "great adventures" together. They made life at UCLA fun. I am also grateful to some other members of Prof. Markovic's group (Richard, Yuta, Vahagn, Wenlong, Alireza) for treating me as one of their own. I would also like to thank my friends Manas,Vikrant, Mukesh, Saakshita, Mihir, Shaunak, Yasmine, Jad, Shailesh who I have shared some good times with.

My time at graduate school drastically changed for the better after my friend of 12 years, Neha came to study at UCLA as well. I am so glad we got to stay together and spend some of the most wonderful times together. The time spent with her will be my favorite thing about LA. I would also like to thank my other Waterloo friends: Sana, Suraj, Brenden, Rahul, Vipul, Pui-Yee, Mladen, Jon and Nikhil, who have always been by my side and whose friendship I will always cherish.

I would not have made it so far in life without the unending support from my family. I am so grateful to have two extremely wonderful sisters, Arti and Puja who have loved me so much. Life would never be as fun without the two of you. I am fortunate to have found a very supportive and amazing life partner in Siddharth, who brings happiness in my life. I would also like to thank my brother in-law, Pratyush for loving me like his younger sister. I want to thank Siddharth's (and my new) family for their good wishes and my relatives in India, especially my grandmother for playing a huge part in who I am today. And lastly and most importantly, I am extremely indebted to my parents. I am thankful to my father for his constant encouragement, motivation and for believing in me more than I have. Thanks Papa for always listening to my tapeout and research woes and giving me the best advice. Thank you Ma for being the most loving mother and being someone

whose voice never fails to make me happy. This work is because of the two of you and dedicated to you!

# VITA

| | |
|---|---|
| 2005-2010 | Bachelor of Applied Science, Honors Co-op<br>University of Waterloo, Waterloo, Ontario, Canada |
| 2010-2012 | Master of Science,<br>University of California, Los Angeles, California, USA |
| 2013-2017 | Graduate Student Researcher,<br>University of California, Los Angeles, California, USA |

# PUBLICATIONS

- N. Sinha, M. Rachid, S. Pavan and S. Pamarti, "Design and Analysis of an 8mW, 1GHz Span, Passive Spectrum Scanner with > +31dBm Out-of-Band IIP3 using Periodically Time-Varying Circuit Components," IEEE J. Solid-State Circuits. (*Accepted*)

- S. Pamarti, N. Sinha, S. Hameed and M. Rachid, "Time-Varying Circuit Approaches for Software Defined and Cognitive Radio Applications," 13th International SoC Design Conference, Jeju, Korea, 2016. (*Invited*)

- N. Sinha, M. Rachid and S. Pamarti, "An 8mW, 1GHz span, passive spectrum scanner with > +31dBm out-of-band IIP3," 2016 IEEE Radio Frequency Integrated Circuits Symposium (RFIC), San Francisco, CA, 2016, pp. 278-281.

- S. Hameed, N. Sinha, M. Rachid and S. Pamarti, "26.6 A programmable receiver front-end achieving >17dBm IIP3 at <1.25xBW frequency offset," 2016 IEEE International Solid-State Circuits Conference (ISSCC), San Francisco, CA, 2016, pp. 446-447.

- N. Sinha, M. Rachid and S. Pamarti, "A sharp programmable passive filter based on filtering by Aliasing," 2015 Symposium on VLSI Circuits (VLSI Circuits), Kyoto, 2015, pp. C58-C59.

# Chapter 1

## Introduction

Spectrum sensing is a key enabling technology for efficient use of the electromagnetic spectrum. The spectrum information provided by the scanners can find widespread use in military applications, automotive industry employing self-driving cars or for on-chip built-in self test [1], to name a few. One of most important application of spectrum sensors is perhaps their use as part of Cognitive Radios (CRs) [2]. As shown in Fig. 1.1, CR networks are envisioned to tackle the problem of low spectrum utilization by exploiting spectral opportunities in time, frequency, and space. The basic idea of CRs is to enable license-exempt (secondary) users to utilize the vacant spaces in the licensed spectrum as and when they become available. The aim is to help increase the spectrum efficiency and alleviate the crowding of unlicensed spectra. A spectrum scanner can help identify these opportunities by detecting the primary users and interferes and enable the best use of the available spectrum by allowing spectrum sharing.

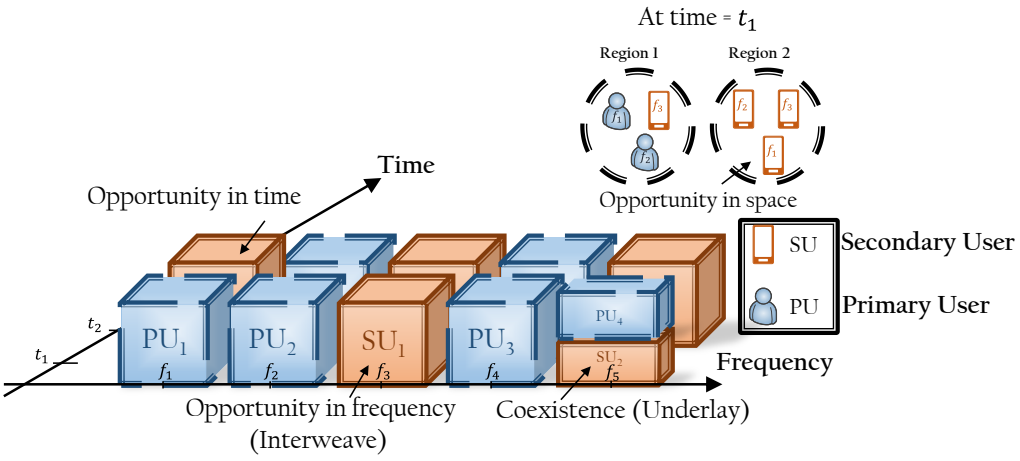


Fig. 1.1: Example Cognitive Radio Network depicting primary and secondary users [3].

## 1.1. Key System Requirements

To be useful, the spectrum scanners have certain key requirements as listed below:

1. Wideband operation and high selectivity – Since most applications of interest cover a wide frequency span, the spectrum scanner needs to provide wideband local oscillator (LO) tunability to scan through the entire spectrum. In addition to this, to cater to varying spectrum scenarios and standards, the resolution bandwidth (RBW) needs to be programmable as well. The bandwidth programmability can also help on-the-fly trade-off between the analog and subsequent digital RBW based on the available hardware and system requirements. Sharp filtering would also be desired to reliably isolate and detect the signals of interest.

2. High linearity – Non-linearity in the system creates additional, undesired tones that can lead to false detection. For instance, two out-of-band tones when subjected to a non-linear scanner can produce a third-order intermodulation tone that may fall in the band of interest. Hence a good scanner needs to be highly linear. Since most practical circuits are dominated by third-order non-linearity, this translates to having a high $3^{rd}$ order input-intercept point (IIP3).

3. High sensitivity – The scanners should be able to detect extremely weak signals. Thus it is important to ensure that the scanner circuitry doesn't add too much noise of its own to the signal band of interest. It should be noted that unlike traditional receivers, since the scanners need to detect only the presence or absence of a signal in most cases, a trade-off exists between the scanner sensitivity and sensing time. A higher sensing time can help detect weak signals, with the limit to the detection provided by the "SNR-wall" [4], [5], i.e. beyond a certain signal-to-noise ratio (SNR), the signal cannot be detected even if infinite number of samples are used.

Signal processing techniques to lower the SNR-wall have been employed in some spectrum scanners [6].

4. Low sensing time – Since the spectrum being sensed maybe dynamically changing, it is important to ensure that the sensing time of the scanner is low. In addition, the sensing time presents a tradeoff with the system throughput wherein increased sensing time can lead to lower throughput [7].

5. Low power – Spectrum scanners will form part of bigger systems and hence should incur a low power overhead.

## 1.2. Prior Art

### *1.2.1 Conventional Techniques*

Conventional spectrum sensing involves either a serial or parallel spectrum scan [8], [9], [12], wherein the LO is swept in the analog and the energy of each band is detected in the digital after being digitized using an Analog-to-Digital converter (ADC). This energy is then compared to a specified threshold (specified for a desired probability of detection and false alarm) to determine the presence or absence of a signal [5][1]. Two of the general conventional approaches are described below:

[1] This is for the simple energy detector. More complicated detection techniques can also be used providing different detection SNR vs sensing trade-offs.

*ADC + Digital FFT*

One approach to spectrum scanning would be to use a Nyquist-rate ADC followed by an FFT block, as shown in Fig. 1.2. This approach reduces the scan time for the spectrum, and can easily provide programmable RBWs but would require a prohibitively large aggregate ADC sampling rate (proportional to the input spectrum span) and a large dynamic range. For instance, in the example spectrum shown in Fig. 1.2 the ADC's need to run at $2F_S$ which can be very high for a wideband spectrum. This would in turn incur a very high power cost making it impractical to implement since analog-to-digital converter performance is improving far too slowly [14].

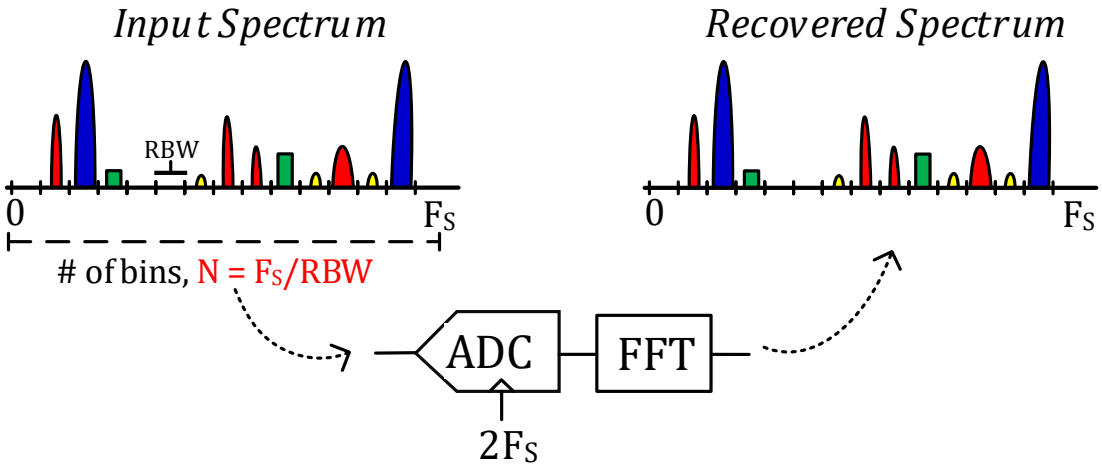


Fig. 1.2: ADC + FFT for direct digital spectrum capture.

*Analog FFT*

Another approach to spectrum scanning is to employ a receiver-like structure [8], [9], [12], like the one shown in Fig. 1.3. A low noise amplifier (LNA), a down-conversion mixer, an analog low-pass anti-aliasing filter, and an ADC are typically employed to isolate and digitize a narrow spectral bin for subsequent FFT-based energy detection and thresholding [5]. The mixer's local oscillator (LO) frequency is swept to scan the spectrum. However, since the LO is typically a square wave, the conventional spectrum scanner suffers from poor harmonic rejection (i.e. suppression of signals that mix with the LOs harmonics). Moreover, since the low-pass filter needs to be very linear and have a sharp response, it is usually realized using active components. These requirements translate into an increased power dissipation to achieve a desired dynamic range.

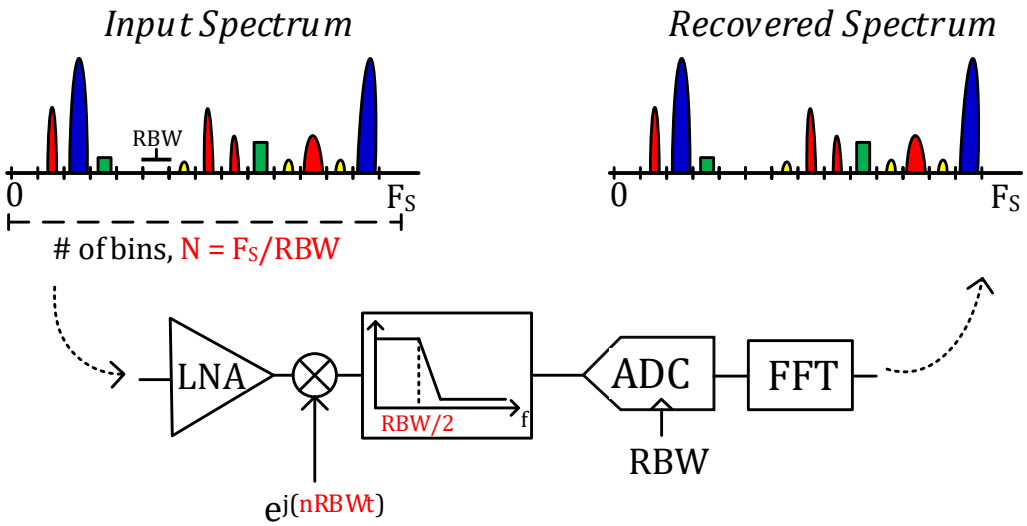


Fig. 1.3: Spectrum analyzer employing a receiver-like structure - Analog FFT.

### *1.2.2 Compressive Sampling-based Scanner*

Compressive sampling (CS) relies on the assumption that the spectrum to be sensed is sparsely populated. In this case, the information bandwidth is much smaller than the total signal bandwidth and hence sub-Nyquist sampling can be used to recover the signal. Incoherent measurements are obtained by mixing the wide-band (but sparse) RF signal with independent, unique pseudorandom noise sequences, as shown in Fig. 1.4, that fold the RF signal into narrowband baseband channels. These scanners then rely on complex digital signal processing to identify the active bins from these samples. A CS-based scanner was demonstrated in [15], [16]. This approach to spectrum sensing significantly reduces the scan time, but does not really provide a fair comparison to the traditional approaches for the following reasons:

i. It only works for sparse spectrum, a scenario which will not always hold true.
ii. When pushing to minimize the required sampling rate, CS requires sharp filters [17] that incur a high power cost. The solution in [15] relies on additional off-chip filtering after the PN sequence mixing to achieve this.
iii. The signal processing needed for signal recovery in CS adds a huge power overhead as compared to the FFT-based energy detection. For instance, the solution in [15] estimates the power consumption to double if the DSP processing is included. However, it should be noted that due to their significantly lower scan time requirement than traditional approaches, this work can lead to a lower energy consumption. It should also be noted that these numbers have assumed only 3 active bins among the 50 bins in the desired spectrum span.

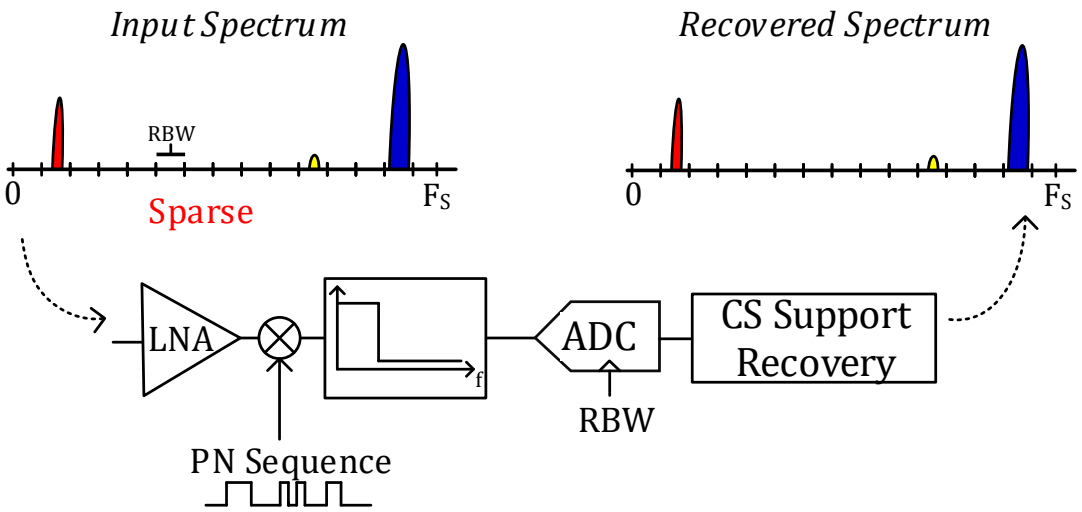


Fig. 1.4: Example architecture for a compressing sensing based spectrum analyzer.

# Chapter 2

## Passive, Linear, Periodically Time-Varying Filter based Spectrum Scanner

We propose to use a passive, linear periodically time-varying (LPTV) filter based approach to spectrum sensing that can ensure linear, sharp and programmable filtering. At the heart of our spectrum scanner is a passive LPTV circuit shown in Fig. 2.1. It is a square wave mixer followed by a simple 1st order RC circuit whose capacitor voltage is sampled uniformly at a rate, $F_S = 1/T_S$. The primary innovation is that the resistor $R$ is varied periodically with a period $T_S$ i.e. $R(t) = R(t + T_S)$. As shown later in this chapter, with the square wave mixer disabled i.e. with $p(t) = 1$, this sampled LPTV RC circuit realizes an equivalent low-pass filter (LPF) with a very sharp frequency response; with the square wave mixer enabled, it realizes true band-pass filters (BPF) with inherent harmonic rejection. In contrast, *time-invariant* passive filters, especially those without inductors, can only achieve limited filter sharpness whereas conventional active filters consume high power and are not as linear.

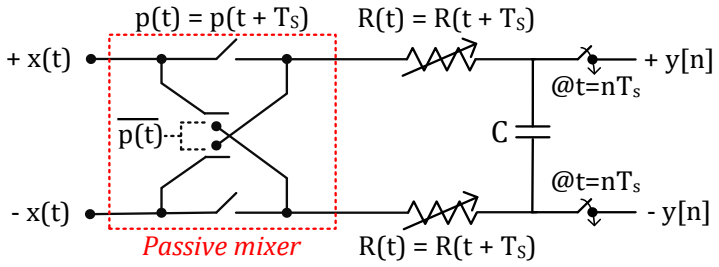


Fig. 2.1: LPTV RC filter.

The central idea behind these periodically time-varying RC filters was first described in signal processing terms in [18] where the technique was referred to as “Filtering by Aliasing” (FA). Early proof of concept sharp LPTV filters were shown in [19]. Note that LPTV circuits are not fundamentally new. Mixers, continuous-time delta-sigma modulators, and even the humble periodic sampler are technically LPTV circuits. This work is different, however, in the sense that it investigates and advocates the use of time-varying circuit components.

## 2.1 Operation of the LPTV RC Filter

For simplicity, we start by considering the low-pass version, i.e. Fig. 2.1 without the upfront passive mixer i.e. with $p(t) = 1$. The output of the linear time-varying system can then be written as

$$y(t) = \int_0^\infty h(t,\tau)x(t-\tau)d\tau \qquad (2.1)$$

where $h(t,\tau)$ is the two-dimensional impulse response of the circuit; specifically, $h(t,\tau)$ is the response at time "$t$" for an impulse applied at time "$t-\tau$". For an LPTV system that varies with a period $T_S$, like the one in Fig. 2.1, $h(t,\tau)$ is periodic i.e. $h(t,\tau) = h(t+T_S,\tau)$. The samples of the output, $y(nT_S)$, are therefore given by

$$y(nT_S) = \int_0^\infty h(nT_S,\tau)x(nT_S-\tau)d\tau = \int_0^\infty h_{eq}(\tau)x(t-\tau)d\tau\Big|_{t=nT_S} \qquad (2.2)$$

where $h_{eq}(\tau) \stackrel{\text{def}}{=} h(nT_S,\tau) = h(0,\tau)$**.** In other words, sampling the output of a $T_S$-periodic LPTV network periodically at $T_S$ may be thought of as sampling the output of an equivalent LTI network with impulse response, $h_{eq}(\tau)$, as shown in Fig. 2.2.

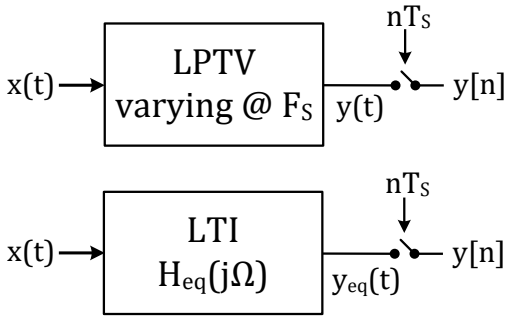


Fig. 2.2: Sampled LPTV system and the equivalent LTI system.

The equivalent LTI filter impulse response, $h_{eq}(\tau)$, can be derived using the "adjoint" of the circuit, as described for general sampled LPTV circuits in [20]. In our case, the circuit is simple enough that $h(t,\tau)$ and hence, $h_{eq}(\tau) = h(0,\tau)$, can be directly evaluated with ease. As shown in Appendix 2.3.1,

$$h_{eq}(\tau) = \frac{1}{R(-\tau)C} \exp\left(-\int_0^{\tau} \frac{du}{R(-u)C}\right) \qquad (2.3)$$

Note that if $R(-\tau)$ is held constant, we get an exponentially decaying impulse response and just a simple LPF with 1st order roll-off as expected. In contrast, it turns out that periodically varying $R$ allows us to design $h_{eq}(\tau)$ in such a way that the equivalent LPF has a sharp characteristic, as shown in Fig. 2.3. Note from (2.2.) that whenever $R(-\tau)$ is large (or small), $h_{eq}(\tau)$, will be accordingly small (or large). Consequently, the example sharp LPF's impulse response can be realized by varying $R(-\tau)$ as shown in Fig. 2.3(b), where it can be noted that $R(-\tau)$ is large for $\tau \approx 0$ and $\tau \approx T_S$ but small at intermediate values. Thus, when compared to using a fixed resistor, a much sharper filter response is achieved. In addition, now the resistor variation can also be used to provide programmability in terms of both stop-band attenuation and filter roll-off, as illustrated later.

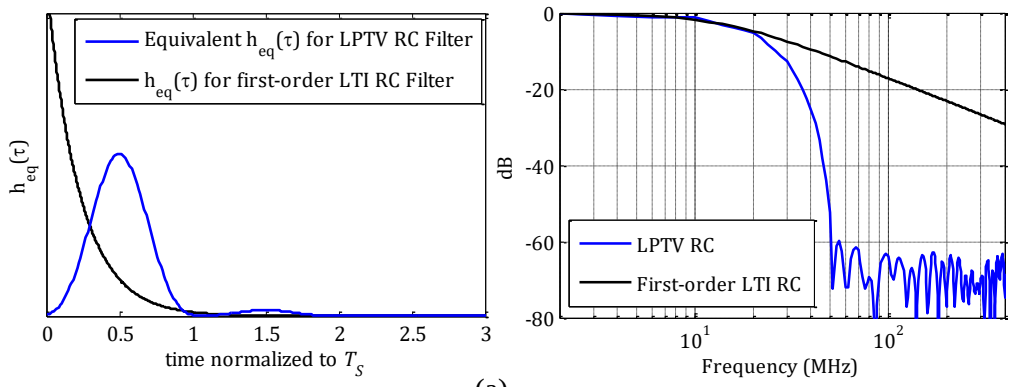


(a)

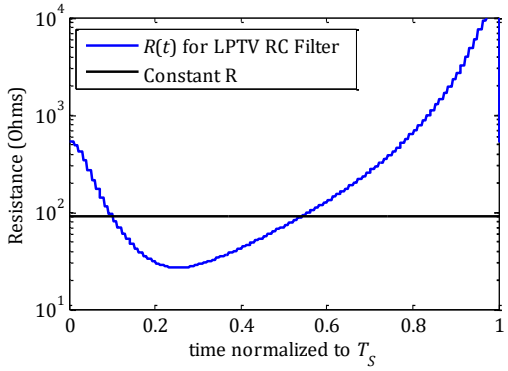


(b)

Fig. 2.3: (a) Example impulse response $h_{eq}(\tau)$ for a sharp low-pass filter; (b) Resistor variation resulting in the desired $h_{eq}(\tau)$.

An intriguing and insightful alternative explanation can be obtained by considering the circuit operation, again without the passive mixer, in frequency domain. First note that, essentially, a variable current, $i(t)$, is integrated onto a capacitor:

$$i(t) = \frac{x(t)-y(t)}{R(t)}; \quad y(t) = \frac{1}{C}\int_{-\infty}^{t} i(\tau)d\tau \qquad (2.4)$$

The signal processing operations are depicted in Fig. 2.4(a), including the subsequent sampling operation. Momentarily ignore the discharging current, $y(t)/R(t)$, for ease of explanation, as shown in Fig. 2.4(b). This assumption is reasonable at least for signals well outside the passband

of the LPF. The role of $R(t)$ is now clear: it effectively serves as a variable gain, $1/R(t)$. The discharging current, $y(t)/R(t)$, is, of course, not negligible, particularly for in-band signals. Section 2.2 derives the accurate filter response and design equations including the discharging current. The central intuition described below remains valid.

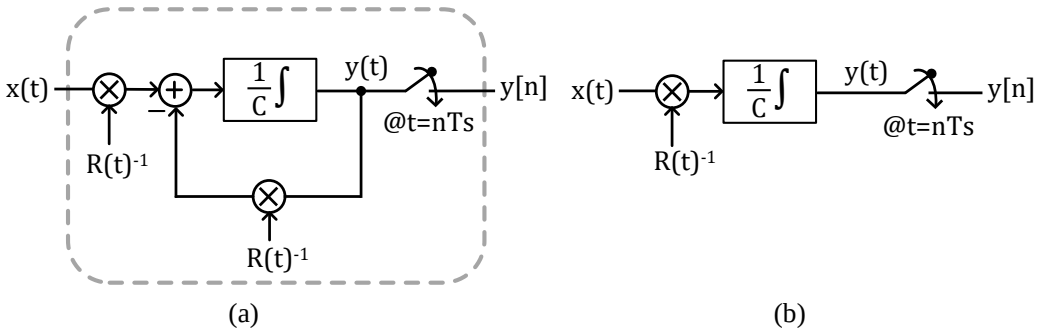


Fig. 2.4: (a) Equivalent signal processing operations for the LPTV RC circuit; (b) Approximate model for intuitive understanding.

The effect of the periodically time-varying resistor, $R(t)$**,** is to essentially "spread/mix" the input with a periodic signal, $d(t) \approx 1/R(t)$, prior to filtering (integration) and subsequent sampling. Consider the frequency domain operations illustrated in Fig. 2.5. The figure shows an example spectrum $X(f)$ of $x(t)$, example Fourier Series coefficients $D_m$ of the periodic $d(t)$, and the integrator response, $H(f)$. As shown, spreading by $d(t)$ produces several, frequency-translated copies of the input spectrum that are weighted by $D_m$. These copies are further selectively weighted by the integrator. Subsequent sampling causes these various copies to alias into the $[-0.5/T_S, +0.5/T_S)$ frequency band. The various $D_m$ (and hence $d(t)$) can be chosen such that the in-band signals are un-attenuated whereas the aliases of the out-of-band signals cancel each other out or are heavily suppressed. Hence the moniker, Filtering by Aliasing [18]. Note that the frequency selectivity of the integrator is essential to the FA concept. Without it, the subsequent

aliasing would affect all the signals equally, and it would be impossible to make the copies of the in-band signal alias constructively while making those of the out-of-band signal alias destructively. Note also that, in a general FA system, the integrator can be replaced by other simple, but frequency selective, filters such as 1st or 2nd order RC filters etc.

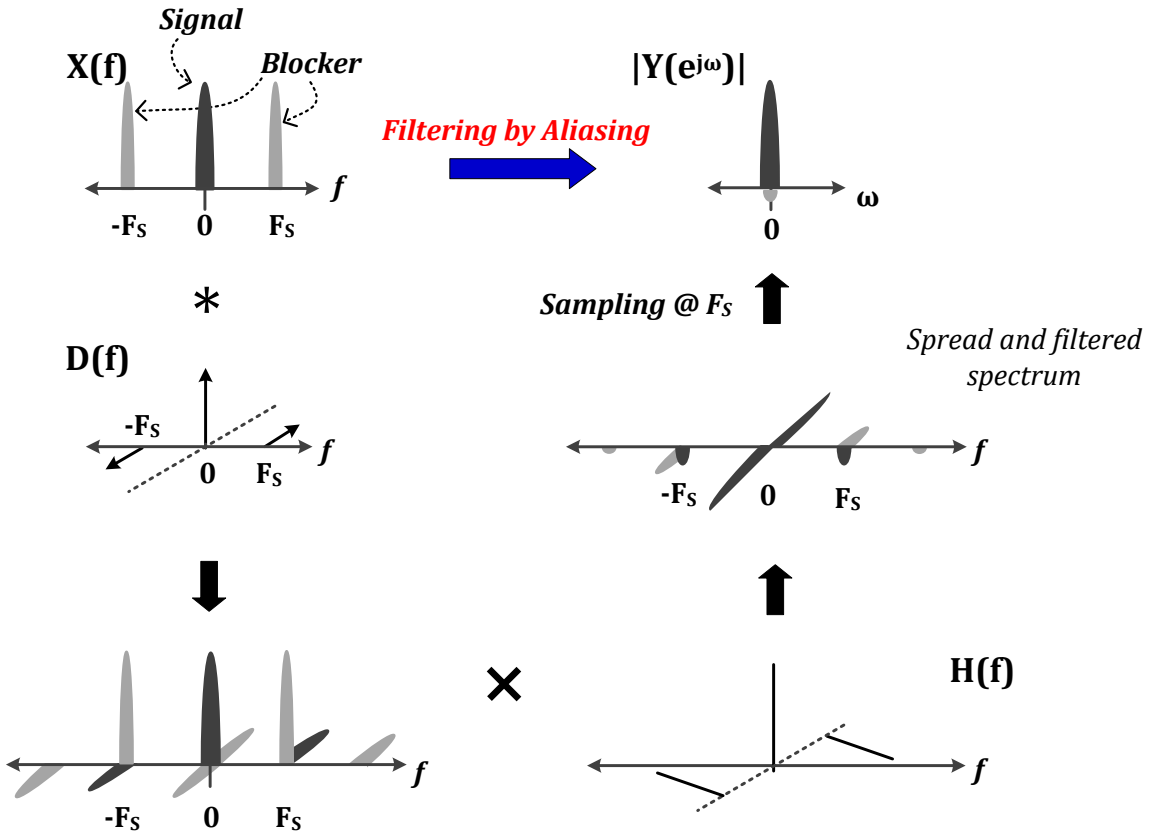


Fig. 2.5: Frequency-domain operations of the FA technique using an example input spectrum, $X(f)$ and spreading signal, $D(f)$. Please note that just a simple example is used here for illustration purposes.

### *2.1.1 LPTV RC Filter with Upfront Passive Mixer*

Consider the LPTV RC filter shown in Fig. 2.1 again, but now with the passive mixer enabled and driven by a binary waveform, $p(t)$. Assume that $p(t)$ is also periodic and has the same period as $R(t)$ so that we still have a sampled LPTV system with the sampling and repetition period, $T_S$, as before. Proceeding just like before, but using $x(t)p(t)$ instead of $x(t)$ in (2.1) and (2.2), an equivalent sampled LTI system can be readily derived with effective impulse response given by

$$g_{eq}(\tau) = \frac{p(-\tau)}{R(-\tau)C}\exp\left(-\int_0^{\tau}\frac{du}{R(-u)C}\right) = h_{eq}(\tau)p(-\tau) \qquad (2.5)$$

The upfront mixer i.e. the choice of $p(t)$ allows an additional degree of freedom in the design of sharp filters. Foremost, notice from (2.3) that $h_{eq}(\tau) \geq 0$. The binary (±1) waveform $p(t)$ allows $g_{eq}(\tau)$ to be positive or negative thereby allowing even sharper filters, if required[2]. More importantly, the passive upfront mixer allows realizing very sharp band-pass filters using an LPTV RC LPF, as described next.

*Bandpass Filters without Harmonic Images*

Suppose that resistor variation $R^{LP}(t)$ realizes a sharp equivalent LPF with impulse response, $h_{eq}(\tau) = h^{LP}(\tau) \geq 0$. Setting $p(t) = sgn(\cos(2\pi F_C t))$ where $F_C$ is an integer multiple[3] of $F_S$, results in an equivalent LTI filter response, $G_{eq}(f)$, that contains copies of the sharp LPF response, $H_{eq}(f)$, translated to $f = \pm F_C$ effectively realizing sharp BPFs. This makes intuitive sense owing

[2] There may be an attendant in-band signal loss, and for the sake of simplicity, this option is not considered anymore in this paper.

[3] $F_C$ does not have to be an integer multiple of $F_S$ for band-pass operation. However, it is assumed to enable harmonic rejection as described.

to the similarity with mixer-first approach. However, since $p(t)$ also contains the harmonics of $F_C$, such square-wave mixing results in undesired band-pass images at the harmonics, just like in conventional mixer-first approach.

Interestingly, these harmonic images can be eliminated in the LPTV RC filtering technique using a simple trick. What is desired is true sinusoidal multiplication of the input, $x(t)$. Since the square-wave mixer only multiplies by the "sign" of the sinusoid, $p(t) = sgn(\cos(2\pi F_C t))$, we appropriately weigh the input according to the envelope of the sinusoid using the variable $R(t)$. Specifically, we choose a new resistor variation, $R(t)$, such that $h_{eq}(\tau) = |\cos(-2\pi F_C \tau)| h^{LP}(\tau)$. It follows that the impulse response of the equivalent LTI filter is $g_{eq}(\tau) = h_{eq}(\tau)p(-\tau) = \cos(-2\pi F_C \tau)\, h^{LP}(\tau)$. Consequently, $G_{eq}(f) = 0.5 \cdot [H^{LP}(f - F_C) + H^{LP}(f + F_C)]$, a true band-pass filter without harmonic images. Fig. 2.6 illustrates the effective BPF with harmonic suppression.

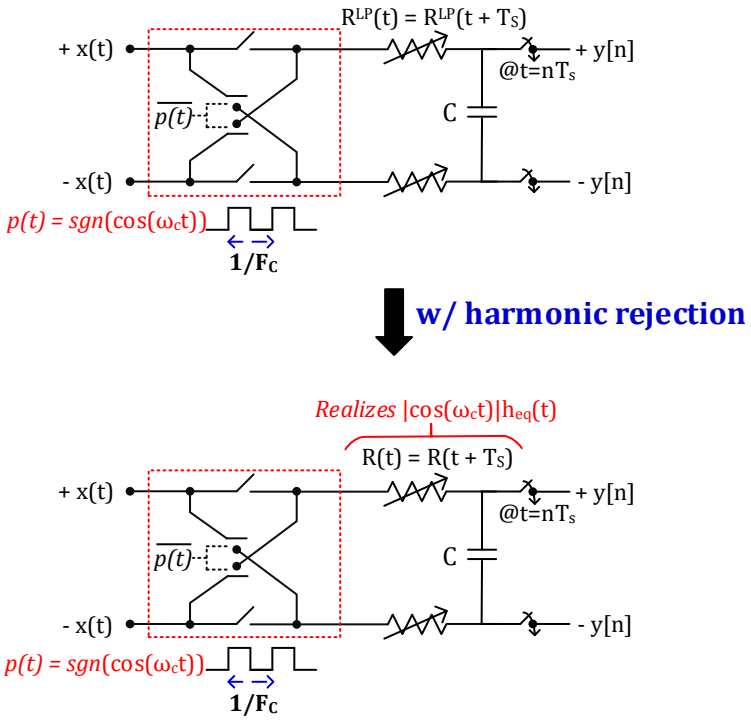

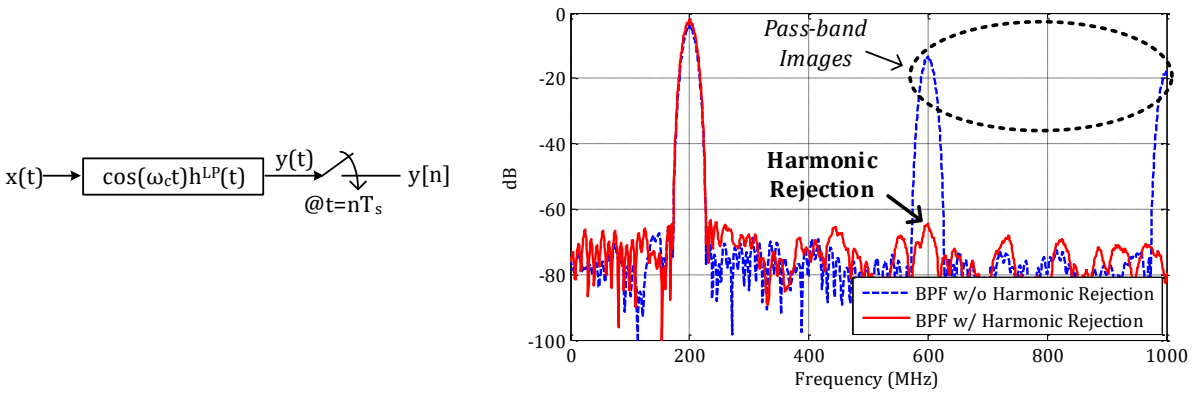


Fig. 2.6: Band-pass filters with sine-wave mixing for harmonic rejection using the LPTV RC filter, and its equivalent model.

## 2.2 Design of the LPTV RC Filter

Previous sections, especially equation (2.3), do not readily suggest how to quantitatively choose $R(t)$ so as to achieve a desired impulse response $h_{eq}(\tau)$. Towards this purpose, we restrict our attention to the practical case where $R(t)\ and\ p(t)$ are varied in time-steps[4] of $T_{CLK}$ where $T_{CLK} \ll T_S$. Accordingly, suppose that $R_\eta$ is the repeating sequence of resistor values with period $K = T_S/T_{CLK}$ that determines the periodic resistor variation $R(t)$ i.e. $R_\eta = R(\eta T_{CLK})$ where $\eta = 0,1,2,\ldots$. Similarly $p_\eta$ represents the binary mixer control waveform[5]. For

[4] It is possible to realize $R(t)$ as a continuously varying resistor, perhaps using a transistor in triode region of operation. However, from a linearity point of view, it may be easier and preferable to vary it in a discrete manner, using a switchable bank of resistors as described in Chapter 3.

[5] While not necessary, we discretize the mixer switching waveform, $p(t)$, at the same rate as (and in sync with) the resistor variation, $R(t)$. This avoids synchronization errors between $p(t)$ and $R(t)$, which may otherwise degrade filter performance including harmonic rejection.

instance, for a BPF at $F_C$, $p_\eta = sgn(\cos(2\pi F_C \eta T_{CLK}))$ where $F_C$ is an integer multiple of $F_S$. Below, we derive an expression for the equivalent filter response, $G_{eq}(f)$, in terms of $R_\eta$ and $p_\eta$.

Since both $R(t)$ and $p(t)$ are varied in steps of $T_{CLK}$, it follows from (2.3) that both $h_{eq}(\tau)$ and $g_{eq}(\tau)$ can be closely approximated by a zero-order hold interpolation of their respective samples, $h_{eq,\eta} \stackrel{\text{def}}{=} T_{CLK} h_{eq}(\eta T_{CLK})$ and $g_{eq,\eta} \stackrel{\text{def}}{=} T_{CLK} g_{eq}(\eta T_{CLK}) = p_\eta h_{eq,\eta}$. For example,

$$g_{eq}(\tau) \approx \sum_{\eta=0}^{\infty} p_\eta h_{eq,\eta}\, g_0(\tau - \eta T_{CLK}) \;\; where \; g_0(\tau) = \begin{cases} 1/T_{CLK}, & 0 \le \tau < T_{CLK} \\ 0, & else \end{cases} \qquad (2.6)$$

Fig. 2.7 illustrates this using an example low-pass $h_{eq}(\tau)$ variation. From (2.2.), the samples $h_{eq,\eta}$, can be readily shown to be:

$$h_{eq,\eta} = \frac{T_{CLK}}{R_{-\eta} C} e^{-\sum_{k=0}^{\eta-1} \alpha_k} = \alpha_\eta \prod_{k=0}^{\eta-1} e^{-\alpha_k} \approx \alpha_\eta \prod_{k=0}^{\eta-1} (1 - \alpha_k), \forall\, \eta = 0, 1, 2, \ldots \qquad (2.7)$$

where, $\alpha_k = T_{CLK}/R_{-k}C$ and $R_{-\eta} = R_{K-\eta}$ as it is periodic. Here, we have assumed that $T_{CLK} \ll R_{-k}C$. While technically not required, this would be the most likely scenario.

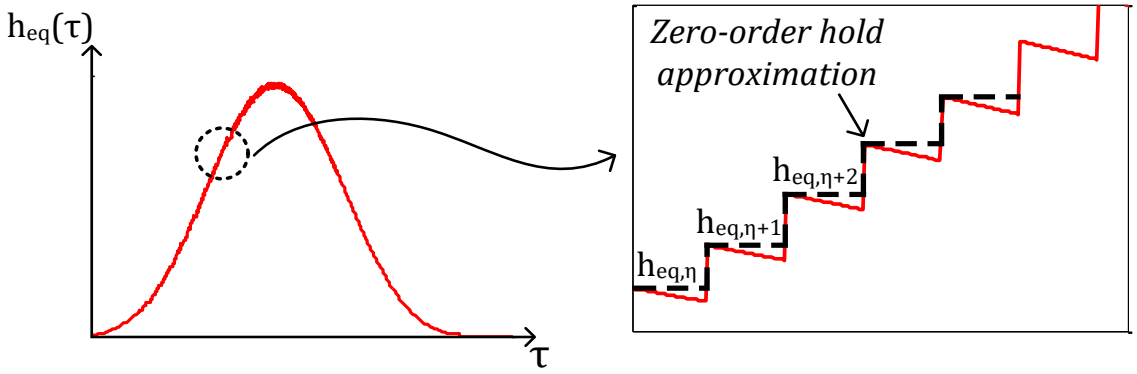


Fig. 2.7: Example $h_{eq}(\tau)$ waveform showing the zero-order hold approximation.

From the periodicity of $R$, it follows that $h_{eq,\eta+K} = \beta h_{eq,\eta}$, where $\beta = \prod_{\eta=0}^{K-1}(1 - \alpha_\eta)$. It can

be shown that the sequence of samples, $g_{eq,\eta}$, represent a discrete-time IIR filter with frequency response

$$G_{eq}\left(e^{j\omega}\right) \stackrel{\text{def}}{\equiv} \sum_{\eta=0}^{\infty} g_{eq,\eta} e^{-j\omega\eta} = \sum_{\eta=0}^{\infty} p_\eta h_{eq,\eta} e^{-j\omega\eta} \cong \frac{\sum_{\eta=0}^{K-1}(p_\eta \alpha_\eta)\left(\prod_{i=0}^{\eta-1}(1-\alpha_i)\right)e^{-j\omega\eta}}{1-\left(\prod_{\eta=0}^{K-1}(1-\alpha_\eta)\right)e^{-j\omega K}} \qquad (2.8)$$

Now, using (2.2.), the LPTV RC system has an equivalent LTI filter frequency response given by:

$$G_{eq}(j\Omega) \approx G_{eq}\left(e^{j\Omega T_{CLK}}\right) \cdot sinc\left(\frac{\Omega T_{CLK}}{2}\right) \qquad (2.9)$$

The LPTV RC filter can therefore be equivalently represented by the model shown in Fig. 2.8. The figure also shows the relationship between $R_\eta$, $p_\eta$ and the impulse response of the equivalent filter, $g_{eq,\eta}$. Filter design can now proceed using traditional means by determining $R_\eta$ and $p_\eta$ needed to realize desired $G_{eq}\left(e^{j\omega}\right)$ and hence, $G_{eq}(j\Omega)$.

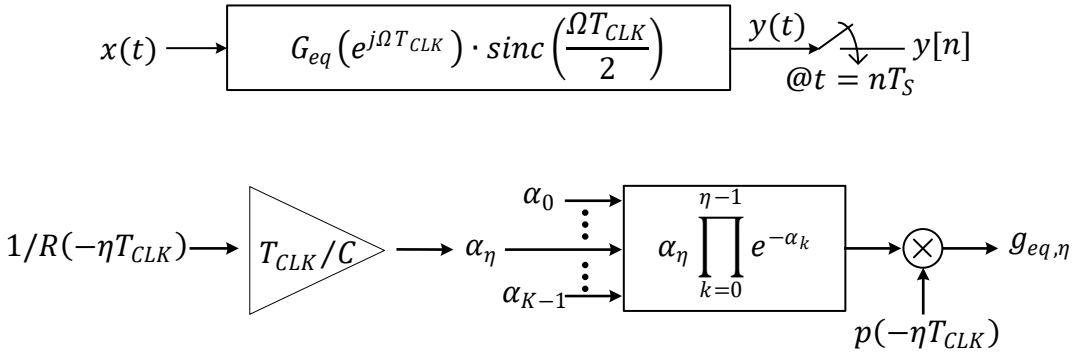


Fig. 2.8: (Top) Equivalent frequency response of the LPTV RC filter; (Bottom) Signal processing operations needed to obtain the $\eta^{th}$ sample ($\eta = 0,1,\ldots$) of the impulse response of $G_{eq}(e^{j\omega})$, where $R(t) = R(t+T_S)$ and $p(t) = p(t+T_S)$ are the periodic resistor and mixer control variations respectively.

Two things are of note. Firstly, the denominator of $G_{eq}(e^{j\omega})$ represents $K$ poles that are equidistant from the origin and evenly distributed from 0 to $2\pi$ in the z-plane, creating an approximate all-pass response for reasonably large $K$ as shown in Fig. 2.9. So, the denominator's effect on the filter suppression or sharpness is not critical.

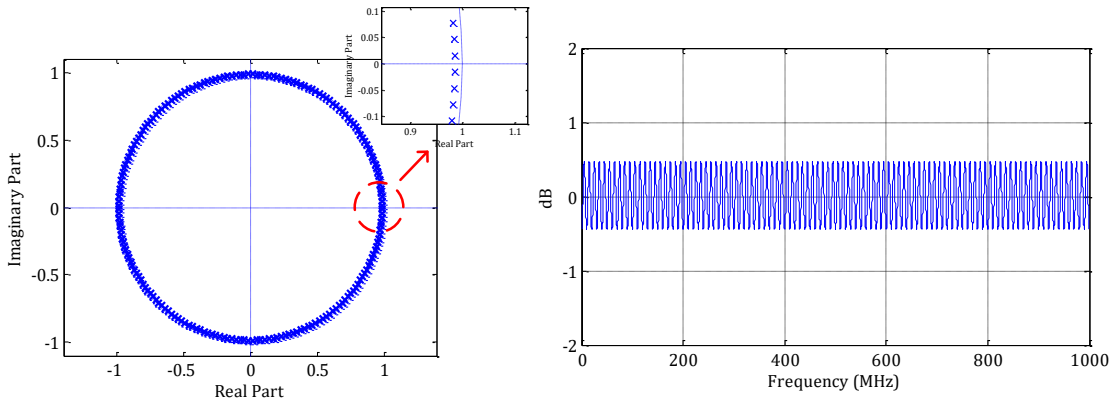


Fig. 2.9: Pole locations (left) and the corresponding filter response (right) due to just the IIR part of the filter response (Eq. 2.8) for an example filter.

Secondly, a BPF with harmonic rejection can be realized by setting

$$p_\eta = sgn(\cos(2\pi F_C \eta T_{CLK})) \text{ and } h_{eq,\eta} = h_{eq,\eta}^{LP} \cdot |\cos(-2\pi F_C \eta T_{CLK})| \quad (2.10)$$

where $h_{eq,\eta}^{LP}$ is the impulse response of an LPF. A detailed design procedure is presented after a discussion of practical considerations in the implementation of the LPTV filter.

Fig. 2.10 shows example low-pass and band-pass filters with their impulse responses and the corresponding resistor variations and filter responses. It can be seen how the resistor variation for harmonic rejection (HR) differs from its low-pass counterpart. Now for each center frequency, a

new resistor (and mixer) waveform can be used to scan different frequency bins in a given frequency span.

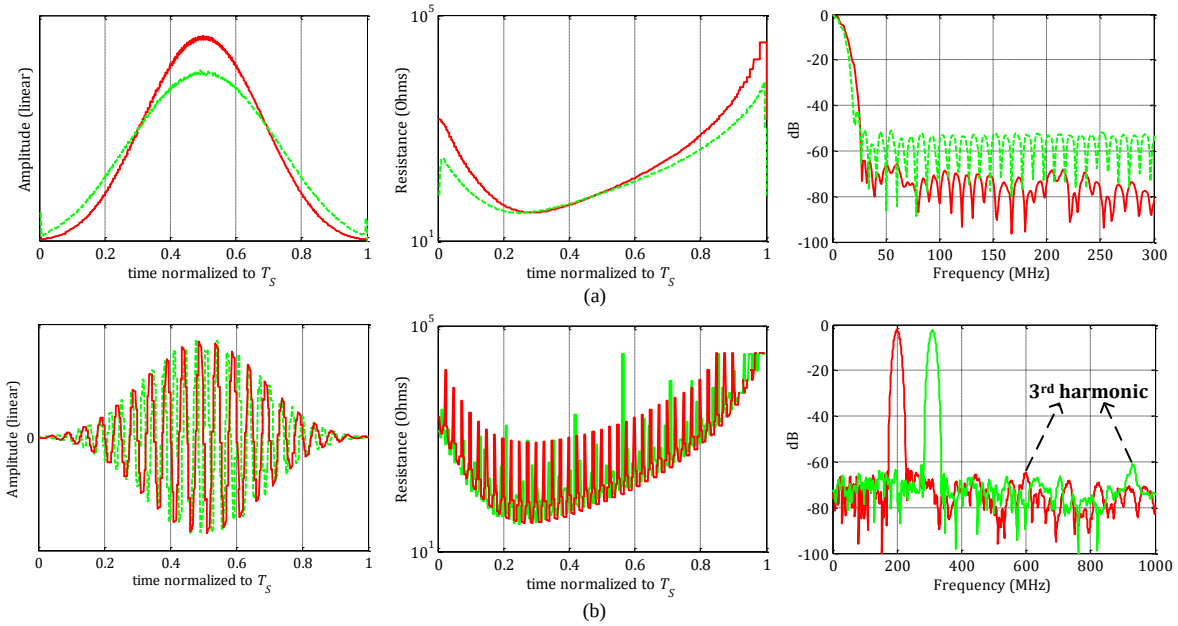


Fig. 2.10: (a) (Left to right) Impulse responses for two example LPF, corresponding R(t) variations and their frequency responses; (b) (Left to right) Impulse response for example BPF at 200MHz and 310MHz, corresponding R(t) variations and their frequency responses with harmonic rejection.

Note that the equivalent LTI filter transfer function can be obtained by other means as well. For instance, as we originally suggested in [18], the integro-differential equations that govern the LPTV RC circuit could be directly discretized using an appropriate integration formula. An alternative, and perhaps more intuitive (to the circuit designer) approach involves a direct time-domain analysis of the simple 1st order RC circuit during each time-step, $T_{CLK}$. Assuming that the input is constant during this small time-step, it is easy to show that

$$y(\eta T_{CLK}) = p_\eta \cdot x(\eta T_{CLK})(1 - e^{-\alpha_\eta}) + y(\eta T_{CLK} - T_{CLK})e^{-\alpha_\eta} \qquad (2.11)$$

where $y(t)$ is the voltage on the capacitor and the two terms in the right-hand side correspond to the simultaneous charging and discharging of the capacitor during the $\eta^{th}$ $T_{CLK}$ time-step. Similar expressions for $G_{eq}\left(e^{j\omega}\right)$ can be obtained by repeated application of this equation over successive time-steps.

### *2.2.1 Practical Considerations*

Since the LPTV resistance, $R(t)$, is assumed to be varied only at a finite rate, $F_{CLK} = 1/T_{CLK}$, it will cause filter images to appear at integer multiples of this frequency as shown in Fig. 2.11(a). This is also evident from (2.2.) where $G_{eq}\left(e^{j\Omega T_{CLK}}\right)$ is periodic. Ideally, the switching frequency, $F_{CLK}$, should be as high as possible but practical considerations like power consumption, technology node, etc. limit how high it can be. The images, however are attenuated by the *sinc* filtering (2.2.). It should be noted that since the capacitor voltage is the result of an RC operation and not a perfect sampled-and-held signal, the images at multiples of $F_{CLK}$ are not perfectly nulled. They are however, greatly suppressed. For instance, as shown in Fig. 2.11(a), the first image is nulled by $\sim$50dB. Practical implementations will also inevitably result in less-than-abrupt jumps in $R(t)$ resulting in additional filtering of the switching images, just as in any digital-to-analog converter. Note also that the resistance values can only be varied in finite steps meaning they need to be quantized. Fig. 2.11(b) shows the effect of resistor quantization on the filter response. As can be seen, 10-bit resistor quantization is sufficient to achieve $\sim$70dB stop-band attenuation together with a transition bandwidth that is 4x the filter BW.

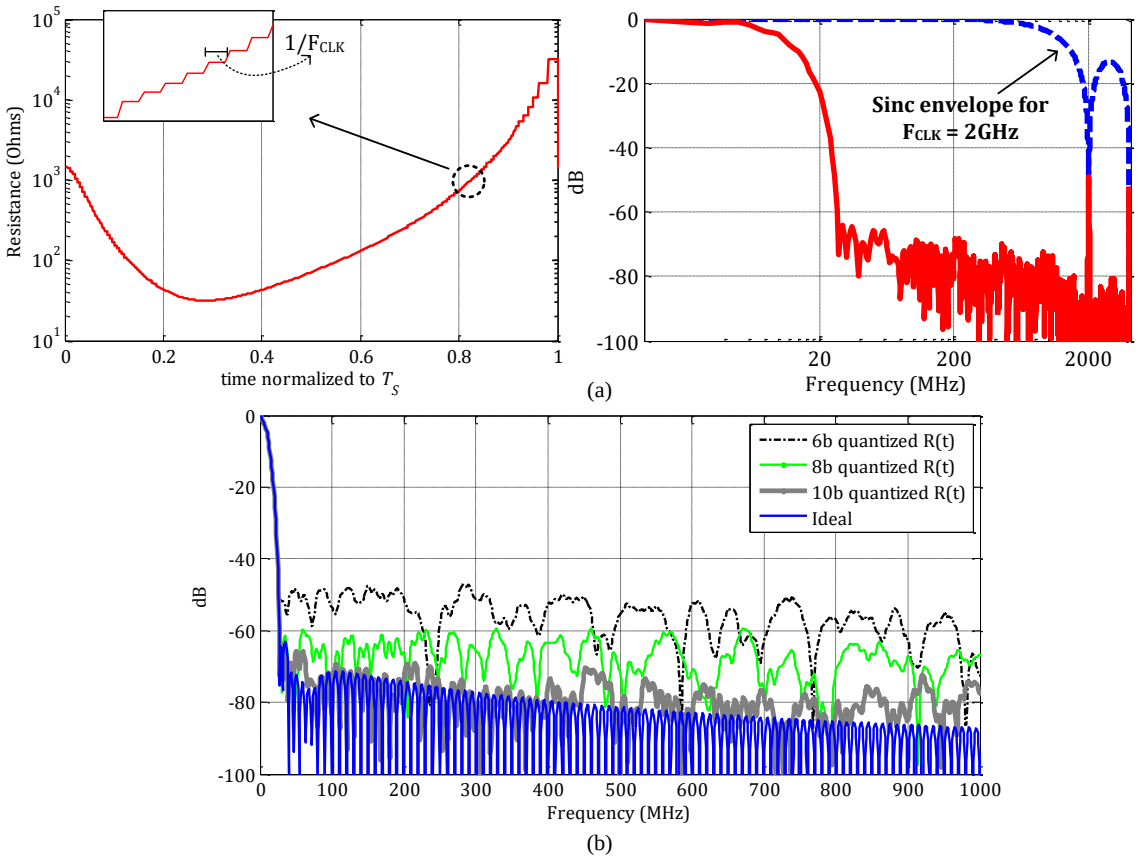


Fig. 2.11: (a) Finite-rate of resistor variation resulting in sinc-shape; (b) Effect of resistor quantization on filter response.

The mean square noise voltage across the capacitor of the LPTV RC filter, and hence, in its output samples is kT/C, just as in an LTI RC filter. Appendix 2.3.2 mathematically proves this, and measurements of the prototype IC described in Chapter 3 confirm it. As an example, consider a sharp LPTV RC filter with a $-3$dB bandwidth of 7MHz. With $R(t)$ variation chosen such that the $min(R(t) + R_S) = 30\Omega$, a capacitor value, $C = 470$pF gives the desired sharp filter shown in Fig. 2.12 and results in an output noise of $3\mu V_{rms}$. In comparison, a 1st order RC filter needs $C = 910$pF with a constant resistance of $25\Omega$ to give a filter with the same $-3$dB bandwidth. This has lower noise, but only a 20dB/dec roll-off. A 2nd order RC-RC filter can achieve close to 40dB/dec

roll-off (as shown in Fig. 2.12), but needs much lower output capacitance, $C_2$ which leads to higher noise. Compared to this, the LPTV RC filter has better sharpness, lower noise, and less total capacitance. A thorough discussion of the benefits offered by LPTV filters in the context of filter sharpness vs noise trade-off, compared to other passive filters, is the subject of another work.

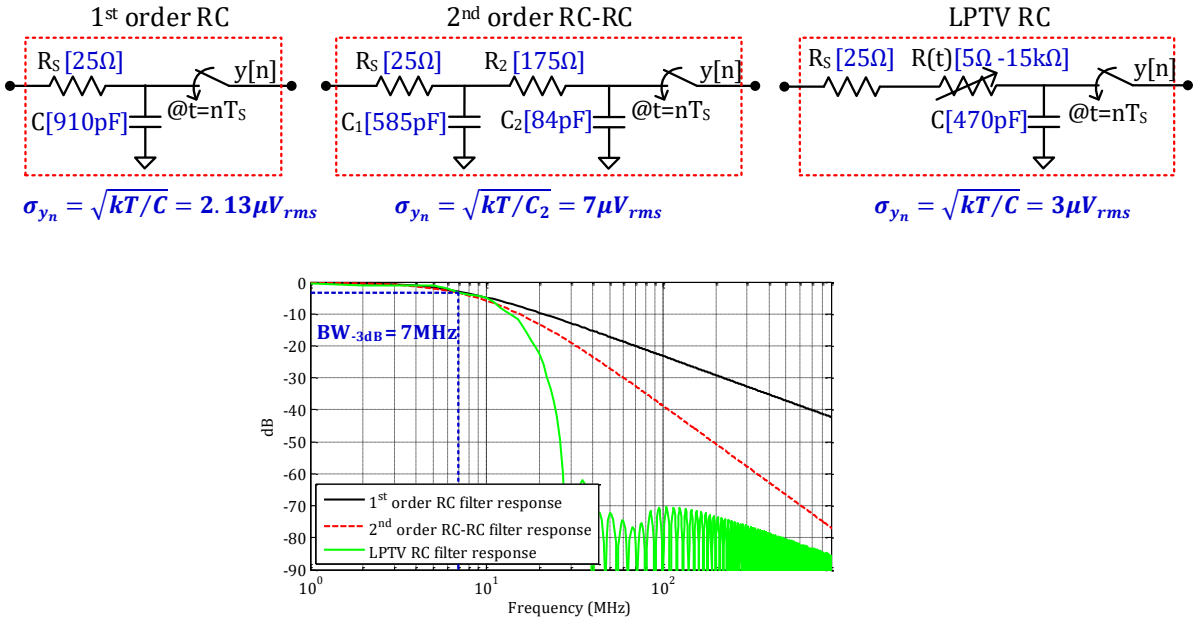


Fig. 2.12: Comparison of noise-sharpness tradeoff between passive LPTV and LTI RC filters.

Additionally, from a noise tradeoff perspective, in the presence of resistor quantization, the series resistance, $R_S$ also affects the dynamic range requirements for $R(t)$ for different capacitance values. Fig. 2.13 shows two example resistor variations for the same filter. As can be seen, the lower capacitance relaxes the number of bits needed to cover the required resistance variation range.

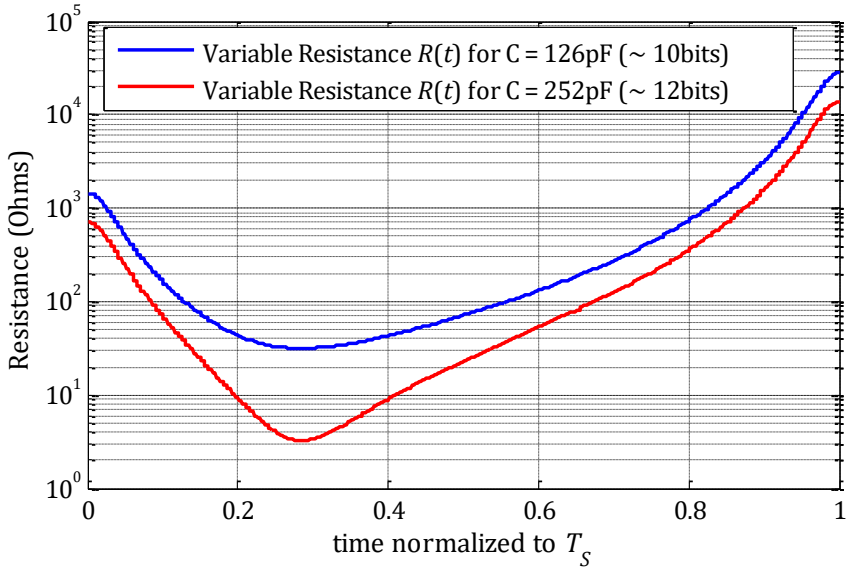


Fig. 2.13: Filter capacitance vs resistor dynamic range requirements in the presence of $R_S$.

### *2.1.1.1 Input Impedance*

It is worthwhile to note that the scanner presents high impedance at its input. It is a time-varying resistance in series with a capacitor. In order to derive the exact expression for the input impedance, we resort to the conversion matrix based analysis of LPTV circuits used in [21].

We start with the differential circuit in Fig. 2.14 with the mixer disabled for the low-pass filter. Similar to the notations used in [21], let us define a frequency vector for the output current, $i_2(t)$ as $\underline{I_2}(\omega) = [I_2(\omega - m\omega_S) \quad I_2(\omega - (m-1)\omega_S) \quad \cdots \quad I_2(\omega + m\omega_S)]^T$ for $\omega \in (\frac{-\omega_S}{2}, \frac{+\omega_S}{2}]$, where $I_2(\omega)$ is the Fourier Transform of the signal $i_2(t)$, $T_S = \frac{2\pi}{\omega_S}$ is the fundamental period of the $R$ variation in the circuit, and $m \to \infty$ is a large positive integer. Similarly, frequency vectors $\underline{V_2}(\omega)$, $\underline{V_1}(\omega)$ and $\underline{I_1}(\omega)$ can also be defined for the output voltage $v_2(t)$ and input voltage $v_1(t)$

and input current $i_1(t)$, respectively. Since $R(t)$ is a periodic signal, it can be expressed using its Fourier Series, resulting in the following Fourier Transform: $R(\omega) = \sum_{l=-\infty}^{\infty} R_l \delta(\omega - l\omega_S)$; where $l$ is an integer and $R_l$ is the coefficient of $e^{jl\omega_S t}$ in the Fourier Series expansions.

As shown in [21], circuit laws can be applied to LPTV systems as well, in the frequency domain. Let **R** denote the conversion matrix for the periodically time-varying resistance $R(t)$. In this case, it is easy to see that the voltage frequency vector, $\underline{V_2}(\omega)$ is given by

$$\underline{V_2}(\omega) = \mathbf{Z_L}\underline{I_2}(\omega) \qquad (2.12)$$

$$\mathbf{Z_L} = [\mathbf{2R} - jC^{-1}\mathbf{\Omega^{-1}}(\omega)]$$

$$\mathbf{R} = \begin{bmatrix} R_0 & R_{-1} & \cdots & \cdots & R_{-2m} \\ R_1 & \ddots & & & R_{-2m+1} \\ \vdots & & R_0 & \cdots & \\ \vdots & \vdots & & \ddots & \vdots \\ R_{2m} & R_{2m-1} & \cdots & \cdots & R_0 \end{bmatrix}; \ \mathbf{\Omega} = diag\{[\omega - m\omega_S \quad \cdots \quad \omega \quad \cdots \quad \omega + m\omega_S]\}$$

where, $R_0, R_1$ ... are the Fourier Series coefficients of the time-varying resistance and $\omega_S = 2\pi/T_S$.

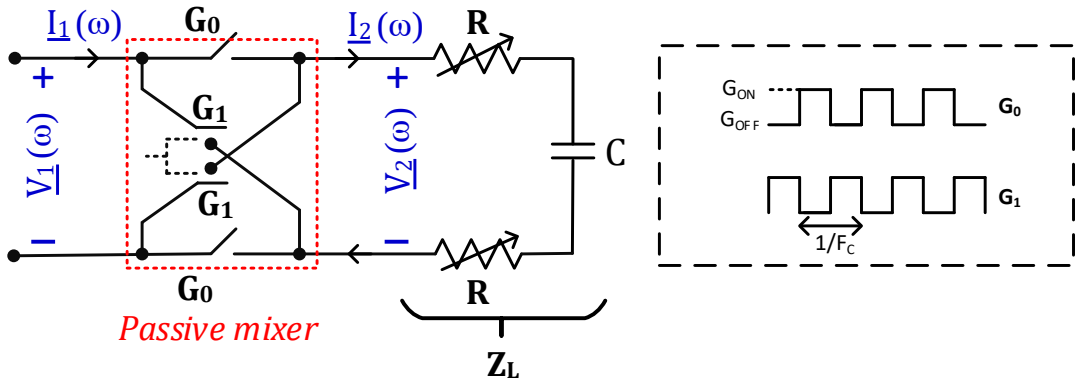


Fig. 2.14: LPTV RC filter with the upfront passive mixer showing the relevant frequency vectors and conversion matrices.

For the low-pass with the mixer disabled, $\underline{V_2}(\omega) = \underline{V_1}(\omega)$ and $\underline{I_2}(\omega) = \underline{I_1}(\omega)$ and therefore the input impedance matrix, $\mathbf{Z_{in}}$ is equal to $\mathbf{Z_L}$. Since impedance, by definition, relates the voltage in a given band, $V_1(\omega + m\omega_S)$ to current in the same band $I_1(\omega + m\omega_S)$, the input impedance of the circuit is given by the diagonal entries of $\mathbf{Z_L}$. Fig. 2.15 shows the input impedance obtained from both the calculation (using Matlab) and Cadence Spectre PSS-PAC simulation. As expected, the impedance is dominated by the capacitance at low frequencies and is equal to the $mean(R(t))$ at high frequencies. For the example shown, the $mean\big(R(t)\big) = 1.68k\Omega$.

For the band-pass filter, with the mixer enabled, we have two additional conversion matrices. The mixer switches in the *through*- and *cross*- paths can be modelled as time-varying conductances, $\mathbf{G_0}$ and $\mathbf{G_1}$ as shown in Fig. 2.14. Just as in [21], KVL and KCL can now be used to determine the relationship between the voltage and current frequency vectors $\underline{V_1}(\omega)$ and $\underline{I_1}(\omega)$ and hence the input impedance. Using conductance matrices for ease of computation, we have

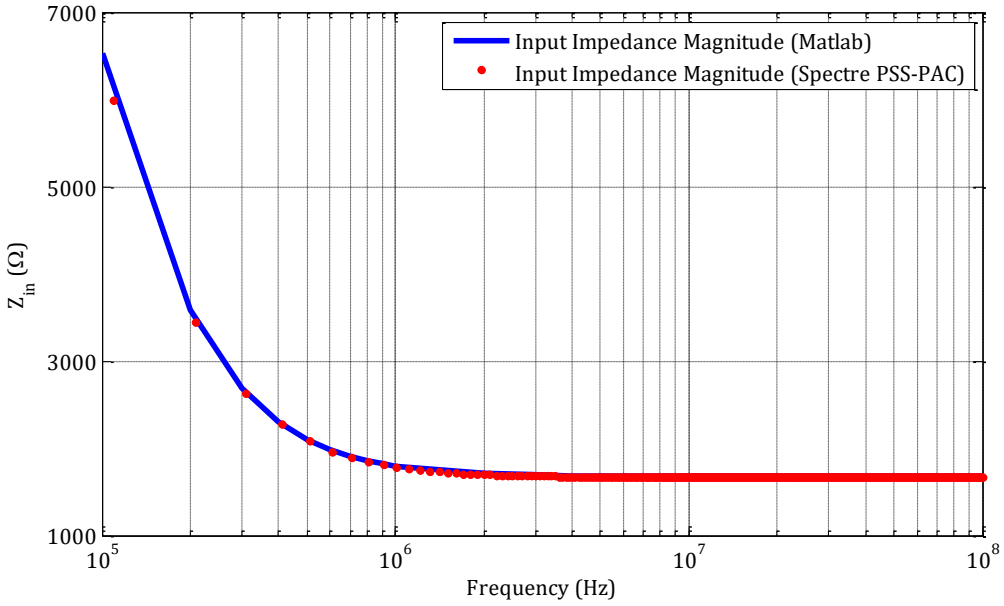

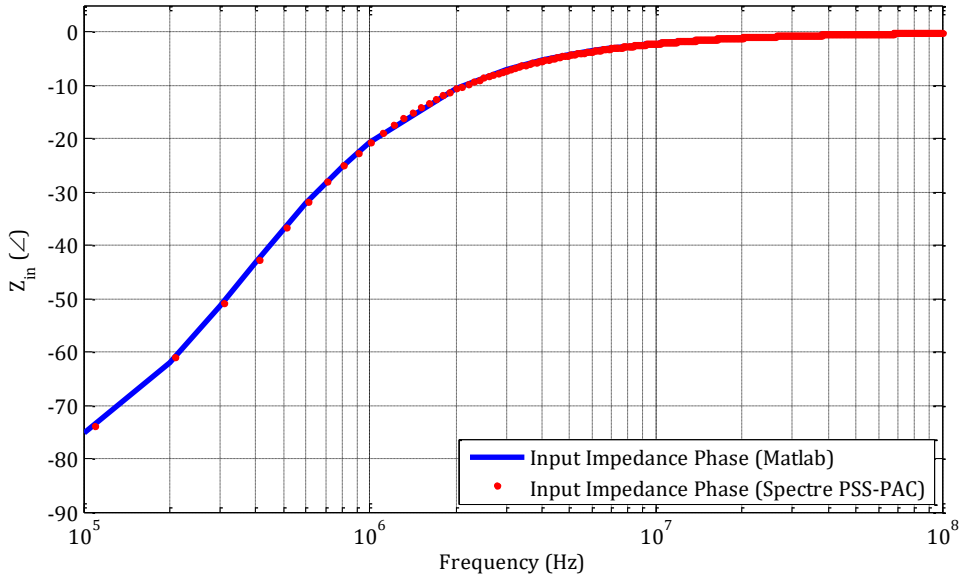


Fig. 2.15: Input impedance for the low-pass LPTV RC filter showing single-ended impedance.

$$\underline{I_1}(\omega) = \frac{(\boldsymbol{G_0+G_1})}{\mathbf{2}}\underline{V_1}(\omega) - \frac{(\boldsymbol{G_0-G_1})}{2}\underline{V_2}(\omega) \qquad (2.13)$$

$$\frac{(\boldsymbol{G_0-G_1})}{2}\underline{V_1}(\omega) = \left(\frac{(\boldsymbol{G_0+G_1})}{\mathbf{2}} + \mathbf{Y_L}\right)\underline{V_2}(\omega) \qquad (2.14)$$

with $\mathbf{Y_L} = \mathbf{Z_L^{-1}}$ and

$$\mathbf{G_0} = \begin{bmatrix} G_{0,0} & G_{0,-1} & \cdots & \cdots & G_{0,-2m} \\ G_{0,1} & \ddots & & & G_{0,-2m+1} \\ \vdots & & G_{0,0} & \cdots & \\ \vdots & \vdots & & \ddots & \vdots \\ G_{0,2m} & G_{0,2m-1} & \cdots & \cdots & G_{0,0} \end{bmatrix}; \mathbf{G_1} = \begin{bmatrix} G_{1,0} & G_{1,-1} & \cdots & \cdots & G_{1,-2m} \\ G_{1,1} & \ddots & & & G_{1,-2m+1} \\ \vdots & & G_{0,0} & \cdots & \\ \vdots & \vdots & & \ddots & \vdots \\ G_{1,2m} & G_{1,2m-1} & \cdots & \cdots & G_{1,0} \end{bmatrix}$$

where $G_{0,0}, G_{0,1}$ ... etc. are the Fourier Series coefficients of the two switching conductances representing the passive mixer. Eliminating $\underline{V_2}(\omega)$ from (2.13) and (2.14) above, the input impedance matrix is given by

$$\mathbf{Z_{in}} = \mathbf{Y_{in}^{-1}} = \frac{(G_0+G_1)}{2} - \frac{(G_0-G_1)}{2}\left(\frac{(G_0+G_1)}{2} + \mathbf{Y_L}\right)^{-1}\frac{(G_0-G_1)}{2} \quad (2.15)$$

From (2.15) above, the input impedance of the LPTV RC filters with the upfront passive mixer is thus given by the diagonal entries of the matrix $\mathbf{Z_{in}}$. Fig. 2.16 shows the input impedance for a BPF at 100MHz obtained from both calculation (using Matlab) and Spectre PSS-PAC simulation. For these results $R_{ON} = 0.1\Omega$ and $R_{OFF} = 1M\Omega$ is used for the mixer switches with $m = 4000$. As can be seen, the impedance away from the LO is $\sim mean\big(R(t)\big) = 3.17k\Omega$ and is capacitive close to the LO. At LO and frequencies very close to the LO (a few kHz), the capacitor behaves as a switched-capacitor resistor and that can be seen from the zero-phase around 100MHz. It should be noted that this resistance value is still very high. The $mean\big(R(t)\big) = 3.17k\Omega$ for this filter. The high input impedance for both the LPF and BPF results in the $S_{11}$ being high as confirmed by the measurements shown in Chapter 3.

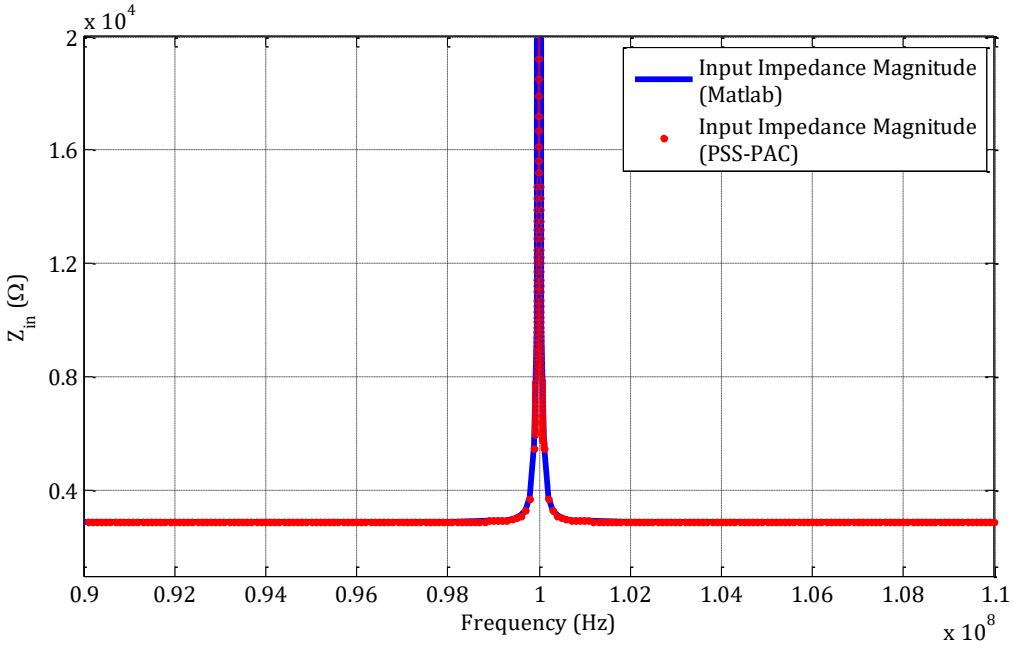

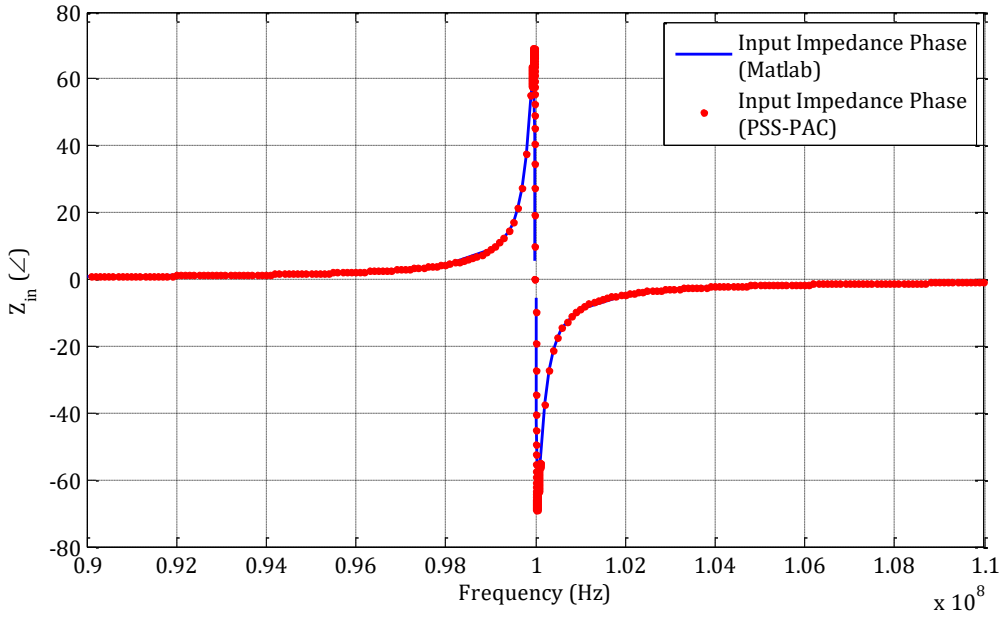


Fig. 2.16: Input impedance for the band-pass LPTV RC filter at 100MHz showing single-ended impedance.

### *2.2.2 Design Procedure*

The design procedure is now illustrated using an example filter design. To enable the scan of a 1GHz spectrum with a 10MHz RBW, we start by choosing $F_{CLK} = 2\text{GHz}$ and design a LPF with bandwidth, $\text{BW} = 5\text{MHz}$. $F_{CLK}$ is chosen to be 2GHz since filter images appear at this frequency, as mentioned in Section 2.2.1. The LPF bandwidth is chosen to be half the desired RBW. The output sampling rate, $F_S$ for these filters is chosen to be $2 \cdot \text{BW}$. Assume that $C$ is chosen large enough to render the sampled output noise variance, $kT/C$, small enough. Assume that the source has a differential source resistance $R_S$. This can be included in the design as $R(t) \stackrel{\text{def}}{=} R_S + R'(t)$, where $R(t) = R(t + T_S)$ is the total periodically varying resistance.

1) Design $K^{\text{th}}$-order FIR LPF, $h_{eq,\eta}^{LP} \geq 0$, with bandwidth, BW, where $K = F_{CLK}/F_S$; e.g., $K = 200$.
2) Set $p_\eta = sgn(\cos(2\pi F_C \eta T_{CLK}))$ and $h_{eq,\eta} = h_{eq,\eta}^{LP} \cdot |\cos(-2\pi F_C \eta T_{CLK})|$ where $F_C$ is the desired center frequency for the BPF.
3) Use (2.7) to compute $\alpha_\eta$ recursively from $\eta = 0$. It can be shown that $\alpha_\eta = h_\eta \prod_{k=0}^{\eta-1} e^{\alpha_k}$.
4) Calculate the resultant $R_\eta$, given $\alpha_\eta$. If $min(R_\eta) \leq R_S$, it is not realizable. So, reduce $C$ and repeat this step, or go to Step 1 and design a relaxed filter.
5) Quantize to chosen number of bits.

Note that the minimum possible $R_\eta$ imposes a tradeoff between the minimum noise and achievable stop-band attenuation for a given number of bits. Hence, a few iterations may be required to achieve target performance. Note also that once an RDAC has been chosen (i.e. number of bits, minimum $R_\eta$), the capacitance $C$ needs to be varied with varying bandwidths.

In this work, convex optimization [22] and spectral factorization [23] are used to find the optimal squared magnitude $|H_{eq}^{LP}(e^{j\omega})|^2$, and the corresponding minimum phase $H_{eq}^{LP}(e^{j\omega})$ and $h_{eq,\eta}^{LP}$. The same LPF is used for all the bins while $F_C$ is swept and accordingly new $h_{eq,\eta}$, $R_\eta$, and $p_\eta$ are calculated. Note that for band-pass filters with HR, $h_{eq,\eta}$ can become very small for some $F_C$. Correspondingly, $R_\eta$ can be very large. However, a 10-bit $R(t)$ variation is sufficient to get good harmonic rejection.

## 2.3 Chapter Appendix

### *2.3.1 LPTV RC Equivalent LTI Filter*

Recall that $h(t,\tau)$ is the response of the circuit at time "$t$" for an impulse applied at time "$t-\tau$". With $x(t)=\delta(t-\tau)$, the initial voltage on the capacitor is related to the resistance value at that instance and given by $y_0 = 1/[R(t-\tau)C]$. This voltage will then decay through varying time-constants as the resistance changes from $R(t-\tau)$ to $R(t)$. Applying KCL at the capacitor node, $y_C(t)$ we have

$$\frac{y_C(t)}{R(t)} = -C\frac{d}{dt}y_C(t) \qquad (2.16)$$

Solving the above differential equation and using the initial condition, $y_0$, we get

$$h(t,\tau) = \frac{1}{R(t-\tau)C}\exp\left(-\int_0^{\tau}\frac{du}{R(t-u)C}\right) \qquad (2.17)$$

The equivalent LTI impulse response is simply $h_{eq}(\tau) = h(0,\tau) = h(T_S,\tau)$.

### *2.3.2 Noise in a Time-Varying RC Circuit*

As shown in [24] and summarized here, even with a time-varying resistance, the mean square noise voltage on the capacitor of the LPTV RC circuit is $\mathrm{kT/C}$, and it is independent of when it is sampled. We start with the autocorrelation of the thermal noise input of the resistor, $E[x(t)x(t+v)] = 2kTR(t)\delta(v)$, where $k$ is the Boltzman constant, $T$ is the temperature in Kelvin and $R(t)$ is the resistance value at a given instance. Then for the output noise power we have,

$$\sigma^2_{y(t)} = E[y(t)^2] = \int_0^\infty h^2(t,\tau) 2kTR(t-\tau)d\tau \qquad (2.18)$$

Replacing $h(t,\tau)$ in (2.18) with equation (2.17) from Appendix 2.3.1, and substituting $u = \int_0^\tau \frac{dv}{R(t-v)C}$, it follows that:

$$\sigma^2_{y(t)} = \int_0^\infty 2KT \frac{1}{C} exp(-2u)du = \frac{\mathrm{kT}}{C} \qquad (2.19)$$

# Chapter 3

## Spectrum Scanner IC and Measurement Results

In this chapter, circuit details and design considerations of the LPTV filter based spectrum scanner IC are described and the measurement results presented. The block diagram of the designed spectrum scanner IC which was implemented in TSMC 1P6M 65nm CMOS process is shown in Fig. 3.1.

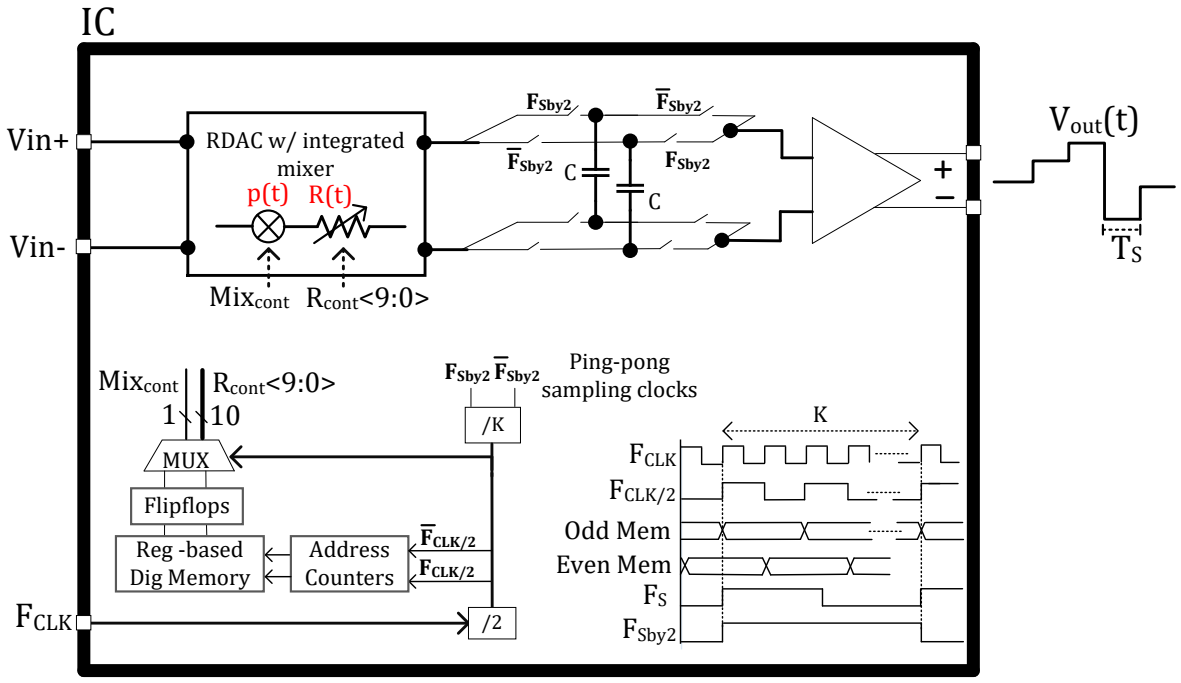


Fig. 3.1: Block diagram of the fabricated spectrum scanner IC.

The main components of the chip are a resistor digital-to-analog converter (DAC) with an integrated mixer, capacitor banks, clock generation circuitry and digital blocks for the resistor and mixer control and for static programmability. In the following sections, each of them is described in detail.

## 3.1 Circuit Design

### *3.1.1 Resistor DAC with integrated mixer*

A straightforward implementation of a resistor DAC (RDAC) with a passive mixer is shown in Fig. 3.2(a) and was realized in [19]. This simple structure suffers from two drawbacks: 1) the upfront mixer switches are subjected to the entire input signal swing which degrades filter linearity, and 2) the high parasitic capacitance associated with the mixer switches leads to unwanted charge loss paths that degrade both stop-band attenuation and HR. The second effect is a result of the mixer switches being sized up so as to not limit the minimum achievable resistance in $R(t)$.

A better RDAC structure with an integrated mixer, shown in Fig. 3.2(b), resolves both issues. This RDAC is implemented differentially and consists of two nominally matched 10-bit resistor ladders. The RDACs consist of binary-weighted *rppoly* resistors in series with transmission gate switches. The switch in each branch is scaled with the resistance in the branch: smaller switches in series with larger resistors. The RDAC is designed to have a minimum resistance of $33\Omega$ with the switch in each branch sized to have an ON-resistance that is 10% of the poly resistance.

The desired resistor variation, $R(t)$ and mixer control, $p(t)$ is obtained by driving the RDAC switches using the 10-bit resistor control, $R_{cont}\langle 9{:}\,0\rangle$ and 1-bit mixer control, $Mix_{cont}$ respectively from the digital block. These controls are generated at $F_{CLK}$ that is nominally set at $2\text{GHz}$ to scan a $1\text{GHz}$ frequency span. The switch in each branch of this new RDAC is controlled by a logical AND between the mixer control, $Mix_{cont}$ and the resistor control $R_{cont}\langle 9{:}\,0\rangle$. This way, depending on the mixer control, either a *through*- or *cross*- branch of the RDAC is activated. For example, a filter at $F_C = F_{CLK}/2$ has $Mix_{cont} = \cdots +1, -1, +1, -1, \ldots$, turning ON the *through*- and *cross*-

branches of the RDAC alternatively. A 1.2V supply drives these controls to maximize linearity with the provided DC bias of 0.6V.

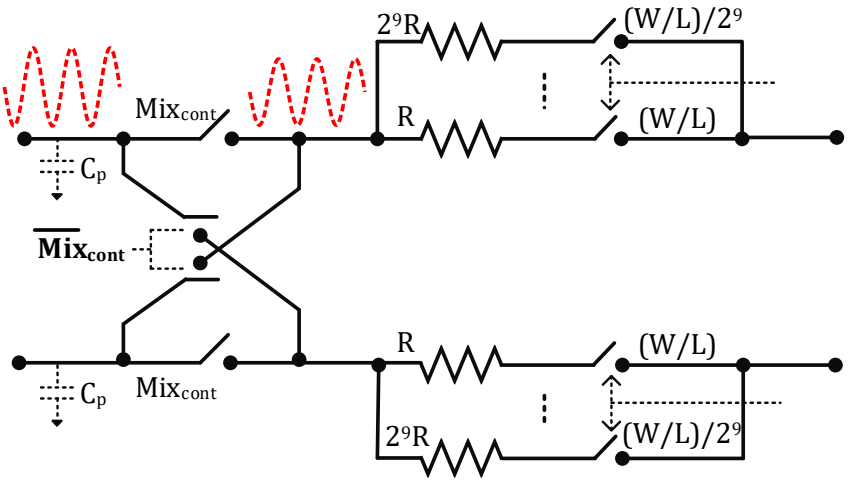


(a)

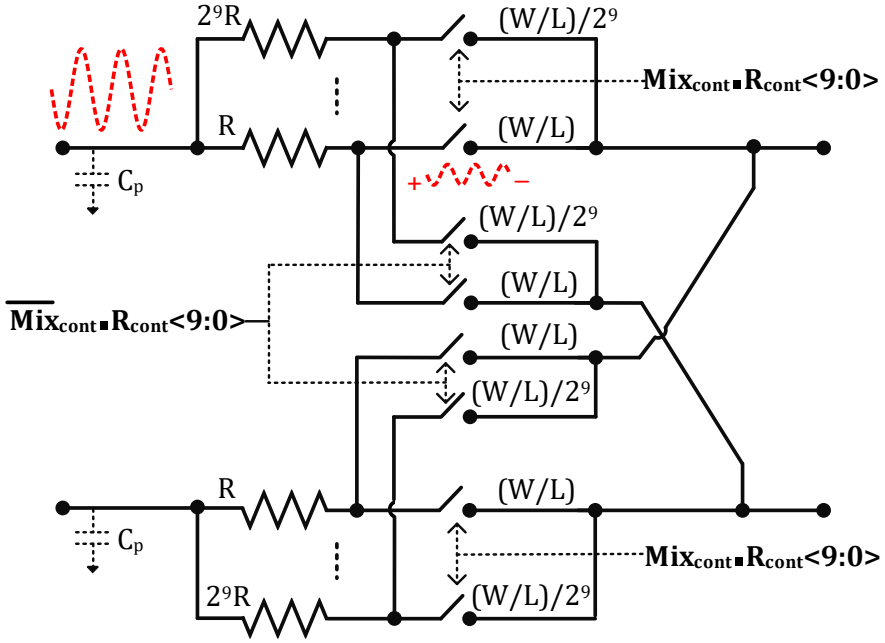


(b)

Fig. 3.2: (a) Naïve RDAC and mixer implementation [19]; (b) Superior RDAC with integrated mixer offering better linearity.

### *3.1.1.1 Circuit Parasitics*

Fig. 3.3 shows the single-ended RDAC circuit modified to explicitly show the switch and wire parasitics. There is also the parasitic capacitance to substrate associated with the *rppoly* resistors as well. The parasitics modify the equivalent LTI filter impulse response $g_{eq}(t)$ thereby degrading the filter response. A brief qualitative/intuitive overview of the circuit parasitics is provided here, with a detailed analysis deferred to Chapter 4.

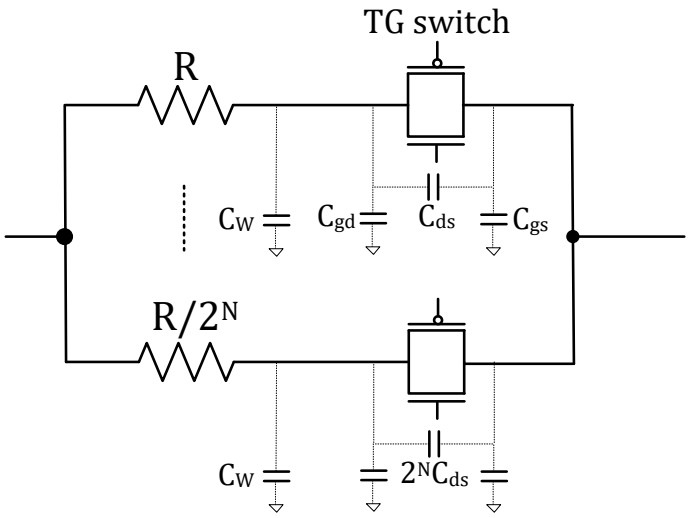


Fig. 3.3: Single-ended RDAC structure with parasitics.

*Parasitic Capacitance* $\boldsymbol{C_{ds}}$

In the naïve RDAC implementation [19], the achievable stop-band attenuation is significantly limited by the $C_{ds}$ capacitance of the transmission gate switches. Since the $R - C_{ds}$ cut-off frequency in the OFF-branches is significantly higher than the frequencies of interest, the RDAC structure in [19]Fig. 3.3 can be reduced to the one shown in Fig. 3.4(a), where the $C_{ds}$ of the OFF-portion provides a conductive path that could bypass the ON-portion, especially for small values of $n$.

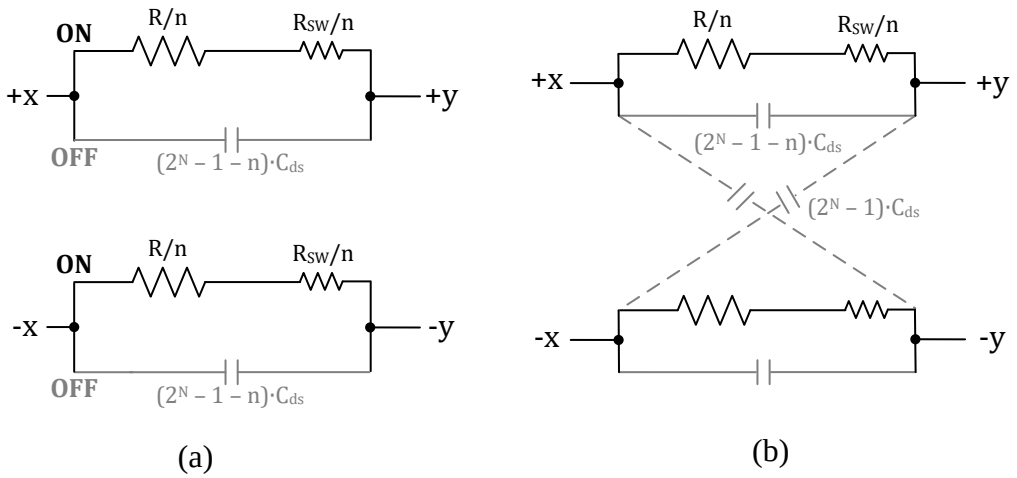


Fig. 3.4: (a) Equivalent differential structure with $C_{ds}$ capacitance for the naïve implementation of the RDAC [19]; (b) Equivalent schematic showing $C_{ds}$ capacitance for the improved RDAC with integrated mixer.

In the proposed RDAC with an integrated mixer, the effect of $C_{ds}$ is reduced as shown in Fig. 3.4(b). With the mixer incorporated in the RDAC switches, based on the resistor control code $n$ and the mixer control, either some of the *through*- branches and all the *cross*- branches of the RDAC are OFF or vice-versa. Then, as illustrated with the example in Fig. 3.4(b), the presence of additional $C_{ds}$ capacitances in the OFF *cross*- path help cancel some of the parasitic currents in the *through*- path. Now for smaller values of $n$, most of the parasitic currents cancel out. However, for large values of $n$, the net parasitic capacitance increases, but its parallel resistance decreases (unlike the structure in Fig. 3.4(a)), and hence the error introduced in the output voltage is reduced. As shown in Fig. 3.5, this helps reduce the impact of $C_{ds}$ on the filter response. Note, however, that $C_{ds}$ is not cancelled completely and hence there is still some worsening of the stop-band attenuation. When realizing band-pass filters, the change in the filter coefficients due to $C_{ds}$ also causes distortion in the envelope of the sinusoid, and hence adversely affects harmonic rejection as well.

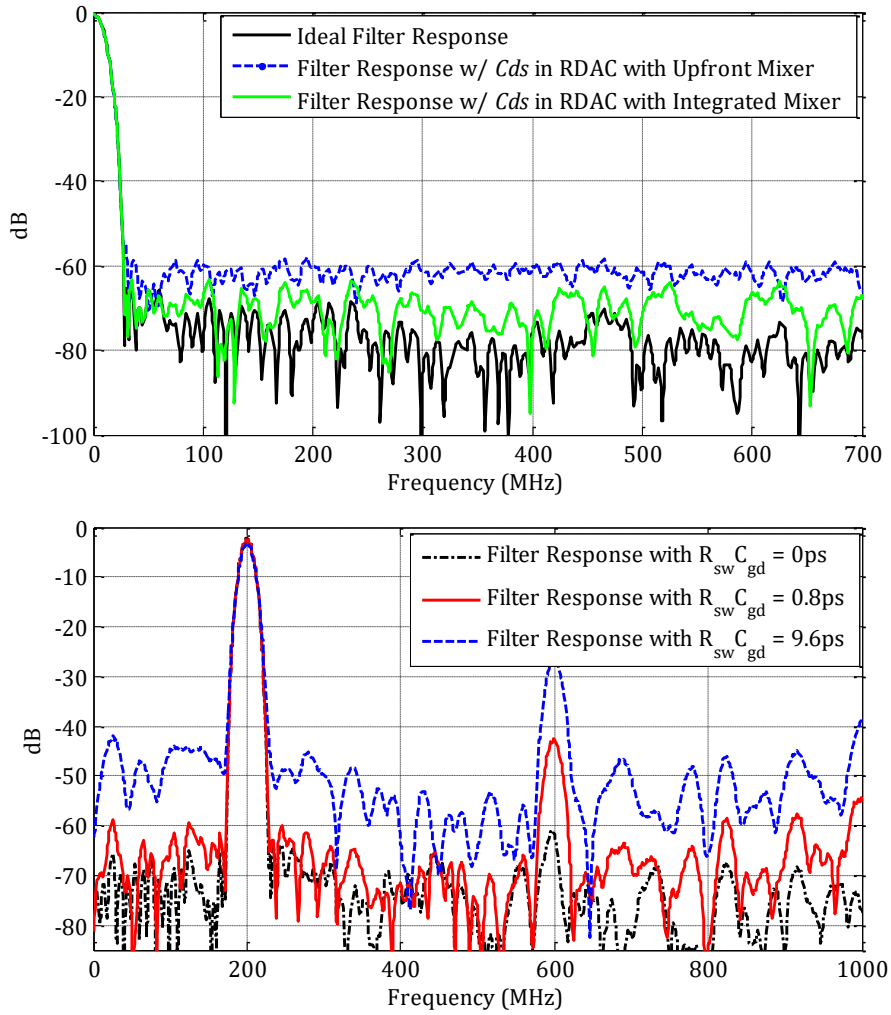


Fig. 3.5: Simulated effect of switch parasitics on filter suppression and harmonic rejection.

*Parasitic Capacitance* $\boldsymbol{C_{gs}}$, $\boldsymbol{C_W}$ *and* $\boldsymbol{C_{gd}}$

The $C_{gs}$ capacitance shown in Fig. 3.3 is always present in parallel with a much larger (~ 2-3 orders of magnitude) capacitor $C$ and hence does not have an impact on the filter response. $C_{gd}$ and $C_W$ (wire) capacitances on the other hand, manifest themselves in a rather complicated manner. Based on the resistor branches that turn ON from one instance to the next, variable amount of parasitic $C_{gd}$ and $C_W$ capacitances share charge with the load capacitor $C$. This time-varying charge

sharing alters the output voltage on the capacitor from its nominal value leading to degraded stop-band attenuation and harmonic rejection (HR).

HR relies on perfect sinusoidal mixing through the accurate realization and timing of the resistor value changes and the sign-switching events. This leads to harmonic rejection being much more sensitive to the presence of parasitic capacitances in the RDAC. The simulated effect of the $C_{gd}$ (and $C_W$) parasitic capacitances from the RDAC on HR and stop-band attenuation of the filters is shown in Fig. 3.5.

*Input capacitance* $\boldsymbol{C_P}$

The effect of the input parasitic capacitance, $C_P$, is best understood using the equivalent circuit shown in Fig. 3.6, obtained using source transformations. Firstly, the input voltage source is low-pass filtered which lowers the in-band gain of BPFs with high center frequencies, as demonstrated in Section 3.2. Secondly, the harmonic rejection is further degraded as it relies on a perfect input source with constant resistance to achieve accurate sinusoidal envelope tracking. Another intuitive perspective is that the upfront low-pass filter formed by the frequency dependent input source impedance affects the relative gain of the harmonic images being rejected by the FA circuit.

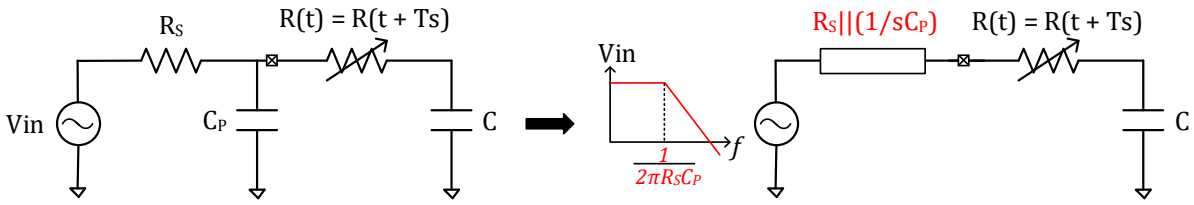


Fig. 3.6: Equivalent circuit in the presence of source resistance $R_S$ and input capacitance $C_P$.

#### *3.1.1.2 Circuit non-linearity*

The non-linearity of the filter is dominated by the switches used for the RDAC, more specifically by their non-linear resistance and capacitance. The use of transmission gates with a DC bias that is half the supply voltage, helps mitigate some of the non-linearity. As mentioned previously, the removal of explicit upfront mixer switches helps improve the linearity by $\sim 9$dB compared to our work in [19]. This is because, as shown in Fig. 3.2(b), the presence of series poly resistors with resistance that is 10x the ON-resistance of the switches, helps shield the RDAC switches from the large input signal swings.

### *3.1.2 Capacitor Banks*

The RDAC is followed by ping-pong output capacitor banks, $C$, allowing one capacitor's output to be read while the other is used in the filter. As noted in Chapter 2, Section 2.2, since the resulting IIR poles of the apparent filter response (denominator of $G_{eq}(e^{j\omega})$ in (2.8)) have minimal effect on the filter suppression, the ping-pong operation is used for ease of circuit implementation and chosen to demonstrate successful Filtering by Aliasing using simple sampling elements. The capacitor banks can be statically programmed to allow additional filter programmability. They are 5-bit binary-controlled MIM capacitors as shown in Fig. 3.7 and have a tuning range from 6.5pF to 201.5pF. A differential capacitor implementation was chosen to help with a 4X reduction in capacitance area compared to a pseudo-differential implementation (at the cost of no common-mode filtering). Binary weighted NMOS switches were used for the static control. The parasitics associated with these control switches of the capacitor banks have no effect on the filter response.

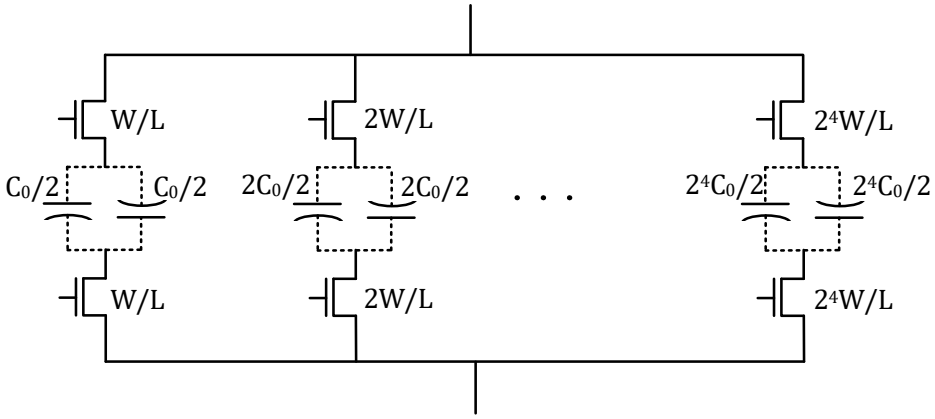


Fig. 3.7: 5-bit binary weighted capacitor banks.

### *3.1.3 Digital Control Unit and Clock Generation*

The resistor sequence bits, $R_{cont}\langle 9{:}\,0\rangle$, and the mixer-switching bit, $Mix_{cont}$, are periodic with $K = F_{CLK}/F_S$ and stored in register-based memory. They are generated offline using Matlab for the desired frequency bin and loaded on-chip. Since the sequence is read at the input rate ($F_{CLK} = KF_S$), the memory is split into equal halves corresponding to odd and even periods of $F_{CLK}$. A half-input-rate clock $F_{CLK/2}$, repeats a counter (counting from 1 to $K/2$) to provide addresses to sequentially read these memory registers. A 2:1 MUX running on $F_{CLK/2}$ toggles between the odd and even halves. This arrangement is chosen to allow for the high input rate operation with a minimal power cost. The 11 bits are then buffered to control the switches in the RDAC. The output sampling clock, $F_S$, is generated by dividing $F_{CLK}$ by $K$. Since the bandwidth of the designed filters is $F_S/2$, bandwidth programmability is enabled by changing the division ratio $K$. $F_{CLK}$ is itself generated from an off-chip differential clock signal buffered on chip. The digital and clock generation circuitry run on a 1V supply.

## 3.2 Measurement Results

The chip measurements were made using two setups, as shown in Fig. 3.8: 1) Using a $50\Omega$ source that is directly AC-coupled to scan a 1GHz spectrum and 2) using an upfront external demodulator (LTC5585) to extend the input scanning range. When using the external demodulator, two separate FA IC's were used for the I and Q paths. Since the output of the filters is a sampled and held signal at rate $F_S$, any input signal frequency greater than $F_S/2$ (around the carrier frequency of the filter) gets attenuated and aliases back into the 0 to $F_S/2$ band. Hence, unlike conventional continuous time systems, the filter responses are generated by providing tonal inputs and measuring the aliased signal acquired at baseband after sampling. For example, with $F_S = 10\text{MHz}$, for any center frequency, an input at 101MHz when passed through the LPTV RC circuit gets suppressed and aliases back to 1MHz, whereas an input at 106MHz would alias back to 4MHz. Off-chip buffers are used to drive these filtered outputs.

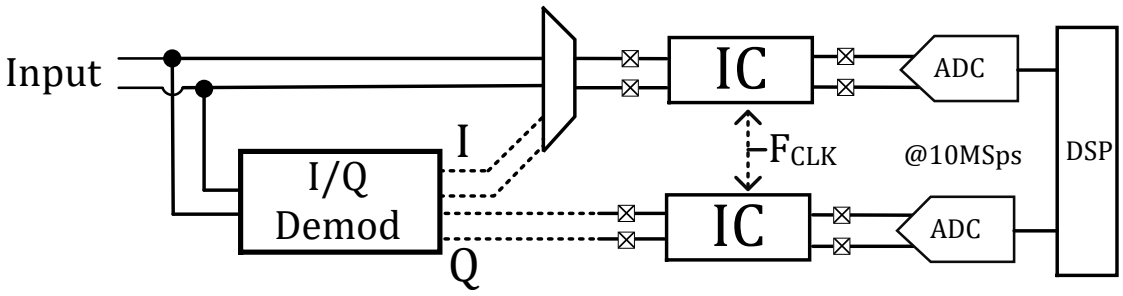


Fig. 3.8: System setup for testing.

On IC-startup, the RDAC is calibrated to a 9b level and the measured values are used to generate the filter responses using a resistance value vs resistor code look-up-table. The measured resistance values are shown in Fig. 3.9.

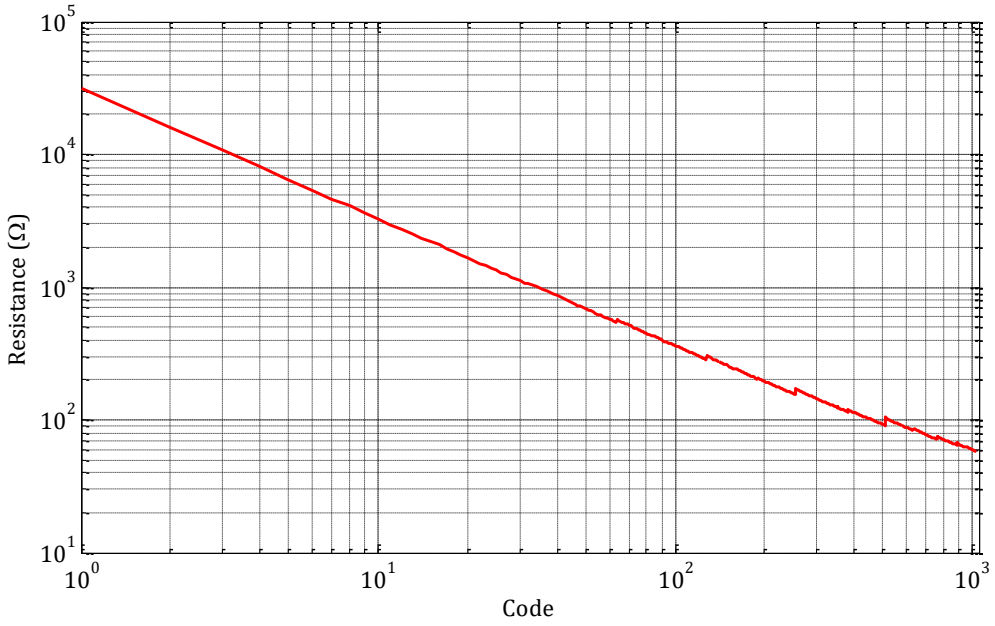


Fig. 3.9: Measured resistance vs resistor control code.

Programmability in the capacitor bank helps account for any global changes in these measured resistance values. Fig. 3.10 shows the normalized measured frequency response as the resistor sequence and mixer control, and hence the center frequency is varied to scan across the different frequency bins using the baseband setup. Similar responses were obtained with the demodulator setup as well. A representative measured filter response at 100MHz is shown in Fig. 3.11, indicating an analog resolution bandwidth (RBW) of 10MHz with an in-band ripple of ~1.5-2dB and a sharp transition bandwidth of 20MHz making it an equivalent $6^{th}$ order BPF. Resolution bandwidth could be programmed by changing the output sampling frequency and the filter capacitance.

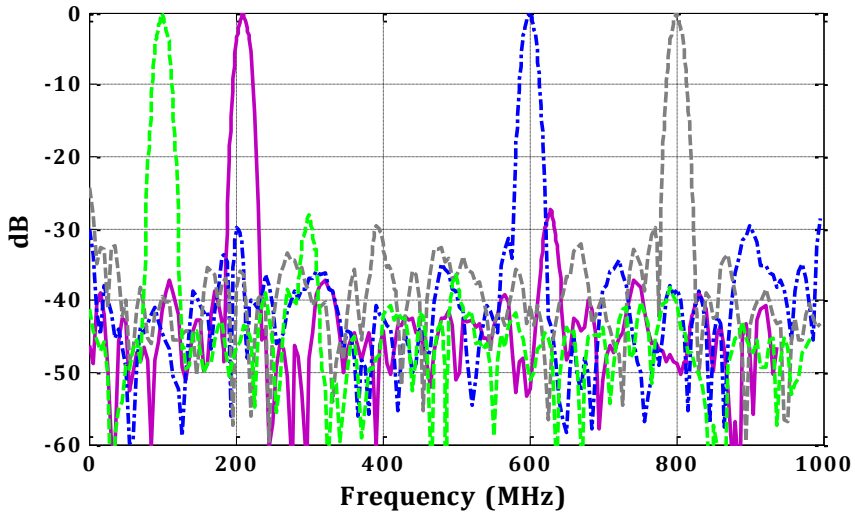


Fig. 3.10: Measured 10MHz filters at different center frequencies (normalized).

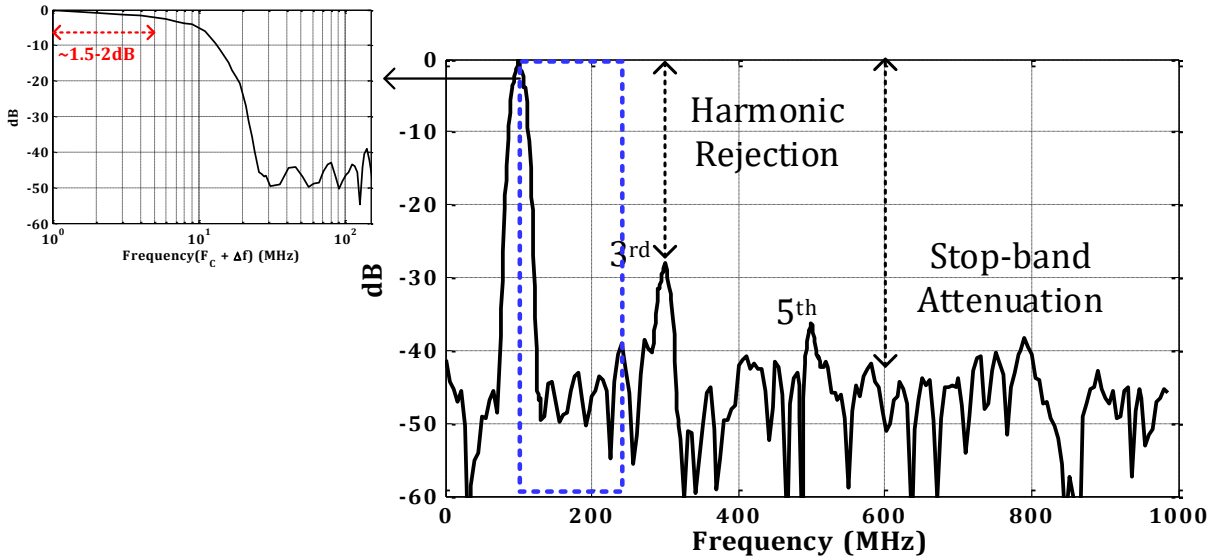


Fig. 3.11: Representative measured filter at 100MHz showing the harmonic response and stop-band attenuation.

Fig. 3.12 plots the worst case spurious images as the center frequency is varied. The measured stop-band attenuation is close to what was expected based on circuit parasitics. The harmonic

rejection, however, is lower than predicted due to an unexpected on-board capacitance, $C_P$ at the chip input in addition to the circuit parasitics. As shown in Section 3.1, this parasitic capacitance $C_P$ also causes a first-order gain roll-off as the filter center frequency, $F_C$ is swept across the 1GHz span. Furthermore, as mentioned previously, the inherent filter *sinc* shape also causes a systematic gain-variation of ~3dB across the 1GHz band. While the effect of the *sinc* shape is known at filter design time, $C_P$ is readily estimated and both effects are corrected for digitally. Fig. 3.13 shows the gain variation as the center frequency is varied. Note that the residual out-of-band signals (due to limited stop-band attenuation and/or harmonic rejection) can alias back in-band, leading to false detection.

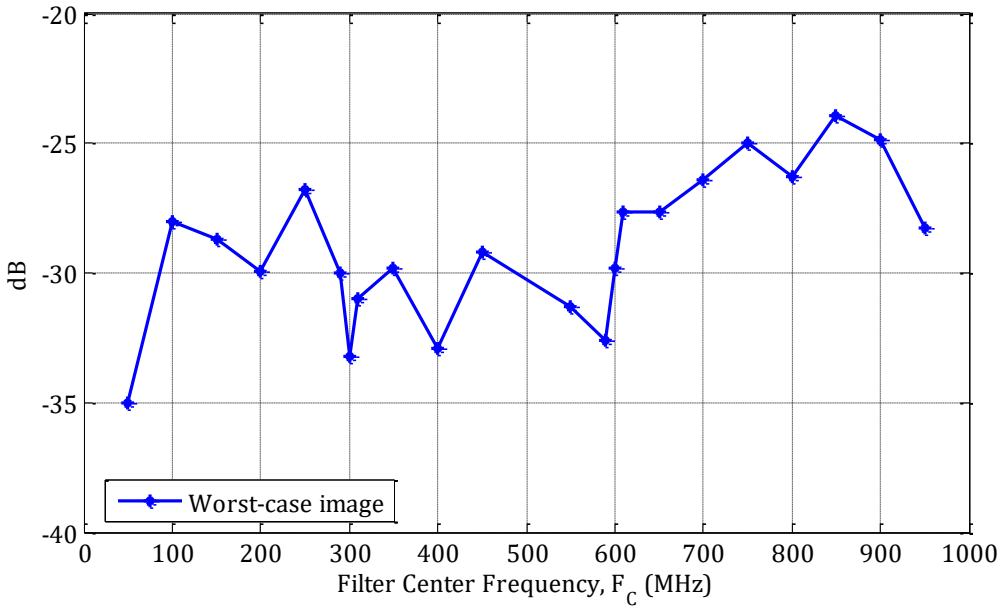


Fig. 3.12: Worst-case spurious image vs filter center frequency, $F_C$.

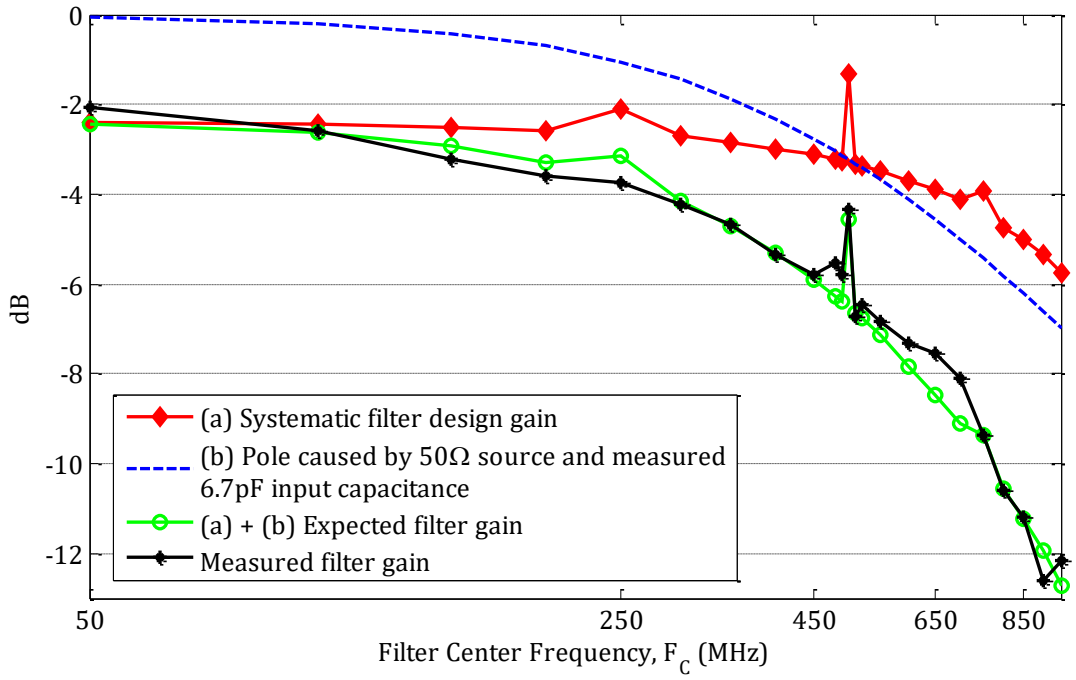


Fig. 3.13: Gain vs filter center frequency, $F_C$.

Fig. 3.14 and Fig. 3.15 show the out-of-band (OOB) IIP3 and sensitivity of the FA scanner respectively, both by itself and with the external demodulator. The results with the demodulator are for the upper-sideband with the demod-LO set at 1850MHz. Similar results were obtained for the lower-sideband as well. The FA scanner is highly linear with an OOB IIP3 of $> +31$dBm across the band. The Pin vs Pout curves for two example FA filters is also shown in the figure. The measured OOB IIP3 is at least +21dB higher than any other comparable spectrum scanner prior art; [25] presents a very linear filter as well, however it only performs low-pass filtering. In the presence of the external demodulator, the IIP3 worsens due to the limited linearity of the demodulator used. Based on the LTC5585 datasheet, the demodulator has a linearity of $\sim +$ 25dBm in the measured frequency range.

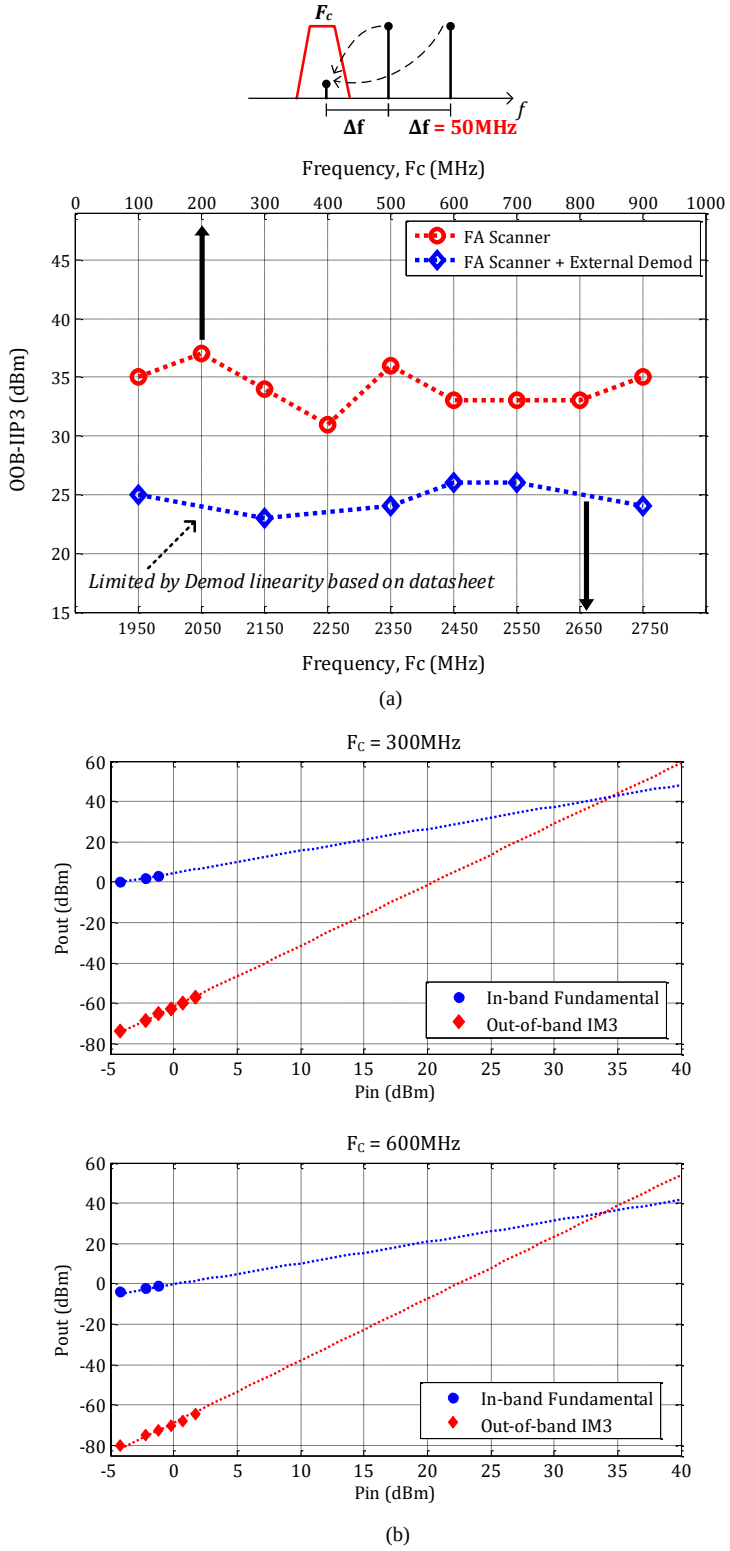


Fig. 3.14: (a) OOB-IIP3 vs center frequency of the FA Scanner with and without the external demodulator; (b) Pout vs Pin for two example filters.

The measured sensitivity (assuming a 0dB SNR) of the FA scanner by itself is better than $-142\text{dBm/Hz}$ and matches the expected value for the 32.5pF capacitance used with the output sampling rate of 10MHz. The upward trend in the scanner sensitivity as the filter center frequency is increased is related to the gain plot in Fig. 3.13. Due to the passive structure, the filter loss directly translates to reduced sensitivity.

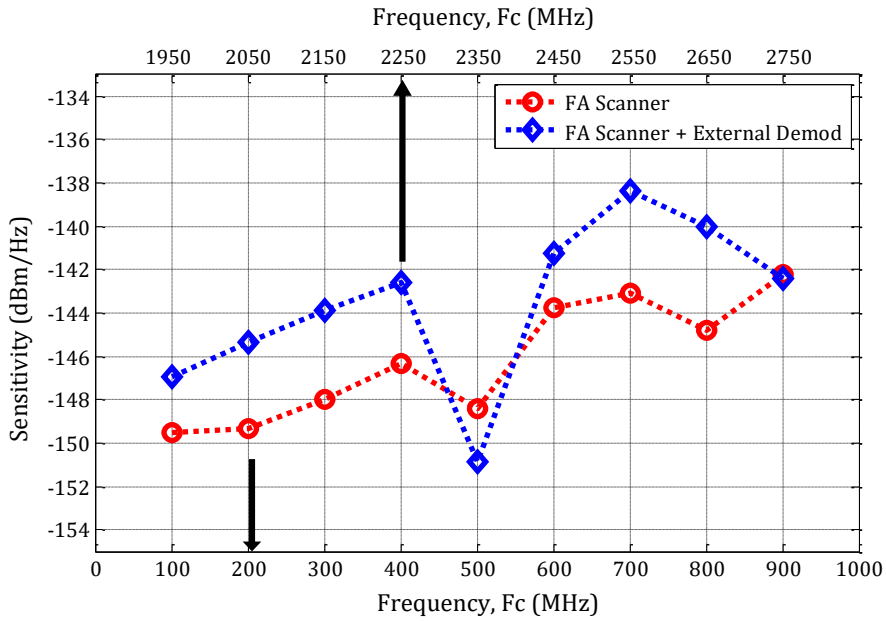


Fig. 3.15: Sensitivity vs center frequency of the FA Scanner with and without the external demodulator for 0dB SNR.

Power consumption is weakly dependent on $F_C$ with worst case observed for $F_C \sim F_{CLK}/2$: the switch drivers draw 2.1mA from 1.2V while the digital and clock generation blocks draw 4mA and 1.4mA respectively from 1V for a total power consumption of 8mW. For a 1MHz digital RBW (combined with a 20MHz analog RBW), the scan time for a serial scan of the 1GHz spectrum is 50us. Hence, this scanner is just a variant of the conventional scanners as far as the spectrum scan

time is concerned. The $S_{11}$ measurement for the scanner is shown in Fig. 3.16. It should be noted that at high frequencies the board capacitance $C_P$ mentioned previously affects the $S_{11}$ as well.

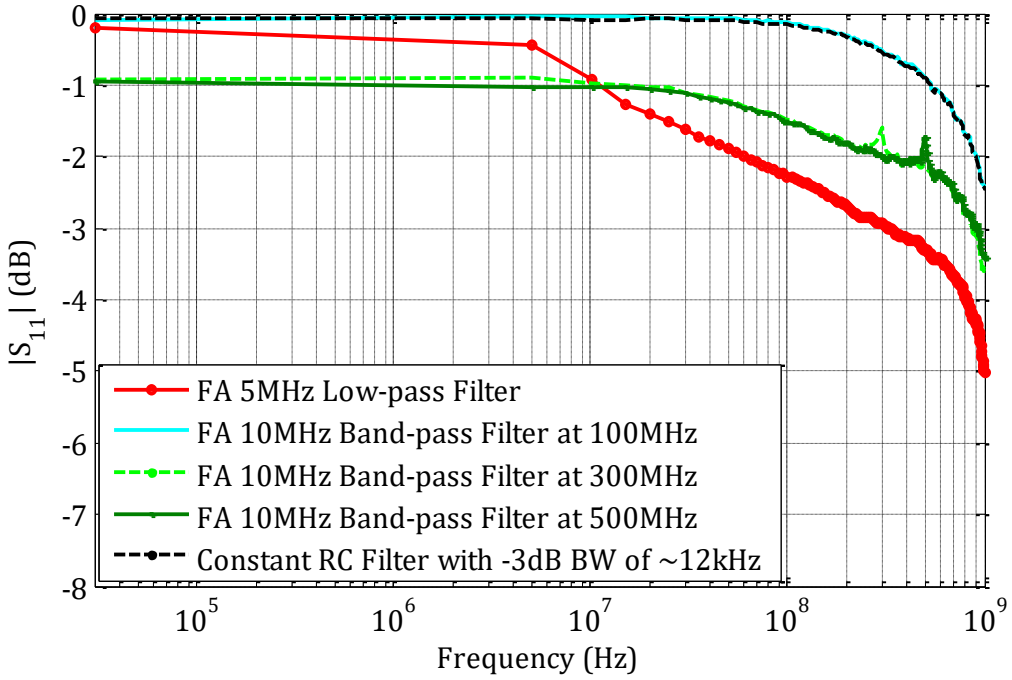


Fig. 3.16: Measured $|S_{11}|$ for the passive LPTV scanner.

Table 3.1 summaries the results for the FA scanner and compares it to other state-of-the-art designs. As can be seen, the LPTV RC scanner is a passive solution that provides the best linearity and lowest power compared to other designs. Although some solutions offer better sensitivity than this work, their spurious-free-dynamic range and power draw is significantly higher. The scan time for the proposed scanner is the same as for all the conventional scanners and as expected, higher than the CS-based scanner. Fig. 3.17 shows the chip micrograph. The active die area is $1.68\text{mm}^2$ and is dominated by the capacitor banks.

Table 3.1: Performance Summary and Comparison to Prior Art

| | This work | Goel [8] | Alink [9] | Ingels [12]-[13] | Yazicigil [15] |
|---|---|---|---|---|---|
| **Technology** | 65nm | 130nm | 65nm | 40nm | 65nm |
| **Architecture** | Filtering by Aliasing | Dual Up/Down Conversion | Cross-Correlation | Digital and Analog Multi-band Sensing | Compressive Sensing |
| **Circuit Implementation** | Passive | Active | Active | Active | Active |
| **Supply (V)** | 1.2(A), 1(D) | 1.8 | 1.2 | 1.1 | 1.1 |
| **Frequency Span (GHz)** | 0 - 1 | 0.1 - 6 | 0.3 - 1 | 0.5 – 2.5 | 2.7 - 3.7 |
| **Power (mW)** | < 8[a] | 227 | 36-61 | 33-99 | 81 |
| **OOB IIP3 (dBm)** | > +31 | +10 | +5[b] | -16 | N/R |
| **OOB IIP2 (dBm)** | +70 | +40 | N/R | +53 | N/R |
| **Sensitivity (dBm/Hz)[c]** | < -142 | -145 | -158[d] | N/R | -142[e] |
| **NF (dB)** | 26 | N/R | 10 | 7 | N/R |
| **SFDR in 1MHz RBW (dB)** | 75 | 63 | 69 | 61 | N/R |
| **Worst-case Spurious Image (dB)** | -24 | N/R | -27[f] | N/R | N/R |
| **Analog RBW (MHz)** | 10,20[g] | 0.4-11 | 20 | 0.2-20 | 10,20 |
| **Scan Time for 20MHz Analog RBW and 1GHz Span[h] (us)** | 50 | 50[i] | 50 | 50 | 4.4[j] |
| **Spectrum Occupancy Constraints** | None | None | None | None | Sparse (6%)[j] |
| **Active Die Area ($mm^2$)** | 1.68[k] | 14.43 | 0.15 | 5.2 | 1.96 |

[a] Excluding output buffer, and ADC; [b] IB/OOB not specified; [c] specified for 0dB SNR; [d] -172dBm/Hz using cross-correlation with maximum sensing time; [e] Measured using 80 samples with a $P_D = 90\%$ and $P_{FA} < 15\%$ ; [f] Obtained from [26] which expands on [9]; [g] Measured BWs, others achievable using programmable resistor waveforms; [h] 1MHz digital RBW; [i] 20MHz analog RBW not supported; [j] For a maximum of 3, 20MHz bins in 1GHz span; [k] 0.5$mm^2$ area is occupied by the extra capacitance added for debug

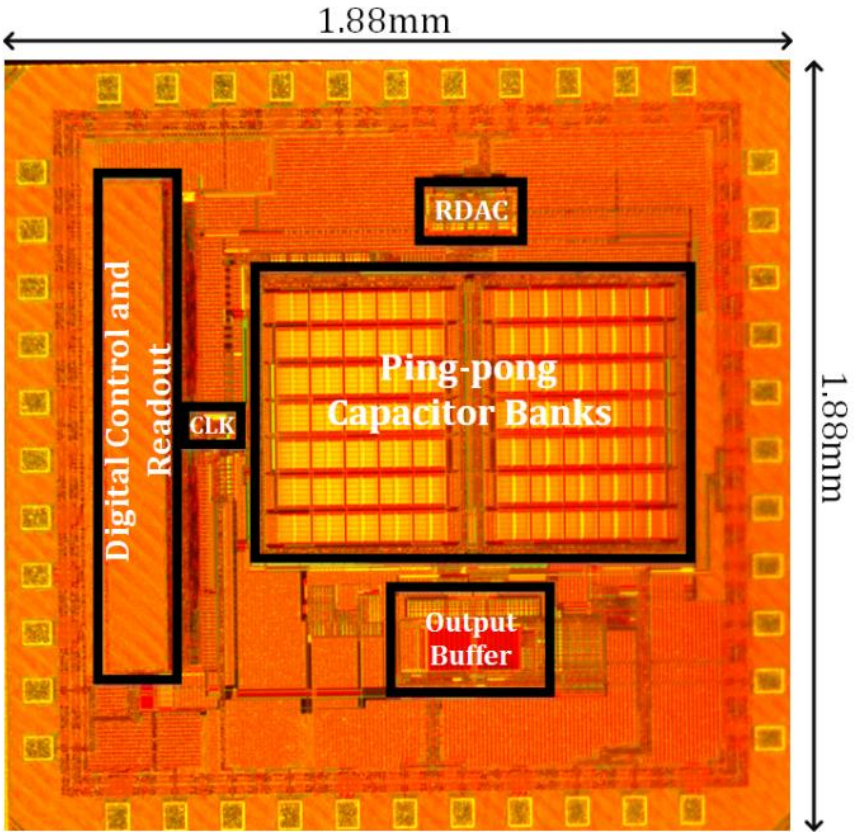


Fig. 3.17: Chip micrograph.

# Chapter 4

## Factors Affecting LPTV RC Filter Performance

In the previous chapters, a linear, periodically time-varying (LPTV) filter-based spectrum scanner based on the "Filtering by Aliasing" technique was demonstrated, that was programmable, had +21dBm better OOB-IIP3 than prior art and consumed very low power. However, as seen from the filter measurement results in Section 3.2, the stop-band attenuation and harmonic rejection were lower than what was predicted for the 10-bit RDAC. This was because the performance was mainly limited by the parasitic capacitances present in the resistor DAC (RDAC) used to implement the periodically time-varying resistance.

In this chapter, some of the limiting factors affecting the filter performance are discussed. A theoretical analysis of the various circuit parasitics associated with the RDAC and the upfront input capacitance that affect the LPTV RC filters is presented. While some effects are fundamentally limiting, others can be significantly improved with better circuit/board design, or need systematic circuit or signal processing solutions.

### 4.1 Non-ideal Integration

The passive implementation of the LPTV RC filter is essentially a lossy integrator, with the amount of charge deposited and discharged from the capacitor being determined by the periodically time-varying resistance. The exact expressions describing this behavior were shown in Section 2.2 where the exponential terms in (2.7) describe the charge lost from the output capacitor(and hence the lossy integration). Now, if we had an ideal integrator, the discrete-time

filter obtained using digital filter design techniques would result in a continuous-time filter with an exact zero-order hold on the filter taps in each time-step (of course with different expressions for $h_\eta$ as well). The amount of current integrated onto the capacitor in a given time-step would then only be a function of the input and the time-varying resistance in that time-step. However, due to the lossy integration, we do not have an exact zero-order hold on the filter taps in a given time-step, as was shown in Fig. 2.7 for an example low-pass filter and is shown in Fig. 4.1 for an example band-pass filter. The zero-order hold was used merely to approximately model the filter in the continuous-time domain. While this approximate zero-order hold resulting from the non-ideal integration in the time-step $T_{CLK}$ does not affect the overall envelope of the effective filter impulse response and hence the stop-band attenuation, it does impact the achievable harmonic rejection.

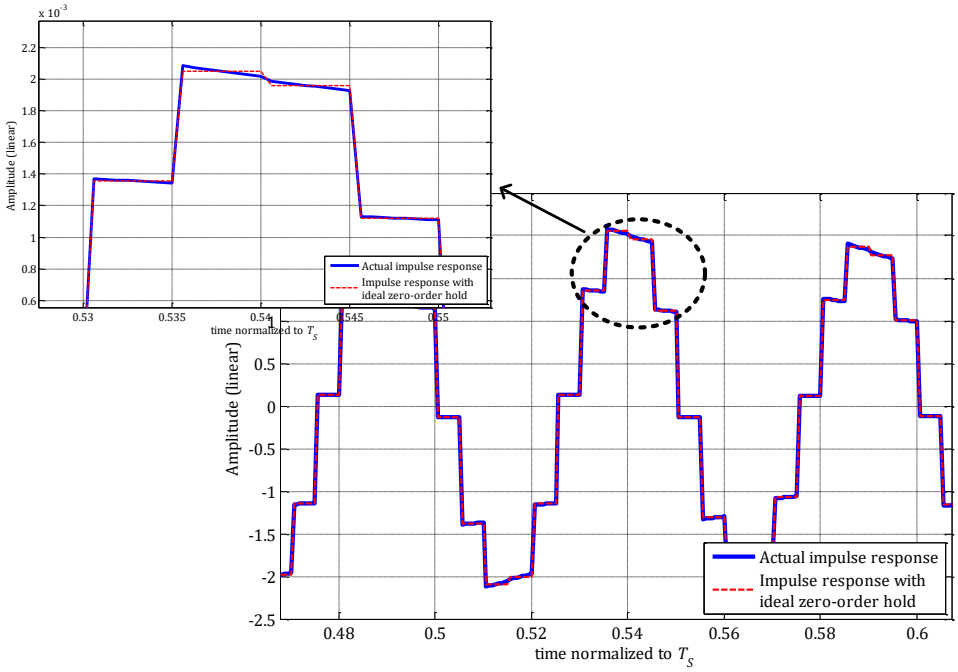


Fig. 4.1: Actual impulse response for an example band-pass filter showing the ideal zero-order hold as well.

The amount of deviation from an ideal zero-order hold is resistor dependent: larger resistor values cause smaller droop whereas smaller ones cause a larger droop. So for a bandpass impulse response, where the low-pass impulse response is multiplied by a sinusoid, while the values close to the zero-crossings of the sinusoid have a smaller/negligible error, the ones around the peak (corresponding to larger values of $\alpha_\eta$ and hence smaller values of R (2.7)) have larger errors. In addition, the error terms experience alternating phases in each half cycle of the LO, which leads to odd harmonics. Another intuitive way to think about this is in the frequency domain. Recall from Section 2.1.1, that harmonic rejection is achieved if the spectrum of the square wave, $p(t)$ convolved with the magnitude of the sinusoid perfectly cancels the harmonics. For this to happen, both the square-wave and the magnitude function need to be subjected to the same frequency operations. However, while the square-wave mixer, by design sees the ideal zero-order hold every $T_{CLK}$, the non-ideal integration means that the magnitude of the sinusoid can be broken into two parts: ideal zero-order hold plus an error term. This error term distorts the magnitude spectrum, leading to residual harmonics, even in the presence of infinite resistor quantization. This is shown in Fig. 4.2, where the filter response with an ideal zero-order hold on the magnitude of the impulse response (shown in Fig. 4.2) and the actual filter response with infinite resistance quantization is also shown.

To get a quantitative idea of this effect, we start with the understanding that an ideal zero-order hold would result in perfect harmonic suppression, i.e. the filter taps would be $\approx \alpha_\eta \prod_{k=0}^{\eta-1}(1-\alpha_k)$ (as shown in 2.7) in the entire $\eta T_{CLK}$ time-step. In reality however, there is a droop caused by the discharge through the resistor $R_\eta$, leading to a value of $\approx \alpha_\eta \prod_{k=0}^{\eta}(1-\alpha_k)$ at the end of the $\eta T_{CLK}$ time-step. Therefore, the maximum error in each time-step is given by

$$e_{ni,\eta} \cong \alpha_\eta \prod_{k=0}^{\eta-1}(1-\alpha_k) - \alpha_\eta \prod_{k=0}^{\eta}(1-\alpha_k) = \alpha_\eta \cdot \alpha_\eta \prod_{k=0}^{\eta-1}(1-\alpha_k) \quad (4.1)$$

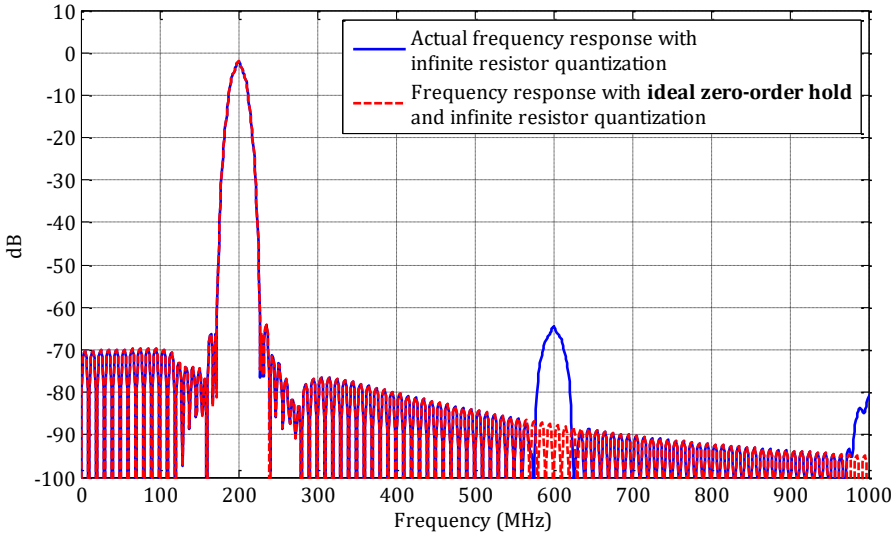


Fig. 4.2: Filter response highlighting the effect of non-ideal integration on harmonic rejection.

From (4.1) it is clear that the error is proportional to the tap-values as mentioned earlier. To get a bound on how this error affects harmonic rejection, we assume this error to be a square-wave with peak-to-peak value $\cong e^*_{ni,\eta}/2$, where $e^*_{ni,\eta}$ is the error caused by the minimum value of $R(t)$. Also, to account for the bell-shaped impulse response, we truncate the error terms near the tail-ends. Then the 3rd harmonic of this square-wave error provides an upper-bound estimate on the harmonic rejection. This is shown in Fig. 4.3 for an example filter with $min\big(R(t)\big)\, C = 9ns$ and $T_{CLK} = 500ps$. Two things must be noted here: 1) In reality, the error terms have a more sinusoidal shape since they arise from a sinusoid and hence the harmonic content is lower than that predicted by the above and 2) Due to the $(1-\alpha_k)$ terms in (4.1), the minimum value of $R(t)$ may not correspond to the maximum value of $e_{ni,\eta}$. Also, from (4.1) it can be seen that since the error is proportional to $\alpha_\eta$, for a similar $RC$ product, the error and hence the harmonic rejection worsens

with increasing $T_{CLK}$.

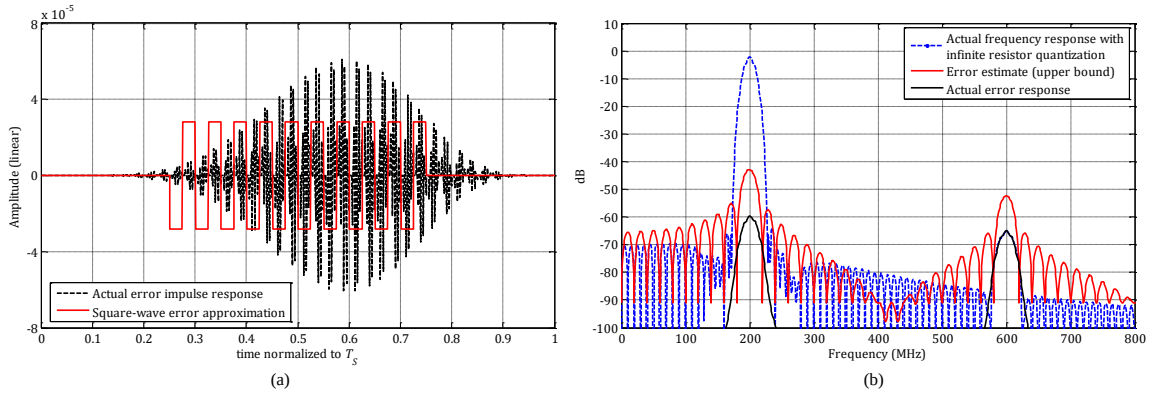


Fig. 4.3: (a) Actual error impulse response due to non-ideal integration and square-wave error estimate; (b) Frequency response of the actual error and the error estimate showing a coarse upper bound on harmonic rejection.

## 4.2 Circuit Parasitics

After describing the effect of the non-ideal *sinc filtering* on the filter response, we move onto the effect of circuit parasitics on the filter performance. To model their influence, we resort to the original, simple discrete-time domain model used in [27]. For sake of completeness, we first describe the ideal model below.

Fig. 4.4(a) shows the passive LPTV RC filter with an upfront mixer and the periodically time-varying resistance $R(t) = R(t + T_S)$. Momentarily ignoring the passive mixer and applying Kirchoff's Voltage Law (KVL) to this simple circuit, the input and output at any time is given by

$$x - y = (R(t) + R_S)C\frac{dy}{dt} \qquad (4.2)$$

For the purpose of filter design, we focus our attention to the practical case where the resistance

is varied in finite time-steps of $T_{CLK} = 1/F_{CLK}$, as shown in Fig. 4.4(b), such that $T_S/T_{CLK} = K \gg 1$ and $R_\eta = R(\eta T_{CLK}) = R_{\eta+K}$. Then, assuming the input is constant during this small time-step and the frequencies of interest are $< F_{CLK}/2$, it is easy to show that the differential equation in (4.1) can be directly discretized using an appropriate integration formula to give,

$$y_\eta = \alpha_\eta x_\eta + (1 - \alpha_\eta) y_{\eta-1} \quad (4.3)$$

where $\alpha_\eta = T_{CLK}/(T_{CLK} + (R_\eta + R_S)C)$, $x_\eta = x[\eta T_{CLK}]$ and $y_\eta = y[\eta T_{CLK}]$. Intuitively, the first term on the right-hand side in (4.3) represents the charge deposited by the input, whereas the second term signifies the discharge from the output. It turns out that in most practical scenarios to obtain useful filters $R_\eta C \gg T_{CLK}$.

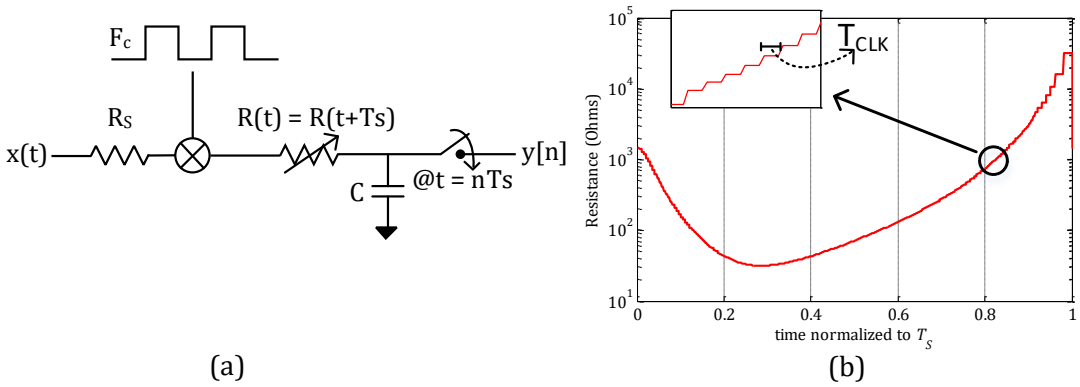


Fig. 4.4: (a) Passive LPTV RC filter; (b) Example resistor variation $R(t)$ in steps of $T_{CLK}$.

Now, by repeated application of this equation over successive time-steps, $T_{CLK}$, the transfer function from the input to the discrete-time, $K$ down-sampled output, $y[n]$ can be shown to be [27]

$$G_{eq}(e^{j\omega}) = \frac{\sum_{\eta=0}^{K-1}(\alpha_\eta)\left(\prod_{i=0}^{\eta-1}(1-\alpha_i)\right)e^{-j\omega\eta}}{1-\left(\prod_{\eta=0}^{K-1}(1-\alpha_\eta)\right)e^{-j\omega K}} \quad (4.4)$$

It is easy to see that for $R_\eta C \gg T_{CLK}$, (4.4) is the low-pass version of (2.8). In essence, the periodically time-varying resistance values are controlling the amount of input current, and hence charge that gets deposited on the capacitor in each time-step. Therefore, the LPTV RC filter can be viewed as the analog implementation of a digital filter given by (4.4). As mentioned earlier, traditional digital filter design techniques are used to design these filters and once the filter taps are known, the one-to-one mapping between $\alpha_\eta$ and $R_\eta$ is used to calculate the desired resistor variation for a given $T_{CLK}$ and $C$.

### *4.2.1 RDAC Imperfections*

At the heart of the LPTV RC filter lies the periodically time-varying resistor. The circuit implementations in [19] and the scanner use a 10-bit binary weighted RDAC, as shown again in Fig. 4.5(a) with *rppoly* resistors in series with transmission gate switches. The 10-bit DAC can ideally give a stop-band attenuation and harmonic rejection of ~60-65dB as was shown through the examples in Fig. 2.10. The measured response, however, is mainly limited by the circuit parasitics.

The RDAC structure with the dominant parasitic capacitances is shown in Fig. 4.5(b). $C_{gs}$ stems from the inherent capacitance of the transmission gates used for the switches and the wiring capacitance. Since it is always in parallel with the much larger (~2-3 orders of magnitude) filter capacitance $C$, it does not affect the filter performance. The other parasitic capacitances shown in Fig. 4.5(b) can affect the filter response significantly. Hence, in the following sections, their effect

on the filter response is investigated and some solutions to mitigate them are provided.

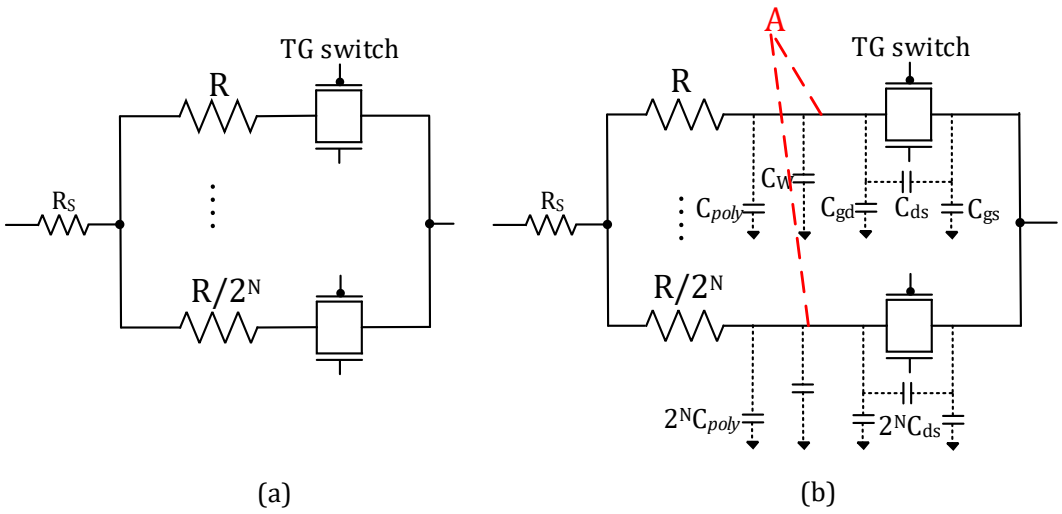


Fig. 4.5: (a) Single-ended, 10-bit binary-weighted RDAC, and (b) RDAC with dominant circuit parasitics.

#### *4.2.1.1 $C_{ds}$ Capacitance*

The $C_{ds}$ capacitance shown in Fig. 4.5(b) arises from the layout of the switches. It can be nominally reduced through good layout practices but cannot be completely eliminated. To understand how it affects the filter behavior, consider the circuit shown in Fig. 3.4(a) again, (shown in Fig. 4.6(a) for convenience): realizing a resistance of $R/n$, where $n$ is the digital control for the RDAC, has $(2^{10} - 1 - n) \cdot C_{ds}$ parasitic capacitances from the OFF branches in parallel with it (since the $RC_{ds}$ corner frequency in each branch is a constant and much larger than the frequencies of interest, we can ignore the series resistance in the OFF branches). By applying KVL to the half - circuit in Fig. 4.6(a), we have

$$x - y + \frac{R}{n} C_{ds} (2^{10} - 1 - n) \frac{d}{dt}(x - y) = \frac{R}{n} C \frac{dy}{dt}$$

$$\Rightarrow x - y + \frac{\boldsymbol{R}}{\boldsymbol{n}} \boldsymbol{C_{ds}}(\boldsymbol{2^{10} - 1 - n}) \frac{\boldsymbol{dx}}{\boldsymbol{dt}} \cong \frac{R}{n} C \frac{dy}{dt} \qquad (4.5)$$

since $C \gg C_{ds}(2^{10} - 1 - n)$. Compared to (4.2), the presence of $C_{ds}$ introduces a resistor control dependent error term which becomes worse as $n$ decreases, thus affecting the realization of larger values of R. Additionally, the $C_{ds}$ capacitance associated with the upfront mixer switches (not shown in Fig. 4.6(a)) will adversely affect the band-pass filter response as well. Fig. 4.6(b) shows the effect of $C_{ds}$ on an example band-pass filter at 700MHz.

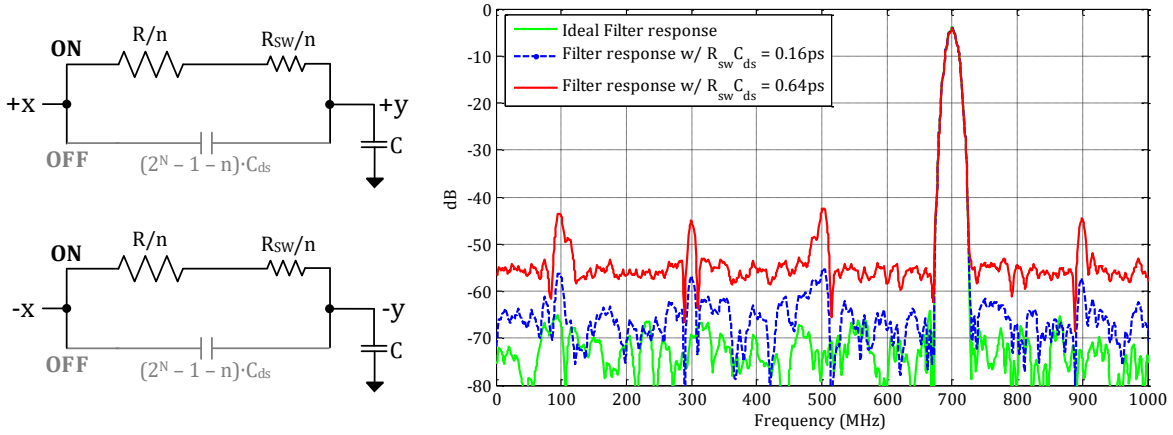


(a) (b)

Fig. 4.6: (a) Differential RDAC in the presence of $C_{ds}$; (b) Effect of $C_{ds}$ on the filter response shown for an example BPF at 700MHz.

As mentioned in Section 3.1, a circuit solution for the above is implemented in the scanner [28] by incorporating the mixer in the RDAC itself. To understand how this helps, as an example, consider the low-pass version, where only the *through*- branch of the RDAC with the integrated mixer is activated, resulting in the RDAC structure shown in Fig. 4.7(a). Applying KVL to this new structure, we have,

$$x - y + RC_{ds}\frac{dx}{dt} \cong \frac{RC}{n}\frac{dy}{dt}\ ;\ since\ C \gg 2^{11}C_{ds} \qquad (4.6)$$

We can see from (4.6), that $C_{ds}$ while present, is independent of the resistor control. As shown in Fig. 4.7(b), this helps reduce the impact of $C_{ds}$ on the filter response. The simulated filter has a unit switch $R_{on} = 3.2k\Omega$ and $C_{ds} = 0.2fF$. Note, however, that $C_{ds}$ is not cancelled completely and hence there is still some residual worsening from the ideal filter response. An intuitive understanding of why this helps was described in Section 3.1.1.

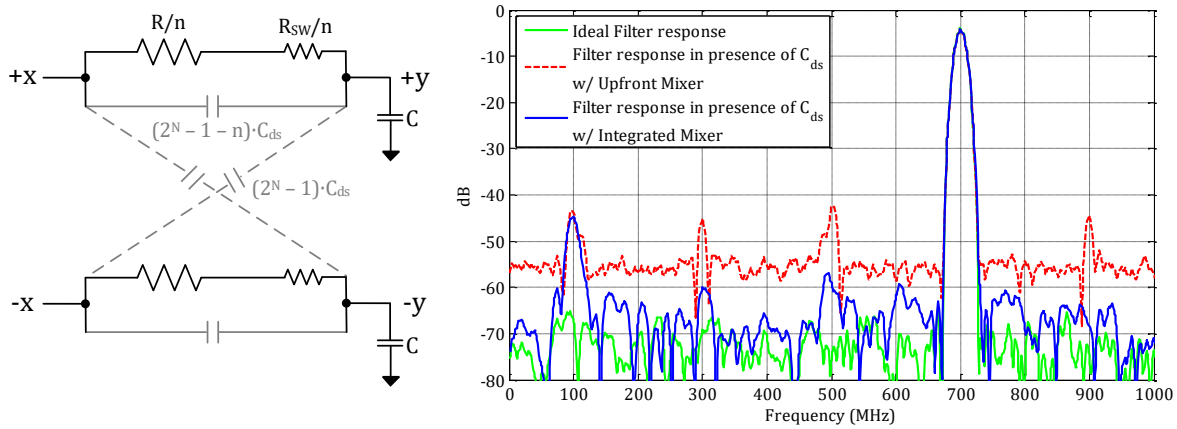


(a) (b)

Fig. 4.7: (a) Differential RDAC with integrated mixer; (b) Effect of $C_{ds}$ on filter response with and without the integrated mixer for an example simulated band-pass filter at 700MHz.

### *4.2.1.2 $C_1\left(C_{gd} + C_W + C_{poly}\right)$ Capacitance*

$C_1$ represents all the parasitic capacitances that are present at node A in Fig. 4.5(b). It stems from the capacitance to substrate associated with the *poly* resistors, and the wire and switch capacitances. For a binary weighted RDAC while the capacitances associated with the poly resistors and the switches will scale in a binary manner, the wire capacitances may not. Hence,

special care must be taken to ensure that the RDAC is truly binary i.e. the resistances and parasitic capacitances both vary in a binary fashion. While not required, for the sake of simplicity, in the analysis presented here $C_1$ is assumed to vary in a binary fashion across the RDAC.

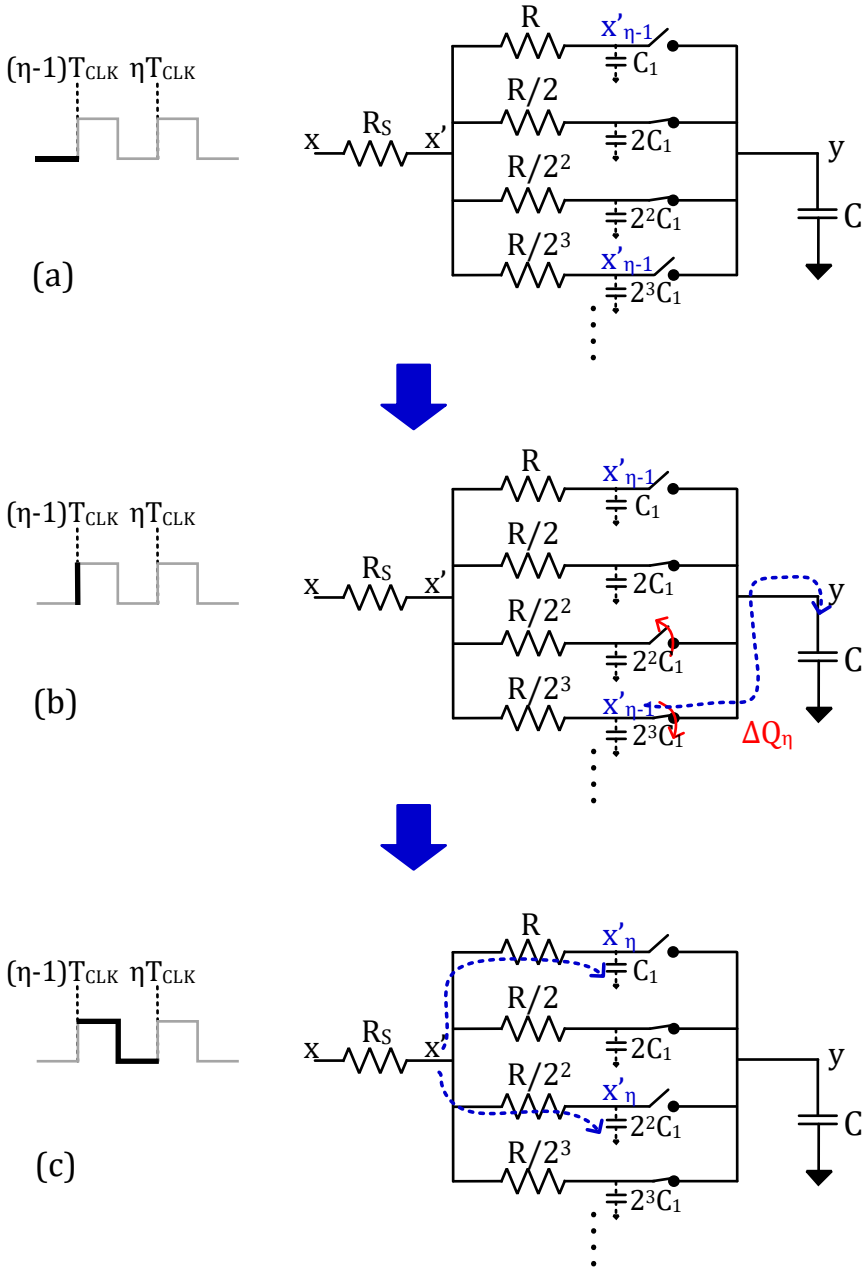


Fig. 4.8: Example RDAC operations depicting the effect of $C_1$ in a low-pass configuration.

The effect of $C_1$ on the filter behavior is periodically time-varying and manifests itself in a rather complicated manner. To help illustrate its effect, consider the example shown in Fig. 4.8 where only a part of the RDAC is shown for simplicity. For the example shown in the figure, the RDAC controls are set such that the resistance value in the $(\eta-1)T_{CLK}$ time-step, $R_{\eta-1}$, is equal to $R/6$. During this time-step, the ON branches continue with their normal $RC$ operation, whereas the OFF branches charge up to the $x'_{\eta-1}$[6] value as shown in Fig. 4.8(a). At the $(\eta-1)T_{CLK}$ edge, as the RDAC value changes to a new resistance value, $R/10$ in the example presented, the 4th resistor branch turns ON. As shown in Fig. 4.8(b), the parasitic capacitance in this branch will now share some charge $\Delta Q_\eta$ with the filter capacitor, $C$. It is important to note that only the parasitic capacitances in the branches that turn ON (i.e. go from being open to close) from one time-step to the next contribute to the charge shared with the main filter capacitor. Hence, the amount of charge transferred at each clock edge is a function of *both*, $R_\eta$ and $R_{\eta-1}$. Subsequently, the filter operates with the new resistor value and the OFF branches draw some current and charge up to the $x'_\eta$ value at the end of the $\eta T_{CLK}$ time-step.

The complete mathematical model describing the effect of $C_1$ on the filter transfer function is derived in Chapter Appendix 4.3.1, where it is shown that the presence of $C_1$ modifies (4.3) to

$$y_\eta \cong \alpha'_\eta\gamma_\eta \cdot x_\eta + \alpha'_\eta\gamma_{2,\eta}g_{\eta-1} \cdot x_{\eta-1} +$$

$$\left(1-\alpha'_\eta\right)\cdot\left(\beta_\eta g_{\eta-1}\cdot x_{\eta-1} + (1-\beta_\eta)\cdot y_{\eta-1}\right) \qquad (4.7)$$

[6] It is assumed that $RC_1 \ll T_{CLK}$ in each branch and hence this assumption is valid for input frequencies of interest ($< F_{CLK}/2$).

$where$

$\alpha'_\eta = T_{CLK}/(T_{CLK} + (R_\eta + R_S||R_{eq,\eta})C)$,

$R_{eq,\eta} = R_{eq1,\eta}||R_{eq2,\eta}$,

$\gamma_\eta = R_{eq,\eta}/(R_{eq,\eta} + R_S)$,

$g_\eta = \gamma_\eta \cdot R_\eta/(R_\eta + R_S||R_{eq,\eta})\ and$,

$\gamma_{2,\eta} = (R_S||R_{eq,\eta})/R_{eq1,\eta}$.

$R_{eq1,\eta}$ and $R_{eq2,\eta}$ are switched-capacitor resistances that are described in more detail in the Appendix. Equation (4.7) while complicated can be intuitively explained using superposition. Fig. 4.9(a) models the equivalent circuit in each time-step in the presence of $C_1$. The first two terms on the right-hand side (RHS) describe the charge path from the input, whereas the last two terms signify the discharge from the output filter capacitor, $C$. The Thevenin equivalent "looking into" the input, $x_\eta$ for the circuit in Fig. 4.9(a) is shown in Fig. 4.9(b): the input is scaled by the factor $\gamma_\eta$ and the resistance is modified to $(R_\eta + R_S||R_{eq,\eta})$, leading to the first term in the RHS of (4.7). Using the same equivalent circuit and ignoring the second-order terms, it can be easily shown that $x'_{\eta-1} \cong g_{\eta-1} \cdot x_{\eta-1}$.

The equivalent circuit from $x'_{\eta-1}$ can be similarly found and is shown in Fig. 4.9(c), leading to the second term in the RHS of (4.7). The last two terms signify the discharge from the output filter capacitor, $C$ for the equivalent circuit shown in Fig. 4.9(d). Just like in the ideal case, (4.7) can be repeatedly applied to get the new filter taps in the presence of parasitic $C_1$. For simplicity,

the model and equation shown here is for the low-pass filter which can be easily extended to the band-pass version by including the sign switching provided by the mixer switches.

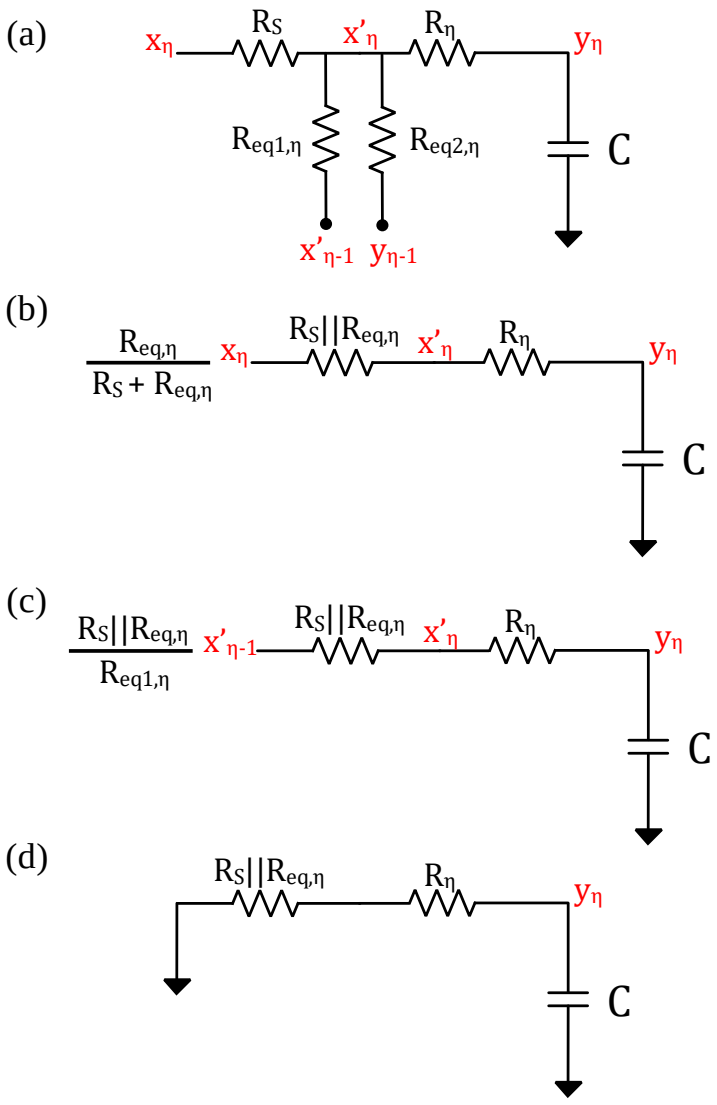


Fig. 4.9: (a) Equivalent circuit in each time-step in the presence of parasitic capacitance $C_1$; (b) Thevenin equivalent circuit from the input $x_\eta$ ; (c) Thevenin equivalent circuit from $x'_{\eta-1}$; (d) Thevenin equivalent circuit for the output voltage discharge.

As can be seen from above, the presence of $C_1$ affects all the filter coefficients in a recursive, non-linear (with respect to the filter tap value) manner, altering the amount of charge deposited/lost from the main filter capacitor, $C$ in each time-step from its optimal value described in (4.3). As an example, the ideal filter taps for a low-pass filter and the error terms due to the presence of $C_1$ are shown in Fig. 4.10.

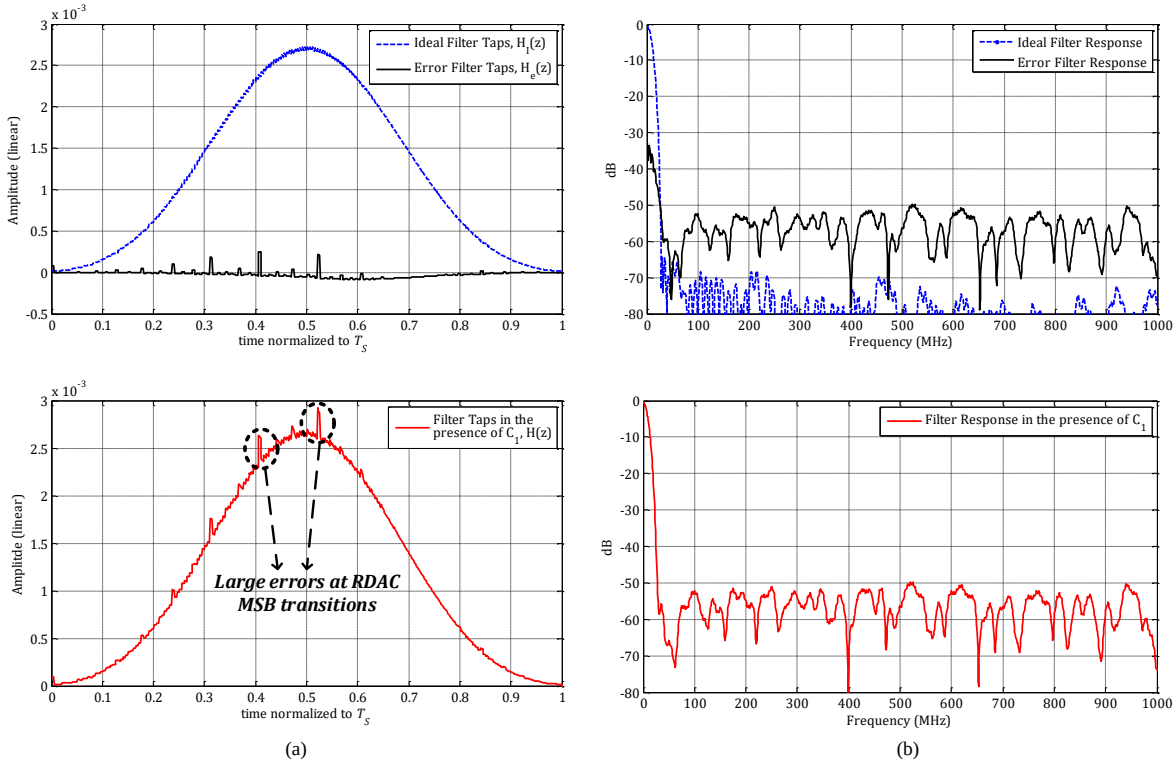


Fig. 4.10: (a) (Top) Ideal ($H_I(z)$) and error ($H_e(z)$) filter taps (impulse response) for an example low-pass filter, (Bottom) Filter taps (impulse response) in the presence of $C_1$, (b) (Top) Ideal and error frequency response; (Bottom) Frequency response in the presence of $C_1$.

The filter response in the presence of $C_1$, $H(z)$ can be broken down into two parts: $H_I(z)$, the ideal response, and $H_e(z)$, the error response. As can be seen from Fig. 4.10, $H_e(z)$ has no straightforward relationship with $H_I(z)$. Also, as one would expect, large errors are made as the

most significant bits transition in the RDAC, leading to jumps in the filter impulse response which is shown in the figure as well. For instance, the large error around $0.4T_S$ arises as the RDAC control goes through an MSB change. This is shown in Fig. 4.11, where bit 8 of the RDAC transitions. Since the stop-band attenuation is a function of the shape of the impulse response, the presence of these abrupt jumps in the response leads to worsening of the filter attenuation.

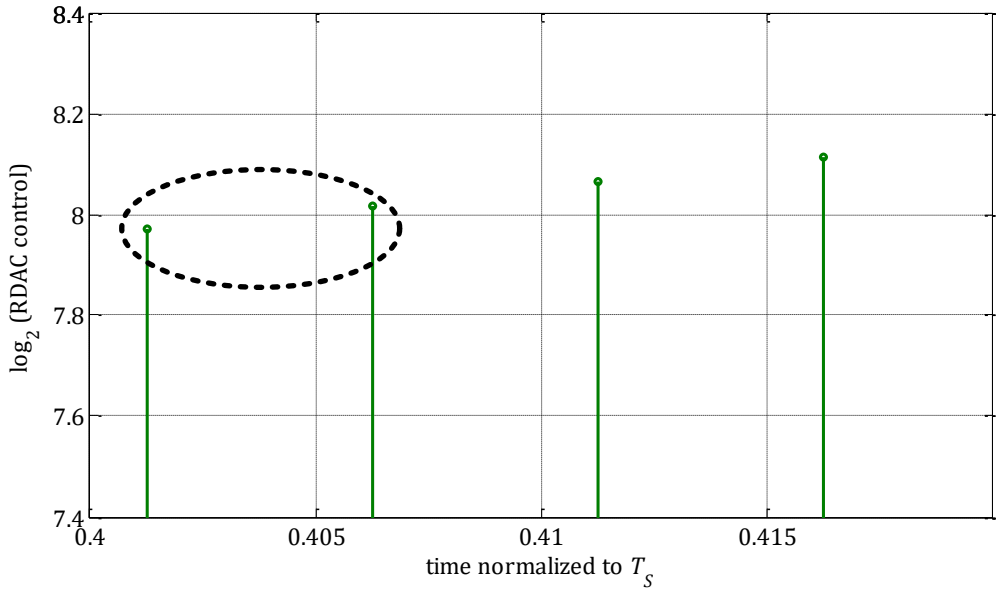


Fig. 4.11: RDAC control vs time showing MSB transitions for the example LPF in Fig. 4.10.

Fig. 4.12 shows the effect of $C_1$ on the filter response based on the mathematical model derived in Appendix 4.3.1 and compares it with the Spectre PSS-PXF simulations for an example low-pass filter and two band-pass filters. The RDAC values used for these plots are: $R = 32k\Omega, C_1 = 2.5\ fF$ with $T_{CLK} = 500ps$. The filter response with an ideal 10-bit RDAC is also shown. We make the following observations from these plots:

1) The presence of $C_1$ significantly worsens both the stop-band attenuation and harmonic rejection. This is because both the envelope of the impulse response and the magnitude of the

sinusoid are affected.

2) The model compares very well with the simulated results using Spectre, for both low-pass and band-pass filters.

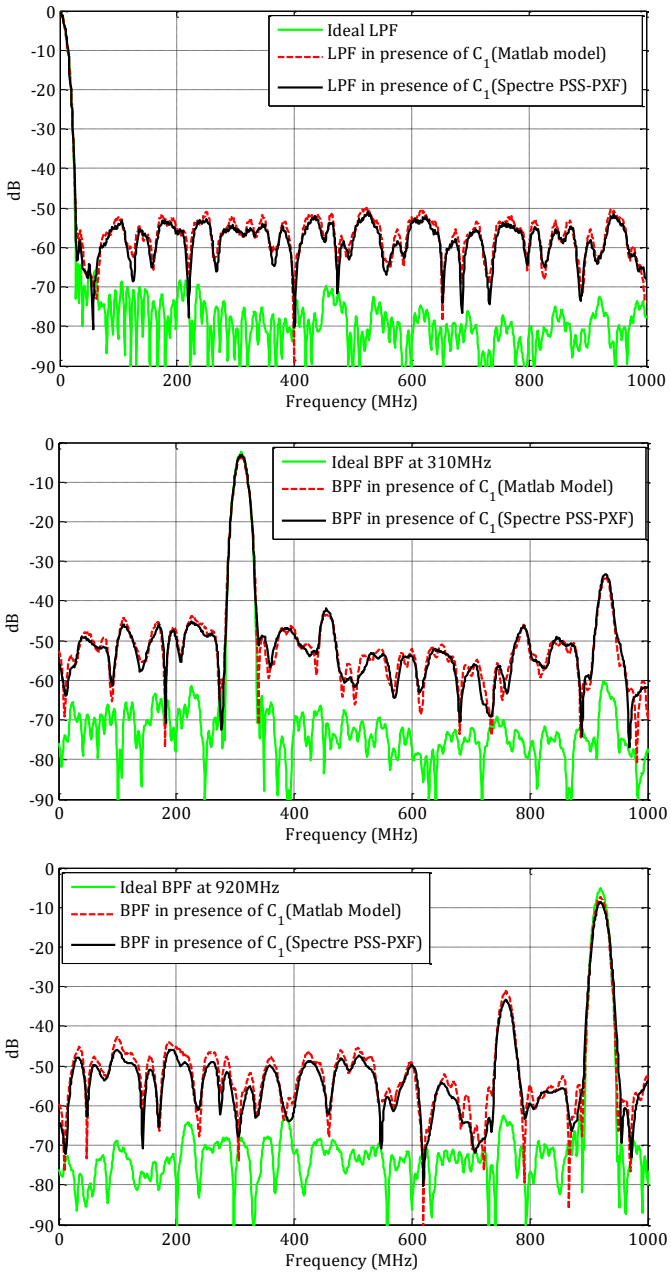


Fig. 4.12: Theoretical (Matlab) Model vs Simulation results in the presence of $C_1$ for an example low-pass filter and two band-pass filters at 310MHz and 920MHz.

### *4.2.1 Source Capacitance*

Fig. 4.13 shows the LPTV RC filter with the source resistance $R_S$, together with the parasitic source capacitance, $C_P$. The $C_P$ capacitance can result from the printed circuit board (PCB) traces, the package and bond-wire capacitance and if not considered carefully, can be large for poor PCB design and package choices.

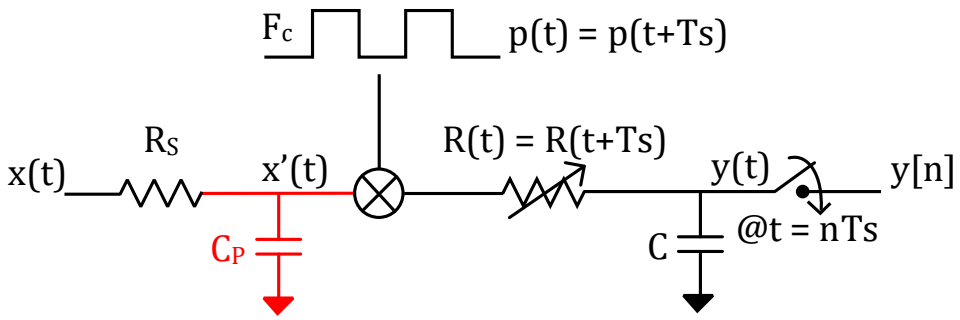


Fig. 4.13: Passive LPTV RC filter with upfront source parasitic capacitance, $C_P$.

An intuitive explanation regarding the effect of $C_P$ was given in Section 3.1.1. However, for a complete quantitative analysis, Laplace transforms used earlier cannot be used for this time-varying circuit. Hence, we again resort to the discrete-time model used in the earlier sections. Applying KVL to the second-order circuit shown in Fig. 4.13, we have

$$x - x' = R_S C_P \frac{dx'}{dt} + pR_S C \frac{dy}{dt}$$

$$x' - py = pR(t)C\frac{dy}{dt} \qquad (4.8)$$

Using a discrete-time approximation for (4.8), it can be easily shown that the output at each time step, $y_\eta$ is now given by

$$y_\eta = p_\eta \frac{T_{CLK}}{T_{CLK}+\tau_\eta} \boldsymbol{x_\eta} + \frac{\tau'_\eta}{T_{CLK}+\tau_\eta} \boldsymbol{y_{\eta-1}} + p_\eta p_{\eta-1} \frac{R_S C_P R_{\eta-1} C}{T_{CLK}} \frac{1}{T_{CLK}+\tau_\eta} \boldsymbol{y_{\eta-2}} \quad (4.9)$$

$$\tau_\eta = (R_\eta + R_S)C + \frac{R_S C_P R_\eta C}{T_{CLK}} + R_S C_P;$$

$$\tau'_\eta = (R_\eta + R_S)C + \frac{R_S C_P R_\eta C}{T_{CLK}} + R_S C_P p_\eta p_{\eta-1}\left(1 + \frac{R_{\eta-1} C}{T_{CLK}}\right)$$

The presence of two capacitances with independent voltages right away suggests that we now have a second-order circuit at hand and hence a second-order term in (4.9). The expression while complicated helps construct the effective impulse response of the filter in the presence of $C_P$ and hence determine it's impact on the filter response. Fig. 4.14 shows the effective impulse response of the LPTV RC filter with the upfront capacitance, $C_P$.

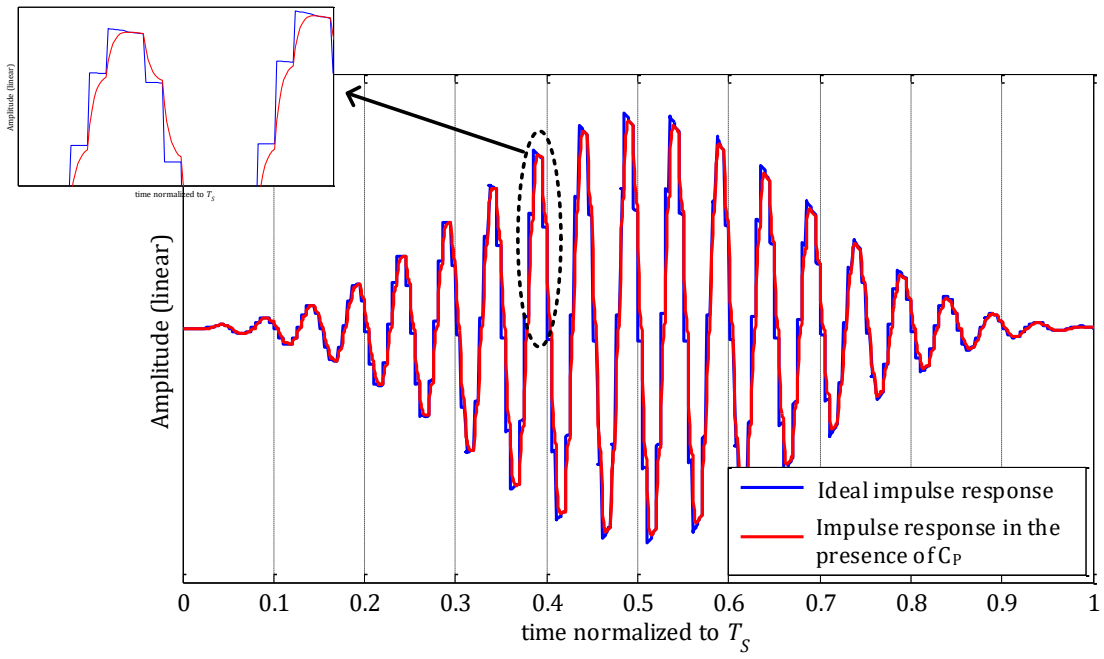


Fig. 4.14: Impulse response for an example BPF at 200MHz with and without the upfront parasitic capacitance, $C_P$ (6pF used here).

Two things can be noted here:

1) The envelope of the impulse response is preserved which implies the stop-band attenuation will be unaffected.

2) The sinusoidal variation, however, is affected. As was noted in Section 2.1.1, harmonic rejection is achieved by realizing the magnitude of the sinusoid using the resistor variation and the *sign* of the sinusoid using the passive mixer. Perfect rejection is obtained when the convolution of the magnitude spectrum with the square-wave mixer waveform spectrum is such that it completely cancels the harmonic. However, with the magnitude function now distorted (while the square-wave switching is unaltered), harmonic rejection is worsened.

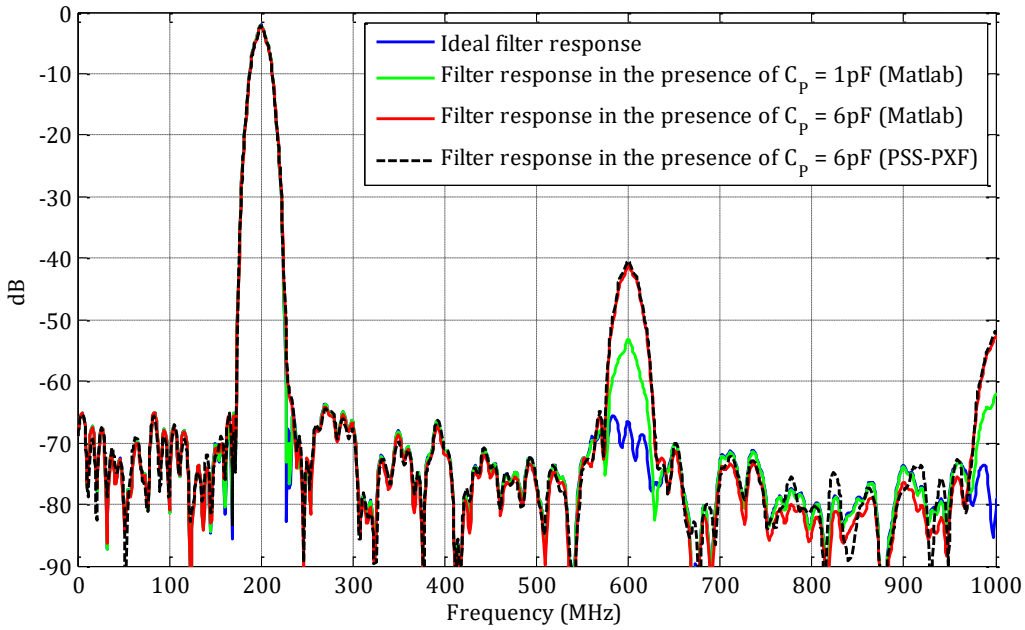


Fig. 4.15: Frequency response for an example BPF at 200MHz in the presence of $C_P$.

The frequency response of the filter in the presence of $C_P$ is shown in Fig. 4.15 and was again verified using the Spectre PSS-PXF simulations in Cadence. As was expected from the filter impulse response, the stop-band attenuation is preserved while harmonic rejection is worsened. In practice, the upfront capacitance can be significantly reduced (~1 – 2pF) with good PCB design and proper package selection. In addition, the presence of the bond-wire inductance helps offset some of the capacitance.

## 4.3 Chapter Appendix

### *4.3.1 LPTV RC Filter in the presence of $C_1$ capacitance in the RDAC*

To mathematically model the effect of $C_1$ on the filter behavior, we start with the example shown in Fig. 4.8. As mentioned previously, if $RC_1 \ll T_{CLK}$, the parasitic capacitors will track the voltage $x'$ in the resistor branches that are OFF. Hence, the voltage on the parasitic capacitor in the 4th branch at the end of the $(\eta - 1)T_{CLK}$ time-step is equal to $x'_{\eta-1}$. Then, as shown in Fig. 4.8(b), as the 4th branch turns ON, charge $\Delta Q_\eta = 2^3 C_1 x'_{\eta-1}$ is almost instantly shared with the output capacitance, $C$, modifying the output voltage to $y'_{\eta-1}$, given by

$$y'_{\eta-1} = \beta_\eta x'_{\eta-1} + (1 - \beta_\eta) y_{\eta-1} \quad (4.10)$$

where $\beta_\eta = C_{1\eta}/(C_{1\eta} + C)$ and $C_{1\eta}$ denotes the sum of parasitic capacitances (at node A in Fig. 4.5(b)) on all the branches that turned ON at the $(\eta - 1)T_{CLK}$ edge. For the example shown in Fig. 4.8, $C_{1\eta} = 2^3 C_1$. Now, it is this voltage, $y'_{\eta-1}$ that gets discharged during the $T_{CLK}$ time-step, modifying (4.3) to give

$$y_\eta = \tilde{\alpha}_\eta x'_\eta + (1 - \tilde{\alpha}_\eta)[\beta_\eta x'_{\eta-1} + (1 - \beta_\eta) y_{\eta-1}] \quad (4.11)$$

where $\tilde{\alpha}_\eta = T_{CLK}/(T_{CLK} + R_\eta C)$. From (4.11), it is evident that in the presence of $C_1$, the output at each time-step is not only a function of the current input but also the input at the previous time-step through the voltage stored on the parasitic capacitances.

Equation (4.11), however, does not present the complete picture; the current drawn by the OFF branches during the new time-step, $\eta T_{CLK}$, affects the intermediate voltage $x'$ and hence the output as well. To understand how it does so, we consider the two scenarios for the OFF branches:

i) The branches that *remain* OFF from $(\eta - 1)T_{CLK}$ to $\eta T_{CLK}$ time-step, draw current proportional to the difference between $x'_{\eta-1}$ and $x'_\eta$.

ii) The branches that *turn* OFF from $(\eta - 1)T_{CLK}$ to $\eta T_{CLK}$ time-step, draw current proportional to the difference between $y_{\eta-1}$ and $x'_\eta$.

Since $RC_1 \ll T_{CLK}$, this current draw by the OFF paths can be modelled as a switched-capacitor resistance of value, $T_{CLK}/C_{1x}$, where $C_{1x}$ represents the parasitic capacitance in the OFF branches. Thus, the equivalent circuit in each time-step can be represented by the model that was shown in Fig. 4.9(a), where $R_{eq1,\eta}$ and $R_{eq2,\eta}$ represent the above scenario (i) and (ii) respectively. Applying KCL to the circuit in Fig. 4.9(a), we have,

$$\frac{x_\eta - x'_\eta}{R_S} = \frac{x'_\eta - y_\eta}{R_\eta} + \frac{x'_\eta - x'_{\eta-1}}{R_{eq1,\eta}} + \frac{x'_\eta - y_{\eta-1}}{R_{eq2,\eta}} \quad (4.12)$$

Solving for $x'_\eta$ in (4.12), substituting it in (4.11) and ignoring the second-order terms, it can be shown that the output at each time-step, $y_\eta$ is now given by

$$y_\eta \cong \alpha'_\eta \gamma_\eta \cdot x_\eta + \alpha'_\eta \gamma_{2,\eta} g_{\eta-1} \cdot x_{\eta-1} +$$

$$\left(1 - \alpha'_\eta\right) \cdot \left(\beta_\eta g_{\eta-1} \cdot x_{\eta-1} + (1 - \beta_\eta) \cdot y_{\eta-1}\right) \qquad (4.13)$$

*where*

$\alpha'_\eta = T_{CLK}/(T_{CLK} + (R_\eta + R_S||R_{eq,\eta})C)$,

$R_{eq,\eta} = R_{eq1,\eta}||R_{eq2,\eta}$,

$\gamma_\eta = R_{eq,\eta}/(R_{eq,\eta} + R_S)$,

$g_\eta = \gamma_\eta \cdot R_\eta/(R_\eta + R_S||R_{eq,\eta})$ *and*,

$\gamma_{2,\eta} = (R_S||R_{eq,\eta})/R_{eq1,\eta}$.

# Chapter 5

## Signal Processing/Circuit Solution for Dominant RDAC Parasitics Affecting LPTV RC Filter Performance

As described in Chapter 4 of this thesis, the $C_1$ capacitance of the RDAC is the most dominant parasitic affecting filter performance. The high sheet resistance per unit area offered by the *poly* resistors makes them the resistor of choice for this circuit. While good layout practices can help mitigate some of the wire capacitance, the inherent capacitances associated with the *poly* resistors and switches cannot be avoided. Hence, in this chapter two techniques to reduce/control the effect of $C_1$ capacitance on the filter are presented: the first one is an off-chip, resistor predistortion technique, while the second one is a circuit solution. Both the techniques and their limitations are described in the sections below.

### 5.1 Resistance Predistortion for $C_1$

As described in the previous chapter, the presence of $C_1$ modifies the filter taps from their optimal value and is approximately determined by the expression in (4.13). This tells us, that if $C_1$ were known, based on the resistor variation (and hence the RDAC control) we would know exactly how much error is being made, .i.e. the desired resistor variation is accompanied by an undesired parasitic capacitance variation. The relationship between the error term and the resistor variation, however, is non-trivial and highly non-linear as was shown through the example in Fig. 4.10. As described earlier, the error made in each filter tap depends on both the current and subsequent value of $R$, making global correction a practically impossible task. One would have to resort to a

Viterbi style algorithm to check which of the various combinations of resistor control codes and code transitions would give the closest response to the ideal impulse response in the presence of $C_1$. Since correcting for the stop-band attenuation would require a global, envelope correction, it cannot be optimally achieved.

So, we focus our attention on reducing the harmonic content of the filter response: we resort to a look-up-table based algorithm to pick the best resistor variation that minimizes the magnitude of the error in each filter tap, $|e_\eta|$, from the ideal filter taps. The local corrections performed by the algorithm ensure that the sinusoidal variation is traced as reliably as possible thereby improving the worst-case image rejection.

The calibration algorithm is described in the following flow-chat:

---

**Algorithm 1**

---

- Vary the first resistor code from its nominal value, setting an upper limit ($ul1$) and lower limit ($ll1$) for the range of variation. Due to the recursive nature of the error, this first code acts as the starting point for the subsequent code variations.
- For each value of the first resistor code, vary the other $K-1$ resistor codes from their nominal value ($Gcode$) in steps of 1, setting an upper limit ($ul$) and lower limit ($ll$) on the range of this variation:

---

$j = 1$;

**for** $k = [min(2^N - 1, Gcode(1) + ul1) : -1 : max(0, Gcode(1) - ll1)]$ **do**

---

$Gcode\_new(j,1) = k$

$\eta = 2$

**while** $\boldsymbol{\eta} < K + 1$ **do**

**for** $\boldsymbol{c} = [min(2^N - 1, Gcode(\eta) + ul) : -1 : max(0, Gcode(\eta) - ll)]$ **do**

- Calculate new tap value using (4.13) based on the $C_1$ estimate and the transition from $Gcode\_new(j, \eta - 1)$ to $\boldsymbol{c}$, for each new value of $\boldsymbol{c}$.
- Calculate the error for each $\boldsymbol{c}$ using the new tap values calculated above and the original ideal filter tap value corresponding to $Gcode(\eta)$.

**end for**

- Pick the $\boldsymbol{c}$ value, $\boldsymbol{c}^*$ which minimizes the error in the $\eta^{th}$ tap such that $\left(\left(|e_\eta^*| < |e_\eta|\right)\right)$
- Set $Gcode\_new(j, \eta) = \boldsymbol{c}^*$
- $\eta = \eta + 1$

**end while**

- Compute error in the 1st code (which depends on the last code, $K$) and $\sum_{i=1}^{\eta} |e_i^*|$
- $j = j + 1$

**end for**

- Pick set of codes, $Gcode\_new(j^*, :)$ with the minimum $\sum_{i=1}^{\eta} |e_i^*|$

The output of the above calibration algorithm is a set of new resistor control codes (and hence resistor variation), which ensures that each new filter tap has minimal error in the presence of parasitics. Fig. 5.1(a) shows an example filter response with and without the resistance predistortion. The worst filter image level when the algorithm is applied to different center frequencies is shown in Fig. 5.1(b). It should be noted that the correction is limited by the resolution of the available 10-bit RDAC, which affects some center frequencies more than others.

For instance, for errors made around the zero-crossings (which corresponds to larger values of R and hence smaller RDAC codes), the resistor predistortion is limited to a minimum resistor control code of 0. The high slope around the zero-crossings translates to a larger change in the RDAC control from one time-step to the next and hence larger error around the zero-crossings, all of which cannot be fully corrected.

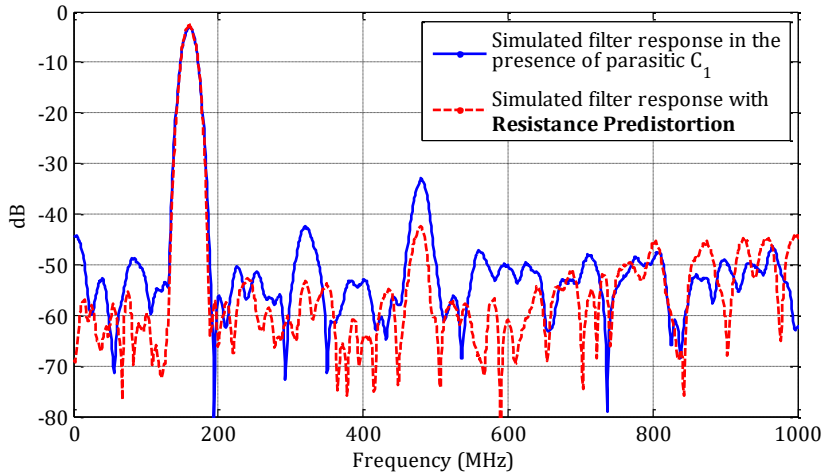


(a)

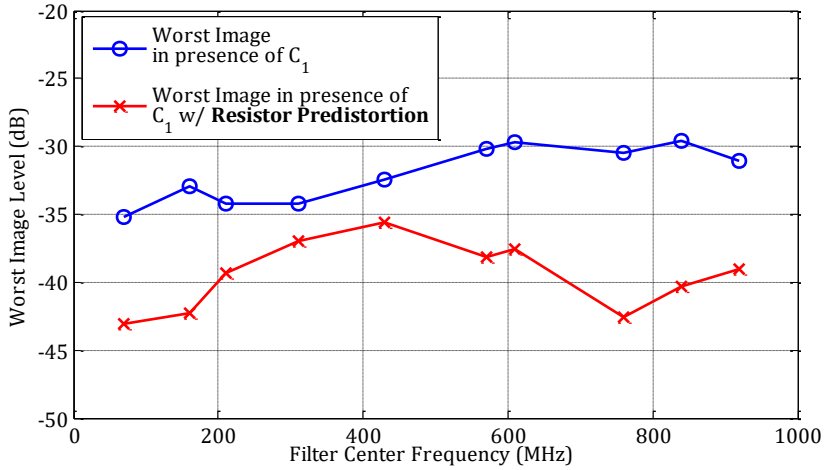


(b)

Fig. 5.1: (a) Example filter response at 160MHz with and without resistance predistortion to account for the presence of $C_1$; (b) Worst filter image level across different center frequencies with and without resistance predistortion.

### *5.1.1 Sensitivity to $C_1$ estimate*

The algorithm relies on the knowledge of $C_1$ to make the correction possible. Estimating the parasitic capacitance from the IC is not straightforward. However, as we show in Fig. 5.2, the correction is not very sensitive to the precise value of $C_1$ and hence capacitance estimates from the parasitic extraction tools in cadence should suffice. This was verified through measurements on the IC used in [28] and is shown in Fig. 5.3 for three example filters at 100MHz, 200MHz and 700MHz. Fig. 5.3 also indicates that $C_1$ is the dominant parasitic capacitance affecting harmonic performance. It must be noted that the PCB board used for this testing contributed to a high upfront $C_P$ capacitance which was also a limiting factor in the measured harmonic rejection with resistance predistortion.

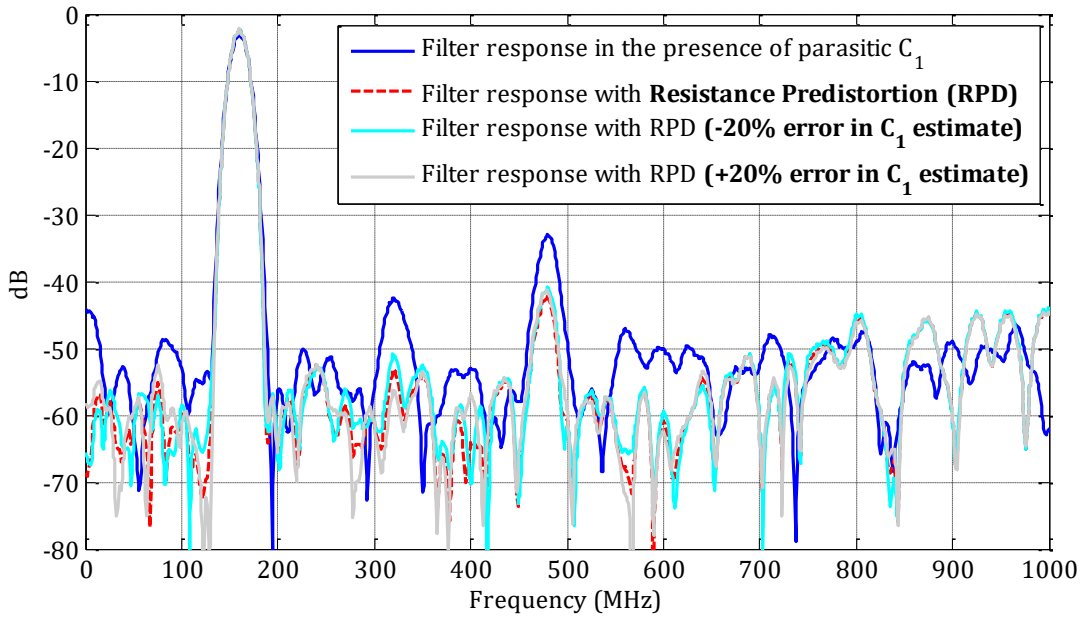


Fig. 5.2: Effect of $C_1$ variation (±20%) on correction algorithm.

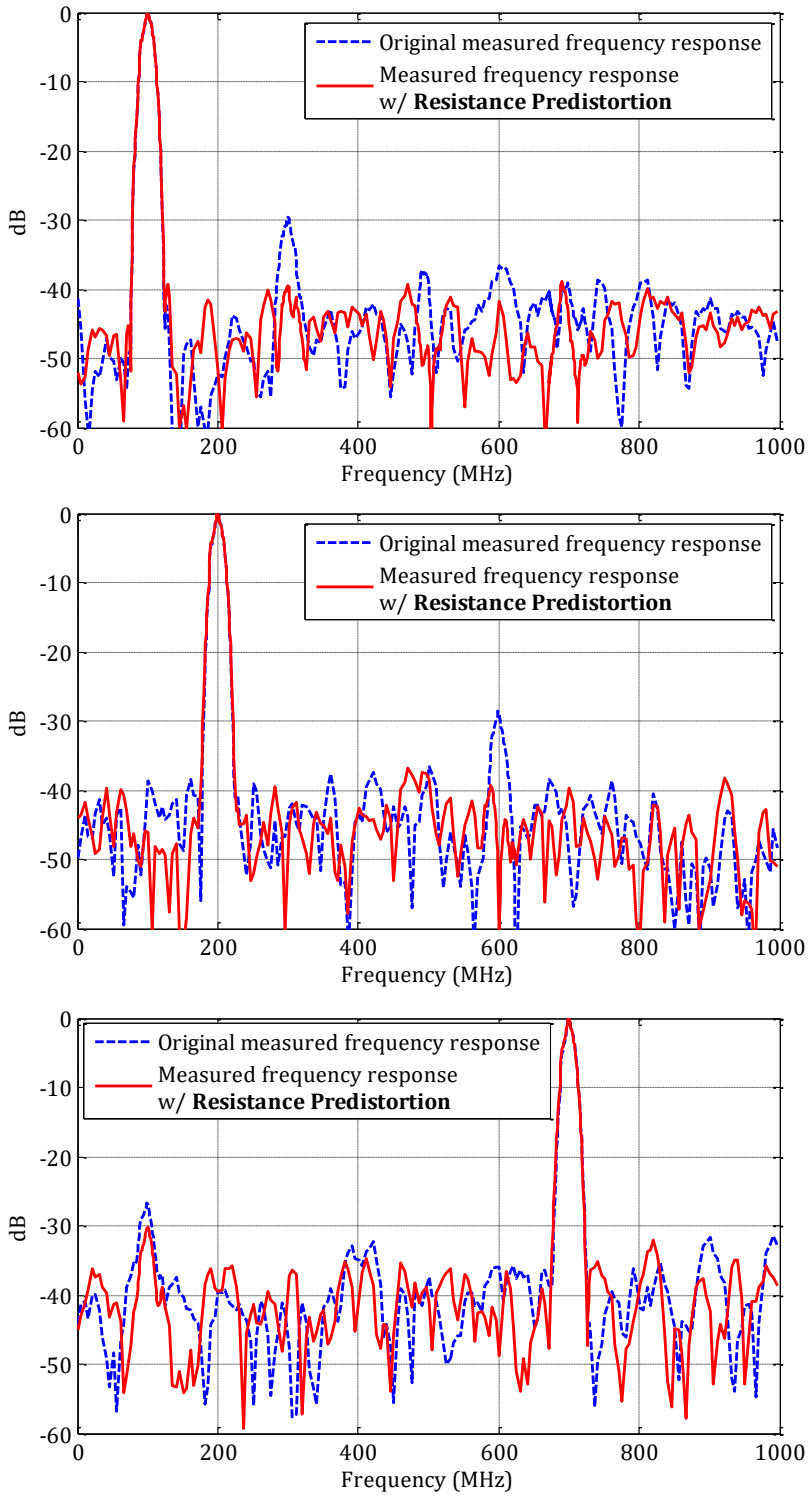


Fig. 5.3: Measured filter responses at 100, 200 and 700MHz from IC used in [28] with resistance predistortion.

## 5.2 Return-to-Infinity RDAC

As seen in Chapter 4 and the previous section, one of the main reasons the parasitic capacitance $C_1$ worsens the filter performance and is hard to account for is because of the recursive, non-linear dependence of the error term on the resistance values. $\beta_\eta g_{\eta-1} x_{\eta-1}$ is the dominant error term in (4.13) and as mentioned earlier, depends on both the current and subsequent values of $R$.

In order to remove this recursive dependence, we propose to use a return-to-infinity (RTI) RDAC as described in Fig. 5.4. Starting with the same RDAC configuration for $R_{\eta-1}$ as in Fig. 4.8, but instead of going to the next resistor value, if we go to infinity, i.e. open all the switches of the RDAC for half the period and then go to the desired R value, we can ensure that the parasitic $C_1$ capacitances that charge share are proportional only to the current value of the resistor, $R_\eta$, as shown in Fig. 5.4. It should be noted that here we are not preventing the charge sharing, but merely making sure that it behaves in a controlled manner.

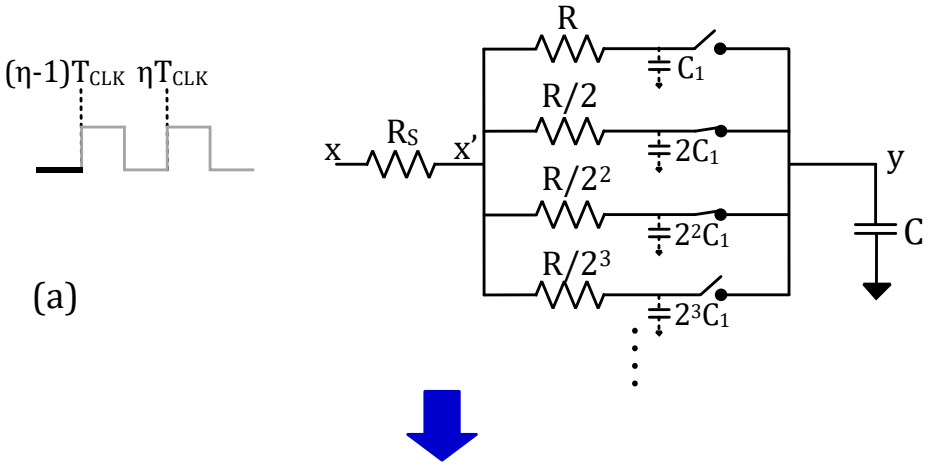

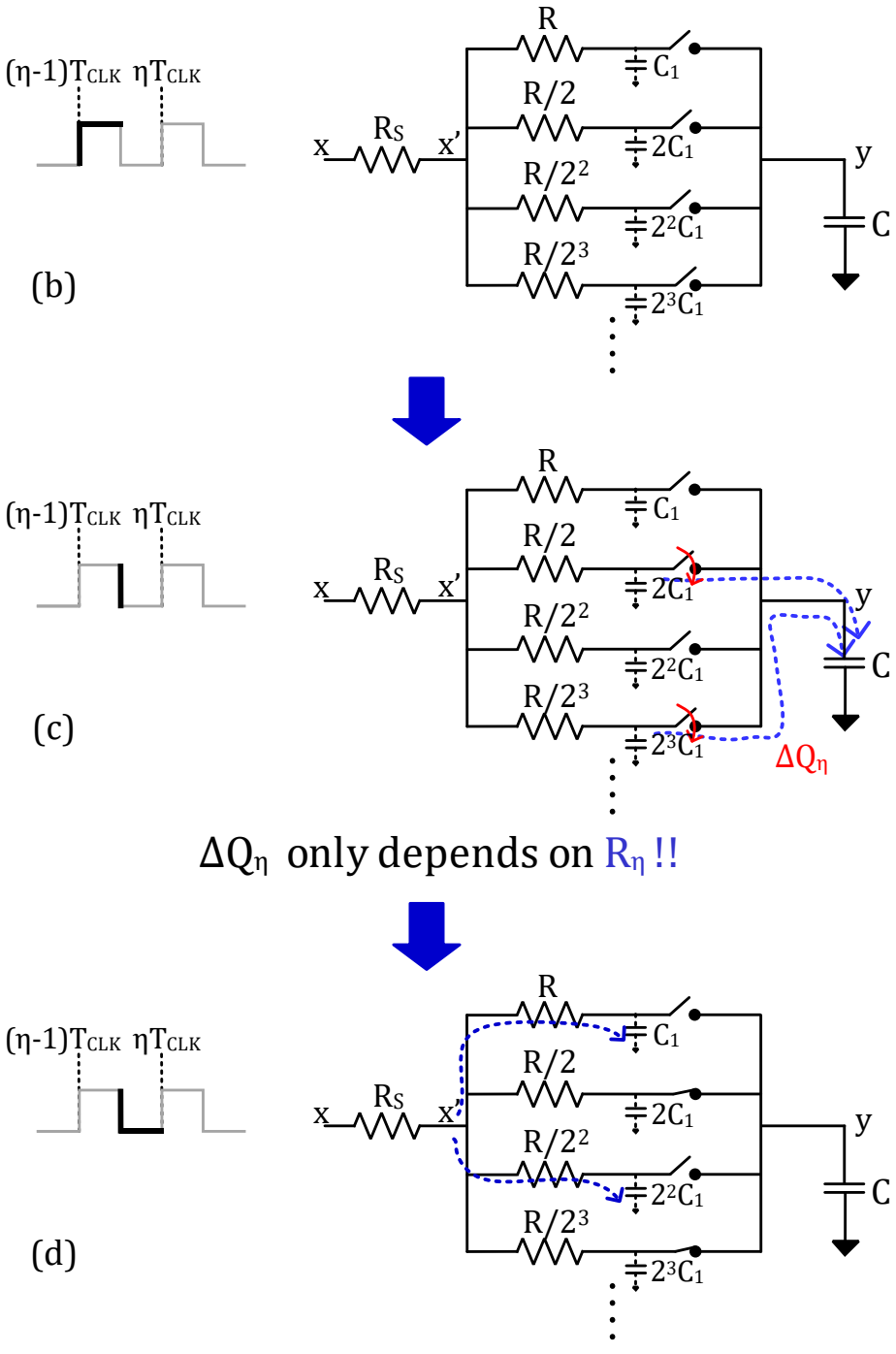


Fig. 5.4: Example circuit operations in the presence of $C_1$ in the RTI-RDAC configuration.

To understand how this helps, we can think of the RTI-RDAC as implementing the original LPTV RC filter with zeros inserted in the impulse response at the time-steps when the resistance goes to infinity, i.e. the filter is just an up-sampled version of the original filter [29]. Fig. 5.5(a) shows the impulse response of an ideal low-pass filter with the RTI-RDAC, where the zeros inserted can be clearly seen. Now, the presence of the parasitic capacitance $C_1$ and the charge sharing that results from it, will lead to non-zero intermediate terms. However, as shown in the equivalent filter model shown in Fig. 5.5(b) for an example low-pass filter, since the error made in each tap is almost proportional to the resistor value for that tap, we essentially have two time-interleaved filters with the same impulse response "shape" and hence, the stop-band attenuation is unaffected! This is shown for a low-pass filter in Fig. 5.6 where the stop-band attenuation of the LPTV RC filter with and without the parasitic $C_1$ capacitance is the same when the RTI-RDAC is used. The transition BW, however, is slightly worsened: this is because, the presence of extra charge loss paths through the parasitic capacitances makes the overall impulse response die down a little faster translating to a slightly higher transition BW. The figure also shows the filter response with the regular RDAC in the presence of $C_1$, which helps reiterate the benefit of using the RTI-DAC in order to preserve the stop-band attenuation.

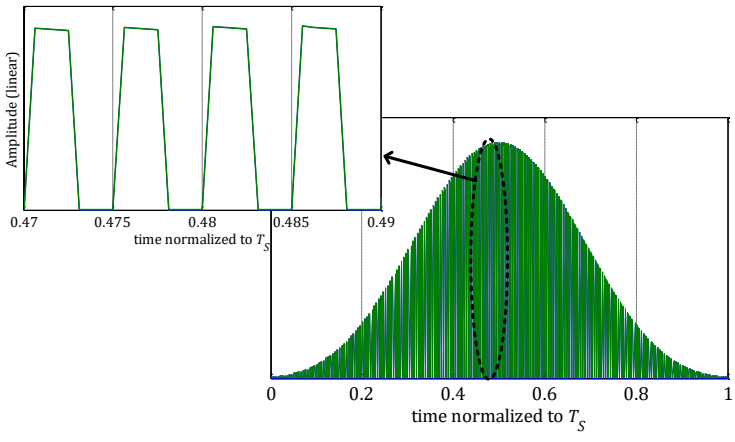


(a)

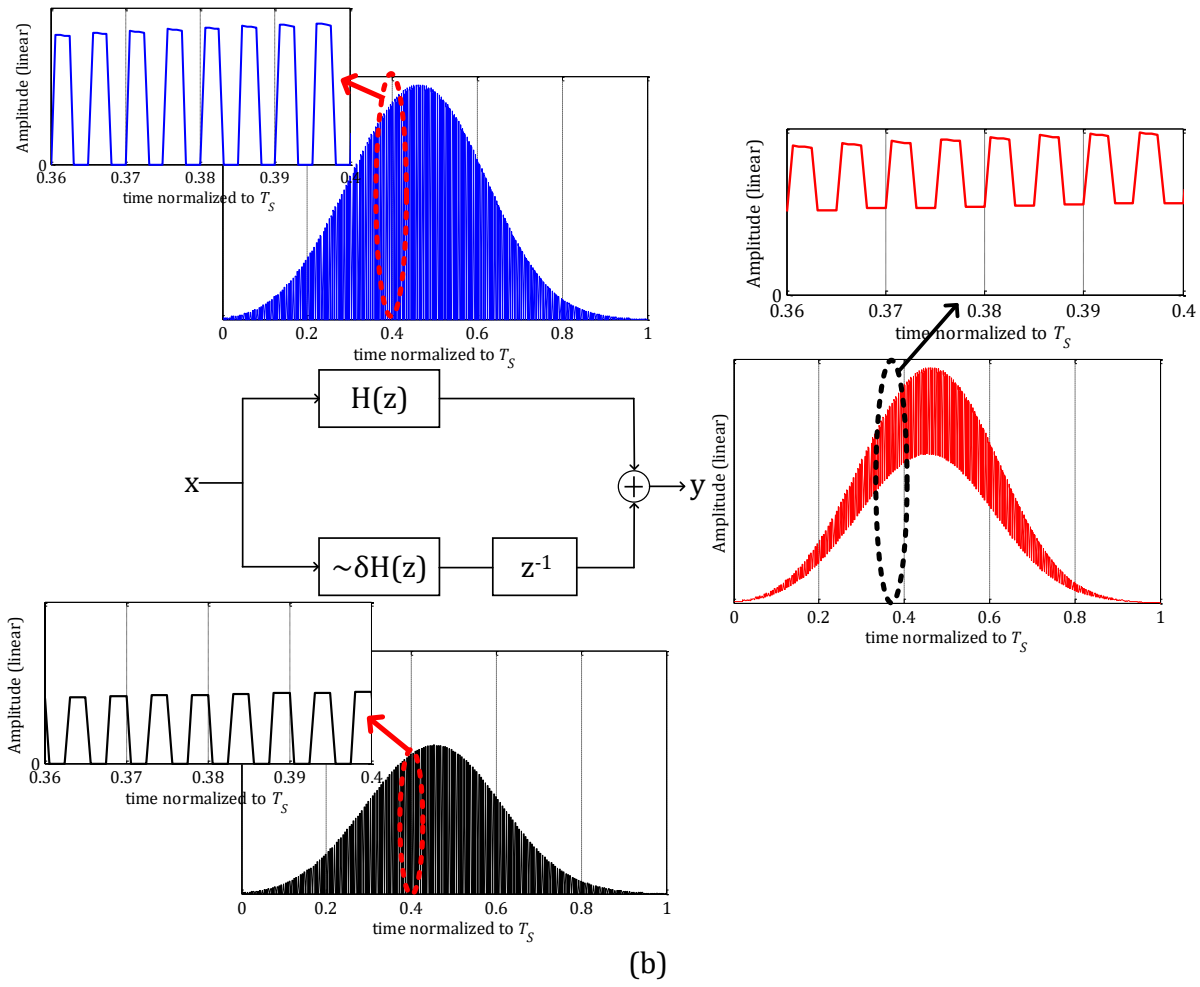


Fig. 5.5: (a) Impulse response for an ideal low-pass filter with return-to-infinity RDAC; (b) Equivalent model of the LPTV RC filter with return-to-infinity RDAC in the presence of $C_1$ and the effective impulse response.

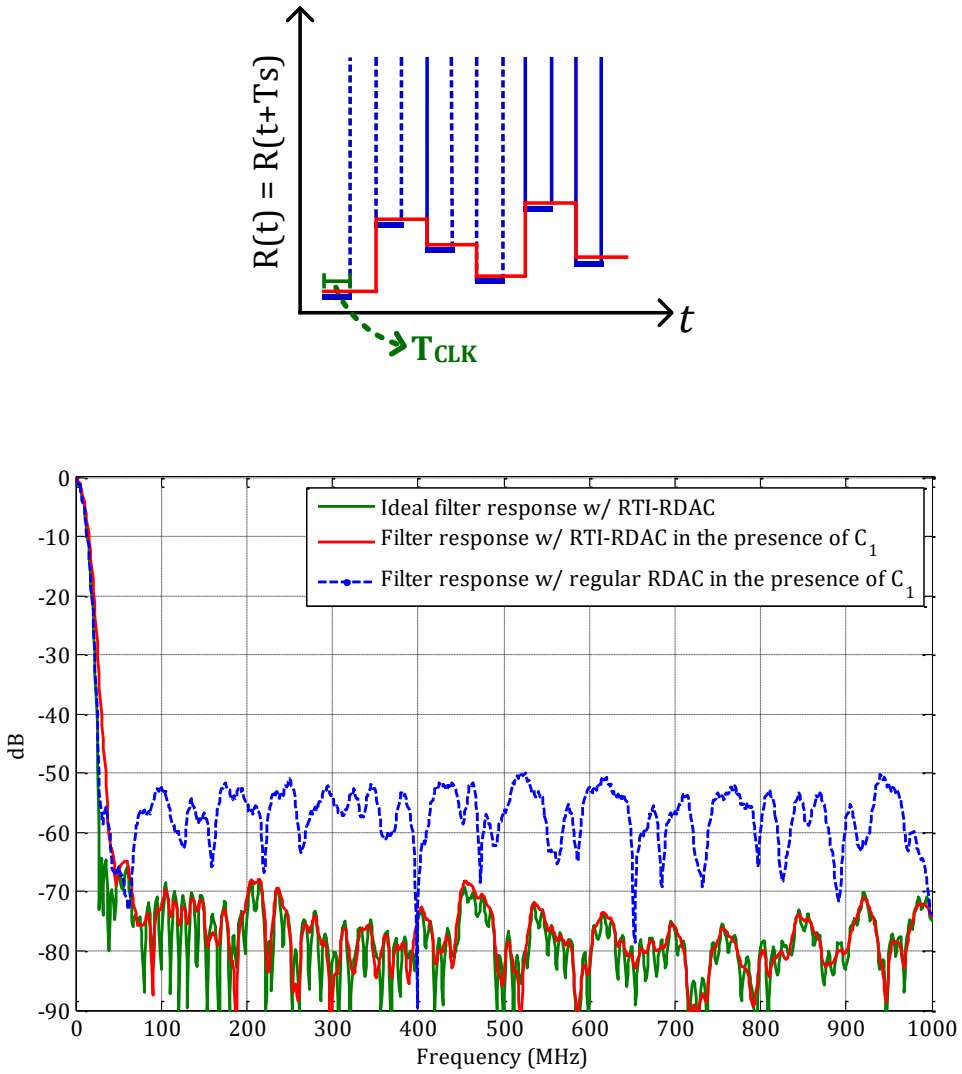


Fig. 5.6: (Top) An example resistor variation for a return-to-infinity (RTI)-RDAC; (Bottom) Frequency response for an example low-pass filter using the RTI-RDAC.

While the stop-band attenuation is preserved as long as the shape/envelope of the impulse response is maintained, the harmonic rejection is much more sensitive. Firstly, the presence of the source resistance, $R_S$ affects the proportionality between the total resistance value at each time-step and the amount of charge shared by the parasitic capacitance $C_1$ in the RDAC. Secondly, as shown in Fig. 5.4(d), the current drawn by the OFF branches doesn't have a linear relationship with the filter taps: It is proportional to $(2^N - 1 - n)C_1$ where $N$ is the total number of bits and $n$

is the resistor control code. So while the harmonic rejection is reduced, it is not completely eliminated. A mathematical model for the LPTV filter using the RTI-RDAC in the presence of $C_1$ can be derived in the same manner as shown in Appendix 4.3.1. Fig. 5.7 shows an example band-pass filter employing the RTI-RDAC and compares it with the original filter response in the presence of the parasitic $C_1$ capacitance. As can be seen, the harmonic image is ~ 7dB lower while the stop-band attenuation is same as for the ideal filter.

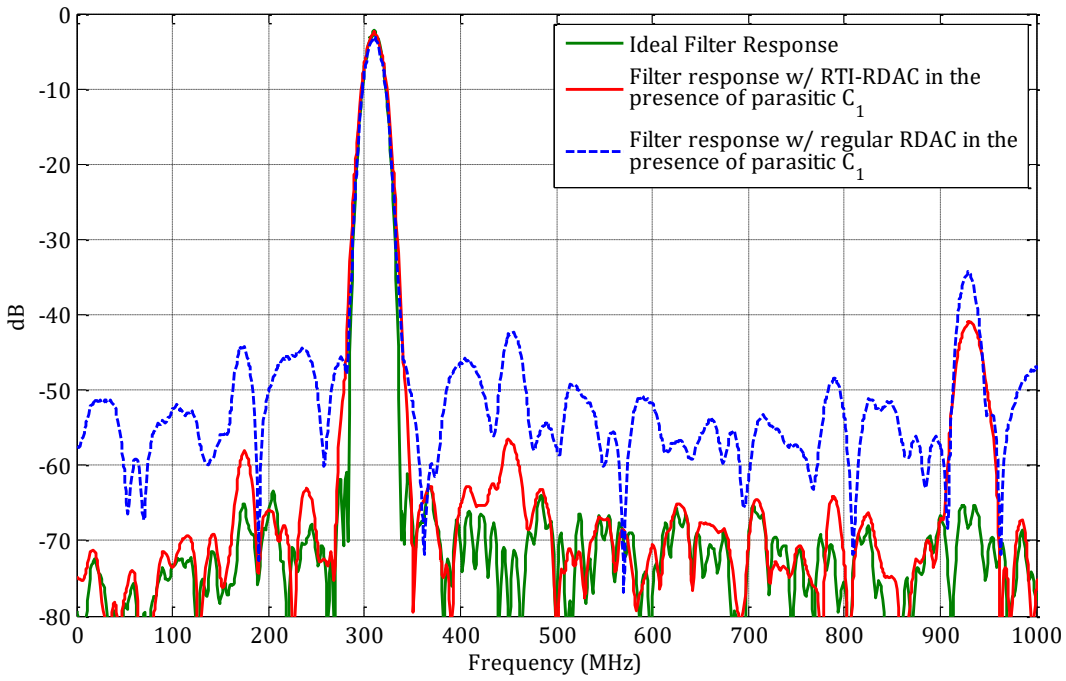


Fig. 5.7: Frequency response for an example band-pass filter at 310MHz using the return-to-infinity RDAC.

### *5.2.1 Polyphase Implementation*

As shown in Fig. 5.5, the RTI-RDAC leads to an up-sampled version of the original filter. Hence, to ensure that the scanning range remains the same, the input sampling rate needs to double. Based on the exact implementation of the digital hardware, this can lead to an increase in power consumption. Also, for the same DC gain, bandwidth and RDAC (minimum R) used, the capacitance is reduced by a factor of 2 which translates to a 3dB increase in output noise power. A potential solution to alleviate these effects while still benefitting from the RTI-RDAC is to use a polyphase implementation like the one shown in Fig. 5.8. The resistor values in the two branches can be time-interleaved to ensure the scanning range is maintained and the filter capacitance is unchanged from the one used for the regular RDAC structure. As shown in Fig. 5.9, the stop-band attenuation is retained, the harmonic rejection is slightly worsened. This is expected because the presence of two RDACs increases the number of OFF paths drawing parasitic current.

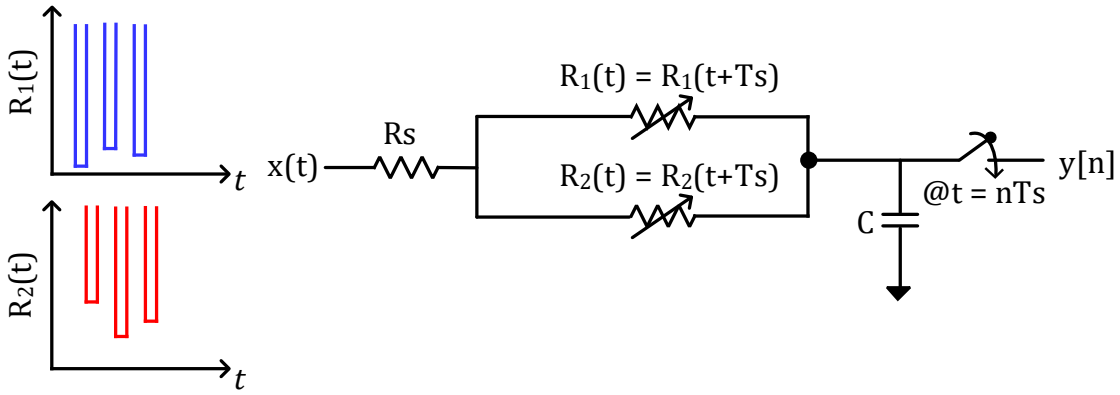


Fig. 5.8: Polyphase implementation using the RTI-RDAC.

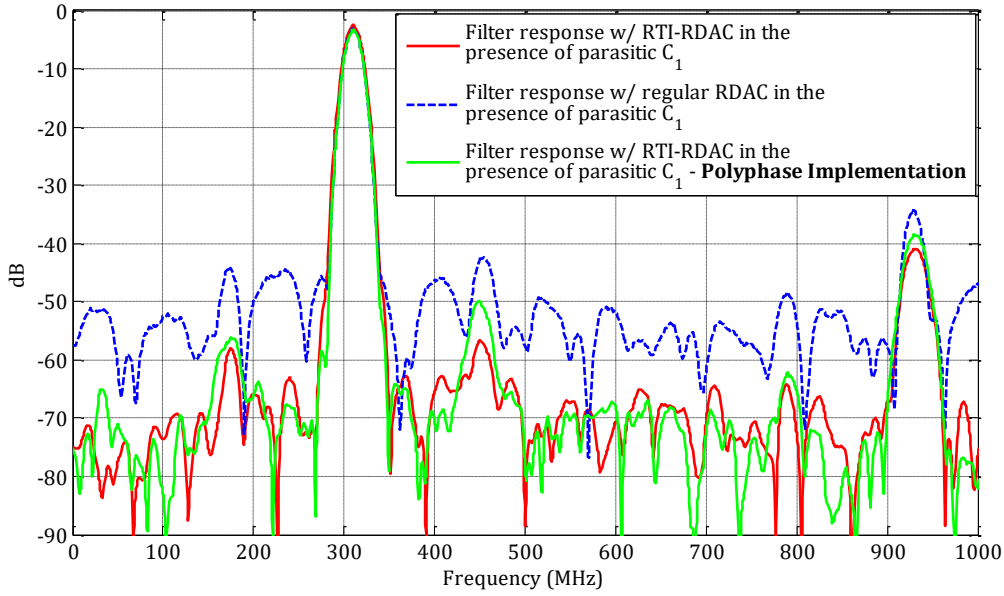


Fig. 5.9: Frequency response for an example band-pass filter at 310MHz using the polyphase implementation of the RTI-RDAC.

### *5.2.2 Parallel Spectrum Scan*

As mentioned in Chapter 1, the spectrum scan time is an important metric for spectrum scanners as well. A lower scan time can help improve the system throughput or can be traded-off to improve the detected SNR. Since the LPTV filter based spectrum scanner essentially does a serial scan of the spectrum, it does not improve on the prior-art as far as scan time is concerned.

One way to improve the scan time would be to have many FA scanners in parallel with each other. However, the passive nature of these scanners would make them interact with each other and co-designing these scanners in the presence of memory elements (capacitances) would be a very challenging task. So, in order to overcome this challenge, we again resort to the RTI-RDAC.

As can example, consider performing two parallel scans using the structure shown in Fig. 5.10. If a regular RDAC is used, each of the scanners would load the other, severely distorting the filtering performance. On the other hand, if an RTI-RDAC is used, where the resistance goes to infinity in a time-interleaved manner, one branch appears like an open to the other, and does not load it. This way two independent parallel scans on the same input spectrum can be performed.

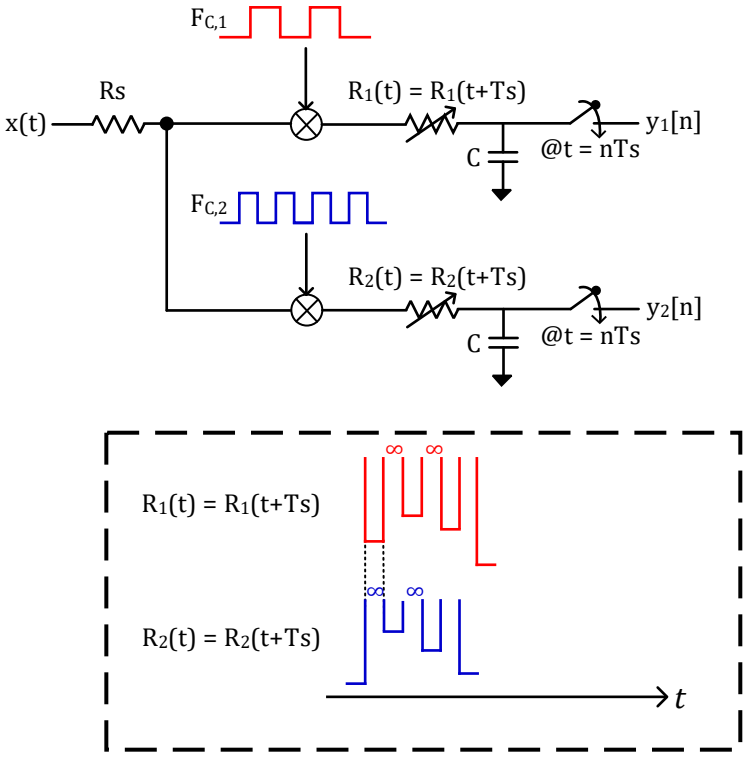


Fig. 5.10: Example filter structure to perform a parallel spectrum scan at two different LO locations using the RTI-RDAC.

# Conclusions

In this dissertation, a new approach to spectrum scanning is presented that uses a passive, LPTV filter based circuit. The operation and design of the LPTV *RC* filters is described in detail together with the circuit innovations used to implement them in IC. The measurement results show that the use of LPTV circuits is a promising idea. The implemented IC has wide bandwidth operation and programmability, highest linearity and lowest power compared to state-of-the-art designs along with acceptable sensitivity and scan time.

In addition to the circuit design details and the measurement results presented, a theoretical analysis of the some of the important limiting factors affecting the filter performance are presented. It is shown that the periodically time-varying resistor which sits at the heart of this LPTV circuit is plagued by various parasitics that can degrade filter performance. The analysis helps provide insights for developing correction algorithms and circuit techniques. A resistance predistortion scheme is presented to tackle the effect of the dominant RDAC parasitic capacitance on harmonic rejection. The limited resolution of the RDAC together with the recursive manner in which the error terms manifest themselves limits the improvements provided by the predistortion scheme. In light of these limitations, a circuit technique is also described that uses a return-to-infinity (RTI)-RDAC. It is shown to completely eliminate the problem of stopband attenuation while slightly improving the harmonic rejection as well.

The current stop-band attenuation and harmonic rejection achieved by the scanner may not be good enough for some applications. Hence, future work on this scanner is aimed at further improving the filter performance. An IC prototype using the RTI-RDAC for improved stop-band

attenuation can be developed together with further investigation targeting better harmonic rejection. The use of RTI-RDACs to perform parallel spectrum scans for improved scanning times or to increase the frequency scanning range can also be explored.

# References


[1] K. A. Jenkins et al., “Integrated CMOS spectrum analyzer for on-chip diagnostics using digital autocorrelation of coarsely quantized signals,” US Patent 7 218 091, May 15, 2007.

[2] Nekovee, M., "Cognitive Radio Access to TV White Spaces: Spectrum Opportunities, Commercial Applications and Remaining Technology Challenges," *New Frontiers in Dynamic Spectrum, 2010 IEEE Symposium on* , vol., no., pp.1,10, 6-9 April 2010.

[3] A. El-Mougy, et al., "Reconfigurable Wireless Networks," in *Proceedings of the IEEE*, July 2015.

[4] R. Tandra et al., “Fundamental limits on detection in low SNR under noise uncertainty,” in Proc. Int. Wireless Netw., Comm. and Mobile Comp. Conf., vol. 1, Maui, HI, USA, 13–16 Jun. 2005, pp. 464–469.

[5] D. Cabric, A. Tkachenko, and R. W. Brodersen, “Spectrum sensing measurements of pilot, energy, and collaborative detection,” in *Proc. IEEE Military Communications Conf. (MILCOM)*, 2006, pp. 1–7.

[6] M. S. Oude Alink, A. B. J. Kokkeler, E. A. M. Klumperink, G. J. M. Smit, and B. Nauta, “Lowering the SNR wall for energy detection using cross-correlation,” IEEE Trans. Veh. Technol.,vol. 60, no. 8, pp. 3748–3757, Oct. 2011.

[7] G. Hattab and M. Ibnkahla, "Multiband Spectrum Access: Great Promises for Future Cognitive Radio Networks," in *Proceedings of the IEEE*, vol. 102, no. 3, pp. 282-306, March 2014.

[8] A. Goel, et al, “A 130-nm CMOS 100- Hz–6-GHz reconfigurable vector signal analyzer and software-defined receiver,” *IEEE Trans. Microw. Theory Techn*., vol. 60, no. 5, pp. 1375–1389, 2012.

[9] Oude Alink, M.S.; Klumperink, E.A.M.; Kokkeler, A.B.J.; Zhiyu Ru; Wei Cheng; Nauta, B., "Using Crosscorrelation to Mitigate Analog/RF Impairments for Integrated Spectrum Analyzers," in *Microwave Theory and Techniques, IEEE Transactions on* , vol.61, no.3, pp.1327-1337, March 2013.

[10] M. S. Oude Alink, E. A. M. Klumperink, M. C. M. Soer, A. B. J. Kokkeler, and B. Nauta, “A 50MHz-to-1.5GHz cross-correlation CMOS spectrum analyzer for cognitive radio with 89dB SFDR in 1MHz RBW,” in Proc. 4th IEEE Symp. on New Frontiers in Dynamic Spectrum Access Networks (DySPAN), Singapore, 6–9 Apr. 2010.

[11] M. S. Oude Alink *et al*., "A CMOS spectrum analyzer frontend for cognitive radio achieving +25dBm IIP3 and −169 dBm/Hz DANL," *2012 IEEE Radio Frequency Integrated Circuits Symposium*, Montreal, QC, 2012, pp. 35-38.

[12] M. Ingels et al., “A 5 mm 40 nm LP CMOS 0.1-to-3 GHz multistandard transceiver,” *IEEE Int. Solid-State Circuits Conf. Dig. Tech. Papers*, 2010, pp. 458–459.

[13] S. Pollin et al., “Digital and analog solution for low-power multi-band sensing,” in IEEE Symp. New Frontiers in Dynamic Spectrum, 2010, pp. 1–2.

[14] B. Murmann, ADC Performance Survey 1997–2015. [Online]. Available: http://web.stanford.edu/~murmann/adcsurvey.html].

[15] R. T. Yazicigil, T. Haque, M. R. Whalen, J. Yuan, J. Wright and P. R. Kinget, "A 2.7-to-3.7GHz rapid interferer detector exploiting compressed sampling with a quadrature analog-to-information converter," 2015 IEEE International Solid-State Circuits Conference - (ISSCC) Digest of Technical Papers, San Francisco, CA, 2015, pp. 1-3.

[16] R. T. Yazicigil, T. Haque, M. Kumar, J. Yuan, J. Wright and P. R. Kinget, "A compressed-sampling time-segmented quadrature analog-to-information converter for wideband rapid detection of up to 6 interferers with adaptive thresholding," *2016 IEEE Radio Frequency Integrated Circuits Symposium (RFIC)*, San Francisco, CA, 2016, pp. 282-285.

[17] M. Mishali, Y. C. Eldar, O. Dounaevsky and E. Shoshan, "Xampling: Analog to Digital at Sub-Nyquist Rates," in IET Circuits, Devices & Systems, vol. 5, no. 1, pp. 8-20, January 2011.

[18] M. Rachid, et al., “Filtering by Aliasing,” IEEE Trans. Signal Processing, vol.61, no.9, pp.2319-2327, 2013.

[19] N. Sinha, et al., “A Sharp Programmable Passive Filter based on Filtering by Aliasing,” VLSI Circuits, 2015. Digest of Technical Papers. 2015 Symposium on, vol., no., pp., 16-19 June 2015.

[20] S. Pavan and R. S. Rajan, “Inter-reciprocity in linear periodically timevarying networks with sampled outputs,” IEEE Trans. Circuits Syst. II, Exp. Briefs, vol. 61, no. 9, pp. 686–690, September 2014.

[21] S. Hameed, M. Rachid, B. Daneshrad and S. Pamarti, "Frequency-domain analysis of a mixer-first receiver using conversion matrices," *2015 IEEE International Symposium on Circuits and Systems (ISCAS)*, Lisbon, 2015, pp. 541-544.

[22] M. Grant and S. Boyd, CVX: Matlab software for disciplined convex programming, version 1.21, Available: cvxr.com/cvx , April 2011.

[23] S. Wu, S. Boyd, and L. Vandenberghe, “FIR filter design via spectral factorization and convex optimization,” Available: http://www.ee.ucla.edu/~vandenbe/publications/magdes.pdf.

[24] N. Sinha; M. Rachid; S. Pavan; S. Pamarti, "Design and Analysis of an 8 mW, 1 GHz Span, Passive Spectrum Scanner With >+31 dBm Out-of-Band IIP3 Using Periodically Time-Varying Circuit Components," in IEEE Journal of Solid-State Circuits , vol.PP, no.99, pp.1-17.

[25] M. Tohidian, I. Madadi and R. B. Staszewski, "Analysis and Design of a High-Order Discrete-Time Passive IIR Low-Pass Filter," in IEEE Journal of Solid-State Circuits, vol. 49, no. 11, pp. 2575-2587, November 2014.

[26] Oude Alink, Mark Stefan, “RF spectrum sensing in CMOS exploiting crosscorrelation.” PhD Thesis, University of Twente, 2013.

[27] M. Rachid, “Filtering by Aliasing and its application to Reconfigurable Filtering and Compressive Signal Acquisition,” Ph.D Thesis, UCLA, 2013.

[28] N. Sinha, M. Rachid and S. Pamarti, "An 8mW, 1GHz span, passive spectrum scanner with > +31dBm out-of-band IIP3," 2016 IEEE Radio Frequency Integrated Circuits Symposium (RFIC), San Francisco, CA, 2016, pp. 278-281.

[29] P. P. Vaidyanathan, "Multirate digital filters, filter banks, polyphase networks, and applications: a tutorial," in *Proceedings of the IEEE,* vol. 78, no. 1, pp. 56-93, Jan 1990.